UNIVERSIDADE FEDERAL DE VIÇOSA

Hydromechanical behavior of filtered iron ore tailings stacks: geotechnical characterization and numerical analyses

Sérgio Leandro Scher Dias Neto
Doctor Scientiae

VIÇOSA - MINAS GERAIS
2025

SÉRGIO LEANDRO SCHER DIAS NETO

Hydromechanical behavior of filtered iron ore tailings stacks: geotechnical characterization and numerical analyses

Thesis submitted to the Civil Engineering Graduate Program of the Universidade Federal de Viçosa in partial fulfillment of the requirements for the degree of *Doctor Scientiae*.

Adviser: Taciano Oliveira da Silva

Co-advisers: Roberto Lopes Ferraz
Eduardo A. G. Marques

VIÇOSA - MINAS GERAIS
2025

Ficha catalográfica elaborada pela Biblioteca Central da Universidade Federal de Viçosa - Campus Viçosa

T
D541r
2025

Dias Neto, Sérgio Leandro Scher, 1993-
Hydromechanical behavior of filtered iron ore tailings stacks: geotechnical characterization and numerical analyses / Sérgio Leandro Scher Dias Neto. – Viçosa, MG, 2025.
1 tese eletrônica (125 f.): il. (algumas color.).

Texto em inglês.
Orientador: Taciano Oliveira da Silva.
Tese (doutorado) - Universidade Federal de Viçosa, Departamento de Engenharia Civil, 2025.
Inclui bibliografia.
DOI: https://doi.org/10.47328/ufvbbt.2025.504
Modo de acesso: World Wide Web.

1. Minérios de ferro - Eliminação de resíduos. 2. Mecânica do solo. I. Silva, Taciano Oliveira da, 1975-. II. Universidade Federal de Viçosa. Departamento de Engenharia Civil. Programa de Pós-Graduação em Engenharia Civil. III. Título.

CDD 22. ed. 622.341

Bibliotecário(a) responsável: Euzébio Luiz Pinto CRB-6/3317

SÉRGIO LEANDRO SCHER DIAS NETO

Hydromechanical behavior of filtered iron ore tailings stacks: geotechnical characterization and numerical analyses

Thesis submitted to the Civil Engineering Graduate Program of the Universidade Federal de Viçosa in partial fulfillment of the requirements for the degree of *Doctor Scientiae*.

APPROVED: February 7, 2025.

Assent:

Sérgio Leandro Scher Dias Neto
Author

Taciano Oliveira da Silva
Adviser

Dedico este trabalho à minha tia Neide, ao meu primo Fabiano,
à tia Lourdinha, ao tio Sérgio e ao meu avô Antônio...

ACKNOWLEDGMENTS

Aos meus pais, Nélia e Geraldo, pela presença constante, pelo apoio incondicional e pelo amor que me sustenta em todas as fases da vida. Vocês são meu alicerce e minha maior inspiração. Ao meu irmão, Rodrigo, que sempre acreditou em mim e me incentivou a alcançar meus sonhos. Vocês são meu porto seguro. Amo vocês profundamente!

Ao Professor Roberto, por sua orientação criteriosa, pelas valiosas sugestões e pelo compromisso com meu crescimento acadêmico e pessoal ao longo desta jornada.

Ao Professor Paulo Sérgio, pela generosidade em compartilhar seu vasto conhecimento e pelo entusiasmo contagiante pela área da Geotecnia, que tanto me inspira.

Ao Professor Taciano, pela orientação precisa, pela paciência e pela confiança depositada no meu trabalho, sempre me encorajando a ir além.

Ao Professor Eduardo e ao Professor Heraldo, pelas contribuições essenciais, pelos conselhos valiosos e pelo apoio nos momentos decisivos desta pesquisa.

Aos meus amigos Gabriela e Fernando, que estiveram ao meu lado em cada passo desta jornada, compartilhando desafios, conquistas e muitas risadas.

Ao pessoal do Laboratório de Engenharia Civil da UFV, especialmente a Marcelo e Leonício, pela disponibilidade, pela colaboração e pelos momentos leves e descontraídos que tornaram o dia a dia mais agradável.

A todos, minha gratidão por fazerem parte desta trajetória tão significativa e transformadora!

This work has been sponsored by the following Brazilian research agencies: Coordination for the Improvement of Higher Education Personnel (CAPES; Financing code 001), Minas Gerais State Foundation for Research Aid (FAPEMIG) and National Council of Scientific and Technological Development (CNPq).

ABSTRACT

NETO, Sérgio Leandro Scher Dias, D.Sc., Universidade Federal de Viçosa, February, 2025. **Hydromechanical behavior of filtered iron ore tailings stacks: geotechnical characterization and numerical analyses**. Adviser: Taciano Oliveira da Silva. Co-advisers: Roberto Lopes Ferraz and Eduardo Antonio Gomes Marques.

The increasing demand for sustainable mining practices has established filtered tailings stacking as a safer and more environmentally responsible solution for managing iron ore tailings (IOT). However, its implementation is challenged by the inherent variability of tailings materials, environmental conditions, and operational factors. This study integrates experimental characterization and numerical modeling to investigate the hydromechanical behavior of silt-sized IOT, focusing on water retention, hydraulic conductivity, void ratio variations, material heterogeneity, and compaction efficiency. Experimental analyses of three representative IOT samples revealed the critical influence of tailings variability and void ratio on hydraulic behavior. Slight variations in particle size distribution significantly affected water retention and hydraulic conductivity. A dual-porosity model captured the effects of fine particle aggregation, while a strong linear relationship was observed between void ratio and water retention curve fitting parameters. Additionally, hydraulic conductivity decreased exponentially with reduced void ratio. Mineralogical characterization was carried out by X-ray diffraction (XRD), while microstructural analyses using scanning electron microscopy (SEM) coupled with energy dispersive spectroscopy (EDS) confirmed the distinctive bimodal pore structure of the materials, underscoring the importance of microstructure in controlling hydraulic behavior. Numerical simulations with fully coupled seepage-deformation models examined the impact of void ratio, tailings variability, and undercompaction on stack stability during construction under alternating weather conditions. Scenarios with lower void ratios effectively preserved matric suction and limited seepage, enhancing geotechnical stability despite material heterogeneity. In contrast, undercompacted scenarios, exacerbated by rainy periods, exhibited rapid saturation, perched water tables, and elevated pore pressures, significantly reducing the Factor of Safety (FoS), particularly during early construction stages. These findings highlight the critical role of precise compaction strategies in mitigating risks associated with tailings variability, environmental interactions, and seasonal rainfall. By integrating experimental and numerical approaches, this study provides a comprehensive framework for designing and evaluating filtered tailings stacks, addressing the complexities of unsaturated soil mechanics

and ensuring safer waste management solutions.

Keywords: iron ore tailings; filtered tailings; hydraulic behavior; unsaturated soil mechanics; numerical modeling; stability analysis

RESUMO

NETO, Sérgio Leandro Scher Dias, D.Sc., Universidade Federal de Viçosa, fevereiro de 2025. **Comportamento hidromecânico de pilhas de rejeitos de minério de ferro filtrados: caracterização geotécnica e análises numéricas**. Orientador: Taciano Oliveira da Silva. Coorientadores: Roberto Lopes Ferraz e Eduardo Antonio Gomes Marques.

A crescente demanda por práticas sustentáveis na mineração consolidou o empilhamento de rejeitos filtrados como uma solução mais segura e ambientalmente responsável para o gerenciamento de rejeitos de minério de ferro (IOT). No entanto, sua implementação enfrenta desafios devido à variabilidade inerente dos materiais, às condições ambientais e aos fatores operacionais. Este estudo combina a caracterização experimental e modelagens numéricas para investigar o comportamento hidromecânico de rejeitos de minério de ferro siltosos, com foco na retenção de água, condutividade hidráulica, variações no índice de vazios, heterogeneidade do material e eficiência da compactação. Análises experimentais de três amostras representativas de IOT destacaram a influência da variabilidade dos rejeitos e do índice de vazios no comportamento hidráulico. Pequenas variações na distribuição granulométrica impactaram significativamente as características de retenção de água e a condutividade hidráulica. Um modelo de dupla porosidade captou os efeitos da agregação de partículas finas, enquanto uma relação linear foi observada entre o índice de vazios e os parâmetros de ajuste das curvas de retenção de água. Adicionalmente, a condutividade hidráulica diminuiu exponencialmente com a redução do índice de vazios. A caracterização mineralógica foi realizada por difração de raios X (XRD), enquanto as análises microestruturais, utilizando microscopia eletrônica de varredura (SEM) acoplada à espectroscopia por dispersão de energia (EDS), confirmaram a estrutura bimodal de poros característica dos materiais, ressaltando a importância da microestrutura no controle do comportamento hidráulico. Simulações numéricas acopladas de fluxo e deformação avaliaram o impacto do índice de vazios, da variabilidade dos rejeitos e da subcompactação na estabilidade de pilhas durante a construção sob condições climáticas alternadas. Cenários com índices de vazios mais baixos preservaram a sucção matricial e limitaram o fluxo de água, melhorando a estabilidade geotécnica, mesmo com a heterogeneidade dos materiais. Em contraste, cenários com compactação insuficiente, agravados por períodos chuvosos, apresentaram saturação rápida, lençóis freáticos suspensos e poropressões elevadas, reduzindo significativamente o Fator de Segurança (FoS), especialmente nas etapas iniciais da construção. Esses resultados destacam o papel fundamental de estratégias de compactação na

mitigação de riscos associados à variabilidade dos rejeitos, às interações ambientais e às chuvas sazonais. Ao integrar abordagens experimentais e numéricas, este estudo fornece uma base abrangente para o projeto e a avaliação de pilhas de rejeitos filtrados, abordando as complexidades da mecânica dos solos não saturados e promovendo soluções mais seguras para o gerenciamento de resíduos.

Palavras-chave: rejeitos de minério de ferro; rejeitos filtrados; comportamento hidráulico; mecânica dos solos não-saturados; modelagem numérica; análise de estabilidade

SUMÁRIO

CHAPTER 1

GENERAL INTRODUCTION

1. INITIAL CONSIDERATIONS

The transition to sustainable mining practices has prompted a shift in tailings management strategies, with filtered tailings stacking emerging as a safer and more environmentally responsible alternative to conventional tailings dams. This method addresses critical challenges such as reducing the storage footprint, minimizing environmental risks, enhancing geotechnical stability, and enabling the recovery of a substantial portion of the water used in ore beneficiation (Fränkle *et al.*, 2024; Furnell *et al.*, 2022; Sepúlveda; Robert; Camacho-Tauta, 2022). Stacked tailings, often referred to as filtered tailings or dry-stacked tailings, are characterized by their unsaturated state, achieved through dewatering processes that lower water content to levels optimal for compaction (Davies, 2011; Oldecop; Rodari, 2021).

Compared to slurried tailings, the unsaturated state of filtered tailings enhances shear strength and reduces susceptibility to both static and dynamic liquefaction (Ke; Chen; Shan, 2019; Servi *et al.*, 2022). This geotechnical advantage, along with the reduction of risks associated with seepage pollution and internal erosion (Cacciuttolo; Pérez, 2022; Oldecop; Rodari; Muñoz, 2017), aligns with Brazil's regulatory framework introduced after the catastrophic failures of Mariana and Brumadinho, which prohibits upstream tailings dams and mandates the decharacterization of existing ones. These advancements further solidify filtered tailings as a viable alternative for safer and more sustainable mining waste management (Consoli *et al.*, 2022; Sako; Pabst, 2023).

Despite its advantages, filtered tailings stacking faces significant challenges due to the inherent variability in tailings material properties and environmental conditions. Factors such as grain size distribution, mineralogical composition, and seasonal weather variations directly influence dewatering efficiency (Carneiro *et al.*, 2023; Rissoli *et al.*, 2024). Additionally, operational constraints during the rainy season in tropical regions like Brazil exacerbate difficulties in maintaining optimal compaction. Excess water content often requires temporary storage in drying areas—causing delays—or placement in non-structural zones with limited or no compaction, further complicating operational efficiency (Crystal; Hore; Ezama, 2018).

As stack heights in Brazil surpass 100 meters, managing filtered tailings becomes increasingly complex due to intensified overburden stresses, which lead to volume reduction and elevated degrees of saturation. These changes compromise the unsaturated state initially achieved during deposition, particularly when drainage systems are insufficient to handle increased seepage pressures (Farenzena *et al.*, 2024; Ulrich, 2019). To address these challenges, effective management of filtered tailings requires precise control of the saturation profile, ensuring that stability is maintained under varying environmental and operational conditions (Cao *et al.*, 2021).

Accurately modeling the behavior of filtered tailings requires a comprehensive understanding of tailings-atmosphere interactions, with the water retention curve (WRC) and unsaturated hydraulic conductivity function serving as essential tools. These functions enable the prediction of seepage dynamics and variations in matric suction within the stack as environmental conditions change (Wilson, 2021). This is particularly critical for tailings with complex structural characteristics, such as multimodal porosity, which significantly influence water retention and flow behavior (Schafer; Beier, 2020; Zhang; Wilson; Fredlund, 2019). By capturing these interactions, it becomes possible to assess seepage dynamics, matric suction distribution, and pore pressure development, all of which are key factors in maintaining slope stability and ensuring the long-term performance of filtered tailings stack. (Fredlund; Rahardjo; Fredlund, 2012; Guedes *et al.*, 2024; Montani; Pornillos; Munoz, 2013).

Given the inherent challenges of filtered tailings stack construction, achieving consistent compaction and maintaining unsaturated conditions throughout the stack remains a significant hurdle. The variability in tailings materials, particularly evident in iron ore tailings, combined with the effects of environmental factors such as alternating wet and dry seasons, introduces complexities in maintaining uniform hydraulic and mechanical properties (Carmignano *et al.*, 2021; Pires *et al.*, 2019). These variations often lead to heterogeneities within the stack, which can promote perched water tables, increase seepage, and elevate pore pressures—conditions that compromise stability and safety. To address these issues, a deeper understanding of the interactions between material properties, environmental conditions, and operational practices is essential. Such insights are critical for developing robust design and management strategies that ensure the safe and sustainable performance of filtered tailings stacks.

2. RESEARCH JUSTIFICATION

In Brazil, although there is no standard specifically addressing the design and implementation of filtered tailings stacks, the ABNT NBR 13029 **(**2024) standard provides guidelines for the design and implementation of waste rock piles. This standard emphasizes safety, operational efficiency, and minimizing environmental impacts. However, it does not explicitly require the use of stress-strain analyses alongside the limit equilibrium method (LEM) for assessing the stability and performance of filtered tailings stacks.

In contrast, the ABNT NBR 13028 (2024) standard, which focuses on the design of mining dams, recognizes scenarios where complementary analyses, such as numerical methods, are necessary. For materials prone to strain-softening or liquefaction, numerical simulations are recommended to capture nonlinear stress-strain behavior and incremental construction sequences. This acknowledgment highlights the increasing importance of advanced modeling techniques in geotechnical assessments, particularly for structures subjected to complex loading conditions and environmental variability.

Internationally, while specific regulations may not explicitly mandate the use of stress-strain or numerical analyses in conjunction with LEM for filtered tailings stacks, the integration of advanced analytical techniques is widely regarded as best practice in geotechnical design (ANCOLD, 2019; CDA, 2019; GISTM, 2020; ICOLD, 2021). These methods enable more realistic modeling of material behavior, accounting for complex interactions within the structure and providing a more reliable foundation for stability assessments.

In this context, the integration of numerical simulations into the assessment framework becomes critical, as these techniques provide the tools necessary to capture complex interactions within the stack, ensure the long-term stability of filtered tailings stacks, and meet the safety and sustainability demands of modern mining operations. While current regulations may not explicitly require stress-strain or numerical analyses, this study demonstrates their necessity in advancing geotechnical design practices for filtered tailings stacks.

3. OBJECTIVES

The main objective of this research is to propose a comprehensive framework for applying unsaturated soil mechanics to the design and assessment of filtered tailings stacks, with a focus on iron ore tailings (IOT) from the Quadrilátero Ferrífero region in Brazil. This framework includes the development of a practical methodology for deriving unsaturated hydraulic

properties through laboratory testing and integrates these properties into advanced numerical simulations using coupled seepage-deformation models. These simulations aim to evaluate transient hydraulic responses and mechanical performance of filtered tailings stacks under various operational and environmental scenarios.

The specific objectives are:

- Characterize the chemical, mineralogical, and physical properties of representative iron ore tailings (IOT) samples from the Quadrilátero Ferrífero region, including particle size distribution, Atterberg limits, specific gravity, compaction curves, water retention curves, and hydraulic conductivity.
- Investigate structural variations across samples by analyzing pore distribution, pore connectivity, particle aggregation, and surface texture using scanning electron microscopy (SEM) coupled with energy-dispersive spectroscopy (EDS).
- Assess the influence of structural variability on hydraulic behavior, focusing on the effects of void ratio, particle aggregation, and heterogeneity on hydraulic conductivity and water retention characteristics.
- Evaluate the role of void ratio during construction stages by analyzing its impact on seepage dynamics and stability, using simulations of tailings compacted at varying levels of compaction.
- Analyze the impact of material heterogeneity on seepage behavior and stability by incorporating the properties of different IOT samples into the modeling and assessment of filtered tailings stack construction.
- Investigate the effects of undercompaction, a hypothetical scenario in which off-specification tailings are compacted at higher void ratios due to reduced compaction efficiency during the rainy season, on seepage dynamics and overall stack stability through simulations of filtered tailings stack construction.
- Propose practical guidelines for optimizing compaction strategies, mitigating risks associated with seepage, elevated pore pressures, and slope instability, ensuring the sustainable performance of filtered tailings stacks.

4. THESIS ORGANIZATION

This thesis is structured into five chapters, organized as follows:

- *Chapter 1 – General Introduction:* this chapter provides a general introduction, including the justification for the research, the general and specific objectives of the study, and an outline of the thesis structure;
- *Chapter 2 – General Methodology:* presents the integrated experimental and numerical approach adopted in the study, with emphasis on the laboratory methods and modeling strategies used to investigate the hydromechanical behavior of filtered tailings;
- *Chapter 3 – Hydraulic Characteristics of Silt-Sized Iron Ore Tailings:* this research paper presents a comprehensive characterization of the basic geotechnical and hydraulic properties of iron ore tailings (IOT) from the Quadrilátero Ferrífero region, highlighting how variability in tailings and void ratios affects water retention and hydraulic conductivity. Experimental methods included the filter paper technique for determining water retention curves and constant head tests using flexible-wall permeameters for assessing hydraulic conductivity. Complementary chemical, mineralogical, and microstructural analyses were performed using X-ray diffraction (XRD) and scanning electron microscopy (SEM) coupled with energy-dispersive spectroscopy (EDS), providing deeper insights into the tailings' properties and their implications for geotechnical behavior.
- *Chapter 4 – Numerical Simulations of Filtered Tailings Stacks: Impact of Void Ratio, Heterogeneity, and Undercompaction on Hydraulic and Stability Behavior*: this research paper investigates the influence of unsaturated hydraulic properties on the behavior of filtered iron ore tailings (IOT) stacks, focusing on the effects of void ratio variations, material heterogeneity, and undercompaction during construction. Advanced numerical simulations with fully coupled seepage-deformation models are employed to examine transient hydraulic responses and slope stability under diverse operational scenarios and alternating wet and dry weather conditions. By exploring the interactions between seepage dynamics, pore pressure development, and mechanical stability, this study provides a comprehensive framework for optimizing the design, construction, and management of filtered tailings stacks, ensuring their safety and efficiency under diverse environmental challenges.
- *Chapter 5 – General Conclusions*: this chapter presents a summary of the overall conclusions of the research.

REFERENCES

ASSOCIAÇÃO BRASILERIA DE NORMAS TÉCNICAS (ABNT). **NBR 13028: Mining - Elaboration and presentation of design of tailings, sediments and water dams - Requirements**. Rio de Janeiro, 2024.

ASSOCIAÇÃO BRASILERIA DE NORMAS TÉCNICAS (ABNT). **NBR 13029: Mining - Elaboration and presentation of a mining waste disposal design**. Rio de Janeiro, 2024.

AUSTRALIAN NATIONAL COMMITTEE ON LARGE DAMS (ANCOLD). **Guidelines on tailings dams – Planning, design, construction, operation and closure**. 2019.

CACCIUTTOLO, C.; PÉREZ, G. C. **Practical Experience of Filtered Tailings Technology in Chile and Peru: An Environmentally Friendly Solution**. Minerals, v. 12, n. 7, p. 889. 2022.

CANADIAN DAM ASSOCIATION (CDA). **Technical bulletin: Application of dam safety guidelines to mining dams**. 2019.

CAO, B. *et al.* **Experimental Study on the Effect of Key Factors on the Soil–Water Characteristic Curves of Fine-Grained Tailings**. Frontiers in Environmental Science, v. 9. 2021.

CARMIGNANO, O. R. *et al.* **Iron Ore Tailings: Characterization and Applications**. Journal of the Brazilian Chemical Society, v. 32, n. 10, p. 1895–1911. 2021.

CARNEIRO, J. J. V. *et al.* **Characterization of an Iron Ore Tailing Sample and the Evaluation of Its Representativeness**. Geotechnical and Geological Engineering, v. 41, n. 5, p. 2833–2852. 2023.

CONSOLI, N. C. *et al.* **Behaviour of Compacted Filtered Iron Ore Tailings–Portland Cement Blends: New Brazilian Trend for Tailings Disposal by Stacking**. Applied Sciences, v. 12, n. 2, p. 836. 2022.

CRYSTAL, C.; HORE, C.; EZAMA, I. Filter-Pressed Dry Stacking: Design Considerations Based on Practical Experience. *In*: INTERNATIONAL CONFERENCE ON TAILINGS AND MINE WASTE. **Proceedings** […]. Keystone, Colorado, USA: UBC Studios, University of British Columbia, 2018. p. 209–2019.

DAVIES, M. **Filtered dry stacked tailings: the fundamentals**. *In*: NTERNATIONAL CONFERENCE ON TAILINGS AND MINE WASTE. **Proceedings** […]. Vancouver: University of British Columbia Library, 2011.

FARENZENA, H. P. *et al.* **Iron ore tailings stabilization with alternative alkali-activated cement for dry stacking: mechanical and microstructural insights**. Canadian Geotechnical Journal, v. 61, n. 4, p. 649–667. 2024.

FRÄNKLE, B. *et al.* **Copper tailings filtration: Influence of filter cake desaturation**. Minerals Engineering, v. 217. 2024.

FREDLUND, D. G.; RAHARDJO, H.; FREDLUND, M. D. **Unsaturated Soil Mechanics in Engineering Practice**. Hoboken, NJ, USA: John Wiley & Sons, Inc. 2012.

FURNELL, E. *et al.* **Dewatered and Stacked Mine Tailings: A Review**. ACS ES&T Engineering, v. 2, n. 5, p. 728–745. 2022.

GLOBAL INDUSTRY STANDARD ON TAILINGS MANAGEMENT (GISTM). **Global tailings review**. 2020.

GUEDES, J. P. C. *et al.* **Fibers Enhancing New Mine Waste-Based Alkaline-Activated Cement for Dry Stacking Purposes**. Journal of Materials in Civil Engineering, v. 36, n. 7. 2024.

INTERNATIONAL COMMISSION ON LARGE DAMS (ICOLD). **Bulletin No. 194: Tailings dam safety**. 2021.

KE, X.; CHEN, J.; SHAN, Y. **A new failure criterion for determining the cyclic resistance of low-plasticity fine-grained tailings**. Engineering Geology, v. 261. 2019.

MONTANI, J. L.; PORNILLOS, E.; MUNOZ, H. Geotechnical-geochemical and operational considerations for the application of dry stacking tailings deposits – state-of-the-art. *In*: INTERNATIONAL SEMINAR ON PASTE AND THICKENED TAILINGS: **Proceedings** [...]. Perth: Australian Centre for Geomechanics, 2013. p. 249–260.

OLDECOP, L.; RODARI, G. U**nsaturated mine tailings disposal**. Soils and Rocks, v. 44, n. 3, p. 1–12. 2021.

OLDECOP, L. A.; RODARI, G. J.; MUÑOZ, J. J. **Atmosphere Interaction and Capillary Barrier in Filtered Tailings.** Geotechnical and Geological Engineering, v. 35, n. 4, p. 1803–1817. 2017.

PIRES, K. de S. *et al.* **Mineralogical Characterization of Iron Ore Tailings from the Quadrilatero Ferrifero, Brazil, by Eletronic Quantitative Mineralogy**. Materials Research, v. 22. 2019.

RISSOLI, A. L. C. *et al.* **Dry Stacking of Filtered Iron Ore Tailings: Comparing On-Field Performance of Two Drying Methods**. Geotechnical and Geological Engineering, v. 42, n. 4, p. 2937–2948. 2024.

SAKO, C. H.; PABST, T. **Comparative geochemical evaluation of codisposal approaches for reactive filtered tailings deposition**. Cleaner Waste Systems, v. 5. 2023.

SCHAFER, H.; BEIER, N. **Estimating soil-water characteristic curve from soil-freezing characteristic curve for mine waste tailings using time domain reflectometry**. Canadian Geotechnical Journal, v. 57, n. 1, p. 73–84. 2020.

SEPÚLVEDA, R. G.; ROBERT, E. S.; CAMACHO-TAUTA, J. **Assessment of the Self-Compaction Effect in Filtered Tailings Disposal under Unsaturated Condition**. Minerals, v. 12, n. 4, p. 422. 2022.

SERVI, S. *et al.* **Mechanical response of filtered and compacted iron ore tailings with different cementing agents: Focus on tailings-binder mixtures disposal by stacking**. Construction and Building Materials, v. 349. 2022.

ULRICH, B. Practical thoughts regarding filtered tailings. *In*: International Conference on Paste, Thickened and Filtered Tailings. **Proceedings** […]. Perth: Australian Centre for Geomechanics, 2019. p. 71–79.

WILSON, G. **The new expertise required for designing safe tailings storage facilities**. Soils and Rock**s**, v. 44, n. 3, p. 1–8. 2021.

ZHANG, F.; WILSON, G. W.; FREDLUND, D. G. **Estimation of Permeability Function for Bulyanhulu Tailings**. Geotechnical Testing Journal, v. 42, n. 3. 2019.

CHAPTER 2

GENERAL METHODOLOGY

1. OVERVIEW OF THE RESEARCH APPROACH

The methodology adopted in this study combines comprehensive experimental testing with advanced numerical modeling to assess the hydromechanical behavior of filtered iron ore tailings. The research approach is divided into two main components. The first consists of a series of experimental procedures aimed at characterizing the geotechnical, chemical, mineralogical, and microstructural properties of representative tailings samples collected from the Quadrilátero Ferrífero region. These laboratory tests provide the necessary input parameters for the hydraulic and mechanical models, allowing for the interpretation of key material behaviors such as water retention, permeability, and structure-related porosity.

The second component focuses on the development of fully coupled seepage–deformation simulations to represent the transient response of tailings stacks during construction under variable climatic and operational conditions. The numerical models incorporate the experimental data to capture the interactions between seepage, pore pressure development, saturation, deformation, and slope stability. Together, the experimental and numerical methods provide a consistent framework for understanding how tailings variability, compaction efficiency, and environmental factors influence the performance and safety of filtered tailings stacks.

2. GEOTECHNICAL, CHEMICAL, AND MINERALOGICAL CHARACTERIZATION

Three distinct samples of filtered iron ore tailings—designated IOT10, IOT13, and IOT16—were obtained from a mining complex located in the Quadrilátero Ferrífero region, Minas Gerais, Brazil. The samples were collected directly at the outlet of the pressure belt filter system, prior to deposition and compaction within the dry-stacked tailings facility. To capture potential temporal variability in the physical and hydraulic behavior of the material, each sample was collected approximately six months apart, reflecting operational and seasonal changes in the tailings production process.

All materials were classified as disturbed samples and were handled in accordance with the preservation guidelines described in ASTM D4220/D4220M-14 (2014). Upon collection, the samples were sealed in airtight plastic bags and immediately transported to the laboratory, where they were gently disaggregated, homogenized, and stored in controlled conditions to prevent moisture exchange and oxidation.

Laboratory characterization included grain size distribution (ASTM D7928-17, 2021), Atterberg limits (ASTM D4318-17e1, 2018), and specific gravity tests (ASTM D854-23, 2023). These procedures were applied individually to each of the three tailings samples to capture potential differences in composition and to provide input for subsequent hydraulic and mechanical modeling. The classification of the tailings was performed using the Unified Soil Classification System (USCS) as described in ASTM D2487-17e1 (2025).

To investigate the effects of particle aggregation and the influence of deflocculants on particle size distribution, two procedures were adopted during combined particle size analysis:

- With deflocculant and mechanical dispersion: samples were soaked in a sodium hexametaphosphate solution for 24 hours to promote chemical deflocculation. They were then subjected to mechanical dispersion and manual agitation before the sedimentation phase.
- Without deflocculant and with mechanical dispersion: samples were immersed in distilled water without any chemical additive, followed by mechanical dispersion and manual agitation before sedimentation.

These procedures enabled the evaluation of natural aggregation effects and the estimation of the true fine fraction potentially masked by particle aggregation.

For chemical characterization, all samples were previously air-dried and sieved through a No. 10 (2.0 mm) mesh, following procedures recommended by EMBRAPA (2017). The tests included determination of pH in water and in KCl solution, and cation exchange capacity (CEC), which quantifies the total number of exchangeable cations retained on the surface of mineral particles (Ca^{2+}, Mg^{2+}, K^{+}, Na^{+}, H^{+}, and Al^{3+}), expressed in milliequivalents per 100 grams (meq/100g).

Mineralogical analysis was conducted using X-ray diffraction (XRD) on samples previously sieved through a No. 40 (0.425 mm) mesh. Oriented powder mounts were prepared by placing finely milled material onto glass slides with a uniform layer thickness (EMBRAPA,

2017). The resulting glass-mounted specimens—visible in Fig. 1—were analyzed using a Panalytical X'Pert Pro PW 3040/60 diffractometer equipped with a Co-Kα source (λ = 1.790269 Å), operating at 40 kV and 30 mA with 1800 W power. Scans were performed in step-scan mode from 5° to 80° 2θ, with a step size of 0.05° and a counting time of 2 seconds per step.

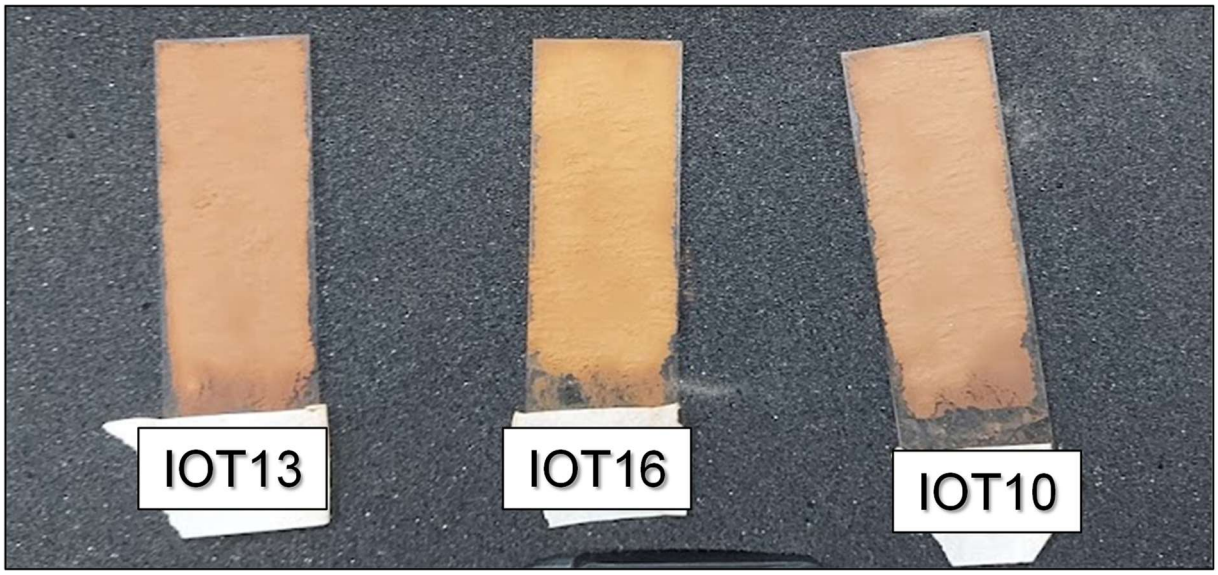

Fig. 1 Oriented powder mounts of IOT10, IOT13, and IOT16 samples on glass slides for XRD analysis

3. COMPACTION TESTS

To explore the range of void ratios that each material could realistically attain under field conditions—particularly in dry-stacked filtered tailings facilities— and to support the definition of input parameters for numerical modeling, specimens of IOT10, IOT13, and IOT16 were reconstituted using three levels of compaction energy: standard Proctor (~600 kJ/m³), intermediate (~1300 kJ/m³), and modified Proctor (~2700 kJ/m³). These procedures followed the Brazilian standard ABNT NBR 7182 (2016). For each energy level, compaction curves were established to determine the corresponding optimum moisture content (w_{opt}) and maximum dry unit weight (γ_{dmax}).

Furthermore, this experimental design enabled an indirect assessment of particle breakage associated with increasing compaction energy. To evaluate this effect, grain size distribution curves were determined for each sample (IOT10, IOT13, and IOT16) after compaction under standard, intermediate, and modified Proctor energies. All tests were conducted using a chemical dispersant to ensure full disaggregation of particles. The resulting curves allowed comparisons between pre- and post-compaction gradations and revealed shifts in particle size

distribution that may be attributed to crushing effects or the breakdown of particle aggregations, particularly under higher compaction efforts.

4. SPECIMEN RECONSTRUCTION

For each tailings material (IOT10, IOT13, and IOT16), specimens were reconstituted to represent three target compaction states corresponding to 75%, 85%, and 100% of the maximum dry density obtained from the respective standard Proctor compaction curves. These degrees of compaction were selected to reproduce field conditions ranging from ideal to suboptimal, particularly in scenarios where the tailings may not achieve full compaction due to construction-related constraints or unfavorable weather conditions, such as high rainfall. The molding water content for each set of specimens was kept constant and equal to the w_{opt} determined from the standard Proctor tests for each IOT sample.

Specimens used in the filter paper method to determine the water retention behavior were statically compacted into metal rings in a single layer, resulting in cylindrical samples approximately 50 mm in diameter and 20 mm in height (Fig. 2). For hydraulic conductivity tests, specimens were compacted in five layers within a cylindrical mold, producing samples with a diameter of 50 mm and a height of 100 mm (Fig. 3). In both cases, static compaction was performed under controlled conditions to ensure reproducibility of the target void ratios associated with each degree of compaction.

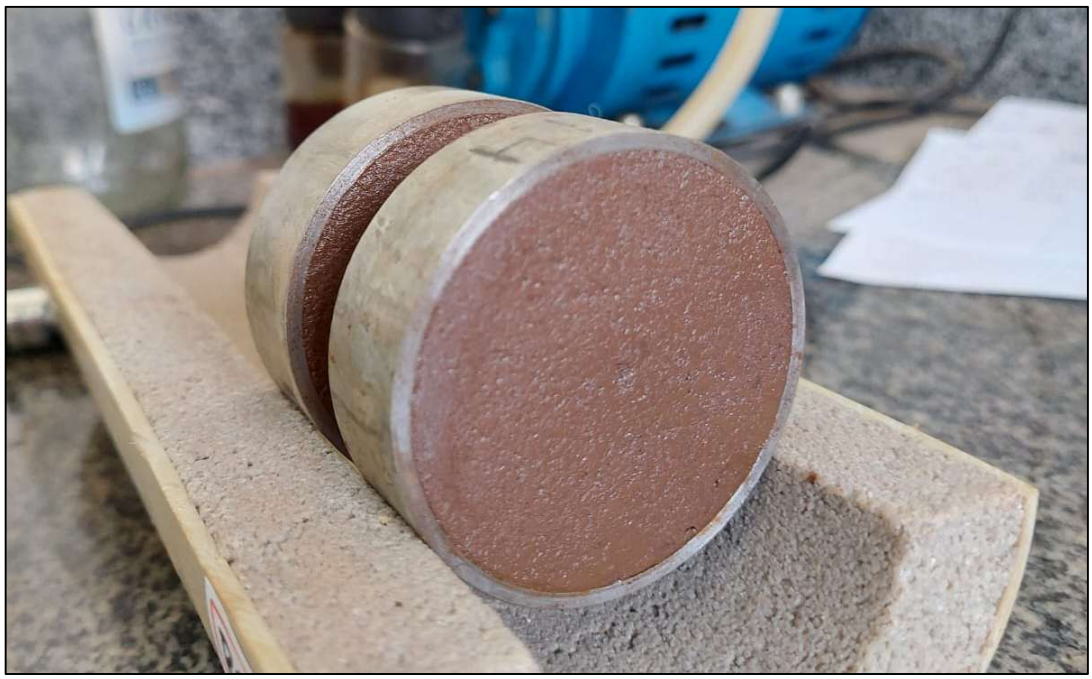

Fig. 2 Specimens molded for the filter paper test (Ø 50 mm × 20 mm)

Fig. 3 Specimens molded for hydraulic conductivity tests (Ø 50 mm × 100 mm)

5. MICROSTRUCTURAL INVESTIGATION

To investigate the microstructural arrangement of the filtered tailings and its evolution with increasing compaction, scanning electron microscopy (SEM) coupled with energy dispersive spectroscopy (EDS) was performed on reconstituted specimens of IOT10, IOT13, and IOT16, compacted to 75%, 85%, and 100% of their respective maximum dry densities as defined by standard Proctor tests.

Fragments were extracted from each compacted specimen and left to air dry at room temperature. After drying, the samples were mounted on 1 cm diameter aluminum stubs using a graphite-based conductive adhesive. The adhesive was applied laterally at the base of each fragment to promote good surface contact and mechanical stability. As shown in Fig. 4, multiple samples were mounted and properly labeled for identification.

Fig. 4 Mounted specimens of IOT tailings fixed on 1 cm stubs with graphite-based adhesive for SEM/EDS analysis

The mounted samples were then coated with a thin layer of gold using a sputter coater to form a conductive surface layer, minimizing the accumulation of electrostatic charges during scanning. Microstructural imaging and elemental mapping were performed using a Leo 1430VP scanning electron microscope (Carl Zeiss Ltd., Cambridge, England) equipped with an EDS detector.

The analysis focused on capturing high-resolution images of particle arrangements, surface textures, aggregation patterns, and pore distribution, supporting the interpretation of internal structure and interaction mechanisms relevant to the geotechnical behavior of the tailings.

6. FILTER PAPER METHOD

The water retention behavior of the filtered tailings was evaluated using the filter paper method, following the procedures described in ASTM D5298-16 (2016). This technique was applied to three representative IOT samples (IOT10, IOT13, and IOT16), each tested under three compaction conditions corresponding to 75%, 85%, and 100% of their respective maximum dry densities. Accordingly, three water retention curves were obtained for each sample, totaling nine curves. For each curve, approximately 15 reconstituted specimens were prepared to ensure sufficient distribution of measurements across a broad range of matric suction values.

All specimens were first saturated by capillary action (Fig. 5a) and then allowed to air-dry until reaching the target moisture condition, as determined by gravimetric monitoring. Once the target mass was reached, three Whatman No. 42 filter paper disks were applied to each specimen. The first disk, equal in diameter to the specimen, was placed in direct contact with

the compacted surface to create a uniform interface (Fig. 5b). A second disk, slightly smaller in diameter, was positioned centrally over the first and was used to measure the matric suction (Fig. 5c). Finally, a third disk—matching the first in size—was placed over the intermediate disk to protect it from external contact and contamination (Fig. 5d). The use of a smaller intermediate disk facilitated its retrieval after the equilibration period.

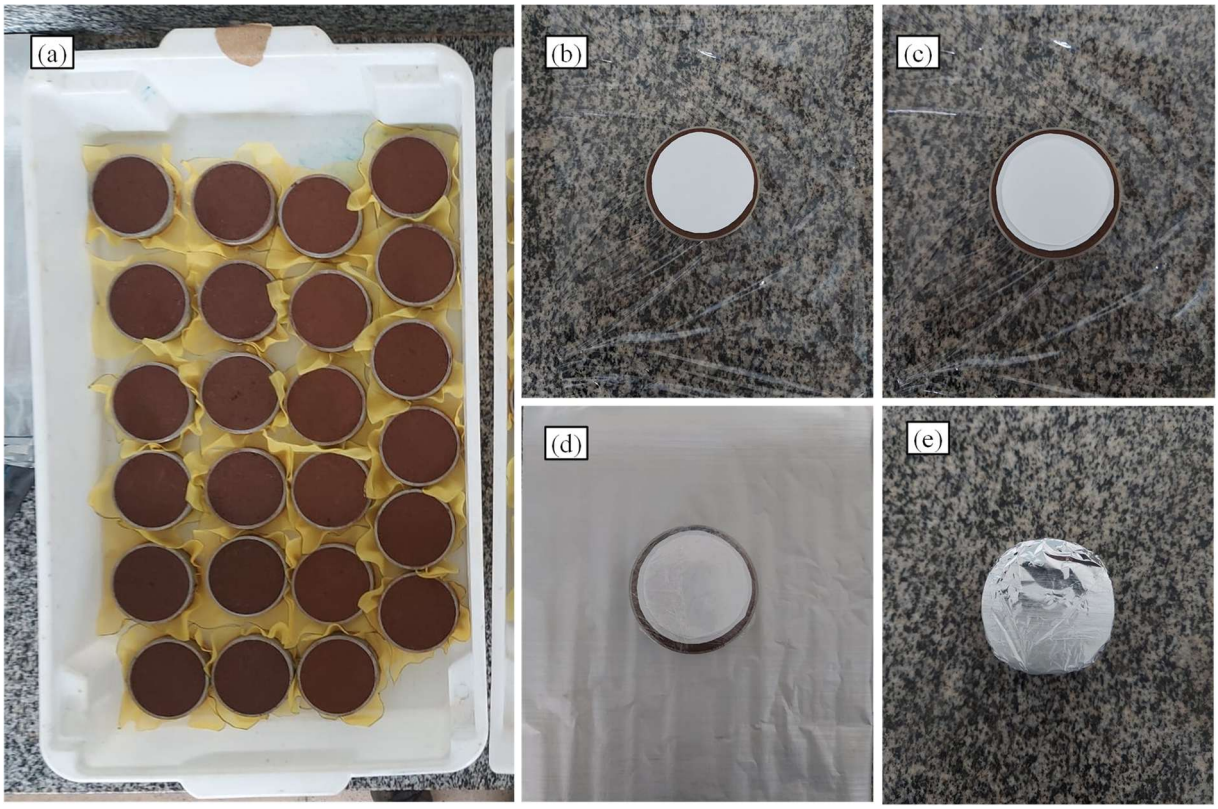

Fig. 5 Sequential steps of the filter paper method applied to IOT specimens. **a** saturation by capillary action; **b** initial filter paper disk; **c** intermediate filter paper disk; **d** final filter paper disk and specimen enclosed in PVC plastic film; **e** specimen wrapped in aluminum foil

After assembling the filter paper system, each specimen was carefully wrapped in two layers of PVC plastic film followed by an external layer of aluminum foil (Fig. 5e). This sealing process was essential to prevent moisture exchange with the environment during the equilibration stage. The wrapped specimens were then sealed inside a Styrofoam box (Fig. 6a), which was placed in a temperature-controlled incubator set to 25 ± 0.5 °C (Fig. 6b). The equilibrium period was maintained for 14 days to ensure moisture redistribution between the specimen and the filter paper disks.

Fig. 6 Equilibration stage for the filter paper test. **a** specimen in sealed Styrofoam box; **b** temperature-controlled incubator set to 25 ± 0.5 °C

Following equilibration, the intermediate filter paper disk was retrieved using tweezers and immediately weighed on a precision balance with 0.0001g resolution. To minimize moisture loss during handling, the weighing procedure was completed within 3 to 5 seconds. The gravimetric water content of the filter paper was then used to estimate the corresponding matric suction value, based on calibration equations for the Whatman No. 42 paper. Afterward, both the specimen and filter paper were oven-dried for confirmation of final moisture content.

Matric suction was determined from the gravimetric water content of the filter paper disks using the empirical calibration proposed by Chandler et al. (1992), as recommended by ASTM D5298-16 (2016). The relationship between water content and matric suction was used to define the water retention curves for each IOT samples.

The retention behavior was modeled using the multimodal van Genuchten approach (van Genuchten, 1980), as proposed by Durner (1994). Further details on the procedures, equations, and parameter fitting are provided in Chapter 3, Section 2.3.

7. HYDRAULIC CONDUCTIVITY TESTS

Saturated hydraulic conductivity tests were performed using a flexible-wall permeameter system (triaxial chamber), following the procedures described in ASTM D5084-16a (2016) for constant head testing. The objective was to assess how compaction state and confinement affect the permeability of filtered tailings.

For each IOT sample (IOT10, IOT13, and IOT16), three specimens were tested, corresponding to the initial compaction conditions of 75%, 85%, and 100% of their respective maximum dry densities. These specimens were first saturated through water percolation followed by the application of back pressure. During this process, a 5 kPa differential was maintained between the cell pressure and the back pressure. Back pressure increments of 25 kPa were applied until saturation was achieved, which was confirmed when the Skempton B-value exceeded 0.95.

Once saturated, the hydraulic conductivity of each specimen was initially measured under constant hydraulic gradients ranging between 5 and 25, depending on the compaction level. Flow was applied in the upward direction, and the percolated volume was recorded using a precision burette. The final value was taken as the average of at least four stabilized readings, without any evident increasing or decreasing trend.

After the initial measurement, the specimens were isotropically consolidated under confining stresses of 100, 200, 400, and 800 kPa. A volumetric stabilization period of 24 hours was adopted for each loading stage. Hydraulic conductivity was then reassessed under the same conditions as the pre-consolidation phase. This procedure yielded five conductivity measurements per specimen, totaling 15 values for each IOT sample and allowing evaluation across a wide range of void ratios.

To account for temperature effects on water viscosity, the conductivity values obtained during testing were corrected to 20°C using temperature correction factors, as recommended by ASTM D5084-16a (2016). Temperature was monitored at the beginning and end of each flow interval, and corrections were applied accordingly.

These measurements are essential for understanding how variations in compaction, particle arrangement, and mineralogy influence fluid flow through filtered tailings. The results not only quantify the hydraulic response under operationally relevant conditions but also serve

as critical input for numerical models simulating seepage behavior in dry-stacked disposal systems.

To represent the relationship between hydraulic conductivity and void ratio, an exponential fitting function was adopted. The modeling approach and parameter estimation procedures are described in detail in Chapter 3, Section 3.2.

To determine the unsaturated hydraulic conductivity function, this study employed the theoretical formulation proposed by Mualem (1976), integrated with the van Genuchten (1980) water retention model. The combined model describes the hydraulic conductivity as a function of matric suction and was calibrated using the parameters obtained from the retention curve fittings and the saturated conductivity data. For each IOT sample, the model parameters were adjusted according to the void ratio, enabling the estimation of unsaturated hydraulic conductivity curves for all simulated conditions. The adopted methodology and parameter sets are detailed in Chapter 4, Section 2.2.

8. NUMERICAL MODELING FRAMEWORK

The numerical modeling approach adopted in this study was developed to evaluate the hydromechanical behavior of filtered tailings stacks under transient conditions, accounting for construction stages, variable compaction, and seasonal climatic effects. Simulations were carried out using the RS2 software (Rocscience Inc.), which implements a fully coupled deformation–seepage formulation based on Biot's theory (Biot, 1941). This approach enables the simultaneous analysis of stress redistribution, suction preservation, transient pore pressure development, and deformation throughout stack construction and operation.

To support the numerical modeling, it was essential to define both saturated and unsaturated hydraulic and mechanical properties. The first step involved determining the saturated characteristics of the tailings, including permeability and shear strength. These were then combined with water retention behavior to enable the estimation of unsaturated hydraulic conductivity and shear strength through theoretical and empirical relationships (Sections 2.3 and 2.4 of Chapter 4), allowing the model to simulate transient hydromechanical conditions with void ratio-dependent behavior. Both saturated and unsaturated hydraulic properties were established based on laboratory tests, as described in Sections 2.2 and 2.3 of Chapter 2.

The elastoplastic model with the Mohr–Coulomb (MC) failure criterion was used to simulate the stress–strain behavior of the stack during staged construction. Effective shear

strength parameters (ϕ' and c') were adopted from Oliveira (2021), based on consolidated isotropically drained and undrained triaxial tests (CID_{sat} and CIU_{sat}, respectively) performed on the IOTmech sample. The stiffness modulus (E_{50}) was obtained from the CID_{sat} results. Although not part of the present experimental program, the IOTmech sample was collected from the same filtration plant—and under the same sampling procedures, including collection directly from the pressure belt discharge point—as the IOT10, IOT13, and IOT16 samples analyzed in this study. The constitutive parameters adopted for the MC model are summarized in Section 2.4 of Chapter 4.

The modeling strategy—detailed in Section 2.5 of Chapter 4—involved the definition of the geotechnical section, finite element mesh refinement, staged construction, initial hydraulic conditions, and climatic boundary inputs. Discharge sections were incorporated to evaluate seepage throughout construction, while internal control points were placed to capture variations in saturation, pore pressure, and total displacement near the most critical zone of the stack.

As part of this framework, the mechanical stability of the stack was assessed through slope stability analyses performed using the Slide2 limit equilibrium software, also developed by Rocscience Inc. These analyses incorporated pore pressure grids generated during the construction stages in the RS2 simulations, ensuring that the hydraulic regime was consistently reflected in the safety evaluations across different compaction and environmental scenarios.

The modeling framework was applied to simulate a series of operational scenarios involving variation in compaction levels, material heterogeneity, and the effects of undercompaction during rainy periods. The selection criteria and specific characteristics of each simulated case are presented in Section 2.3 of Chapter 4, and a summary table (Table 1) is provided to guide the interpretation of the numerical results discussed in Chapter 4.

The IOT10-100% scenario, compacted to the maximum dry density obtained from the standard Proctor test, was adopted as the reference case for comparison with all other simulated conditions. The void ratios listed in Table 1 were used not only to define the initial porosity of each modeled layer but also to assign the corresponding saturated and unsaturated geotechnical properties of the tailings. The empirical functions and procedures used to relate void ratio to hydraulic conductivity, water retention, and unsaturated shear strength are detailed in Sections 2.3 and 2.4 of Chapter 4.

Table 1 Summary of simulated scenarios, associated IOT samples, and void ratios adopted in the numerical modeling

Scenario type	Sample designation	Void ratio (e)
Variation in void ratio	IOT10-100%	0.47
	IOT10-90%	0.64
	IOT10-80%	0.84
Tailings heterogeneity	IOT10-100%	0.47
	IOT13-100%	0.58
	IOT16-100%	0.72
Undercompaction during rainy season	IOT10-100%	0.47
	IOT10-90/100%	0.64/0.47
	IOT10-80-100%	0.84/0.47

9. GENERAL METHODOLY WORKFLOW

To provide a comprehensive overview of the integrated approach adopted in this research, Fig. 7 summarizes the general methodological framework employed throughout the study. Although visually organized into two main components—experimental characterization and numerical modeling—these stages are deeply interconnected. The diagram outlines the complete sequence of experimental procedures—ranging from sample collection and characterization to compaction and hydraulic testing—followed by the numerical modeling framework used to simulate the hydromechanical behavior of filtered tailings stacks. This integrative approach enabled the evaluation of critical factors such as void ratio, material variability, and climatic effects on seepage and slope stability in filtered tailings stacks.

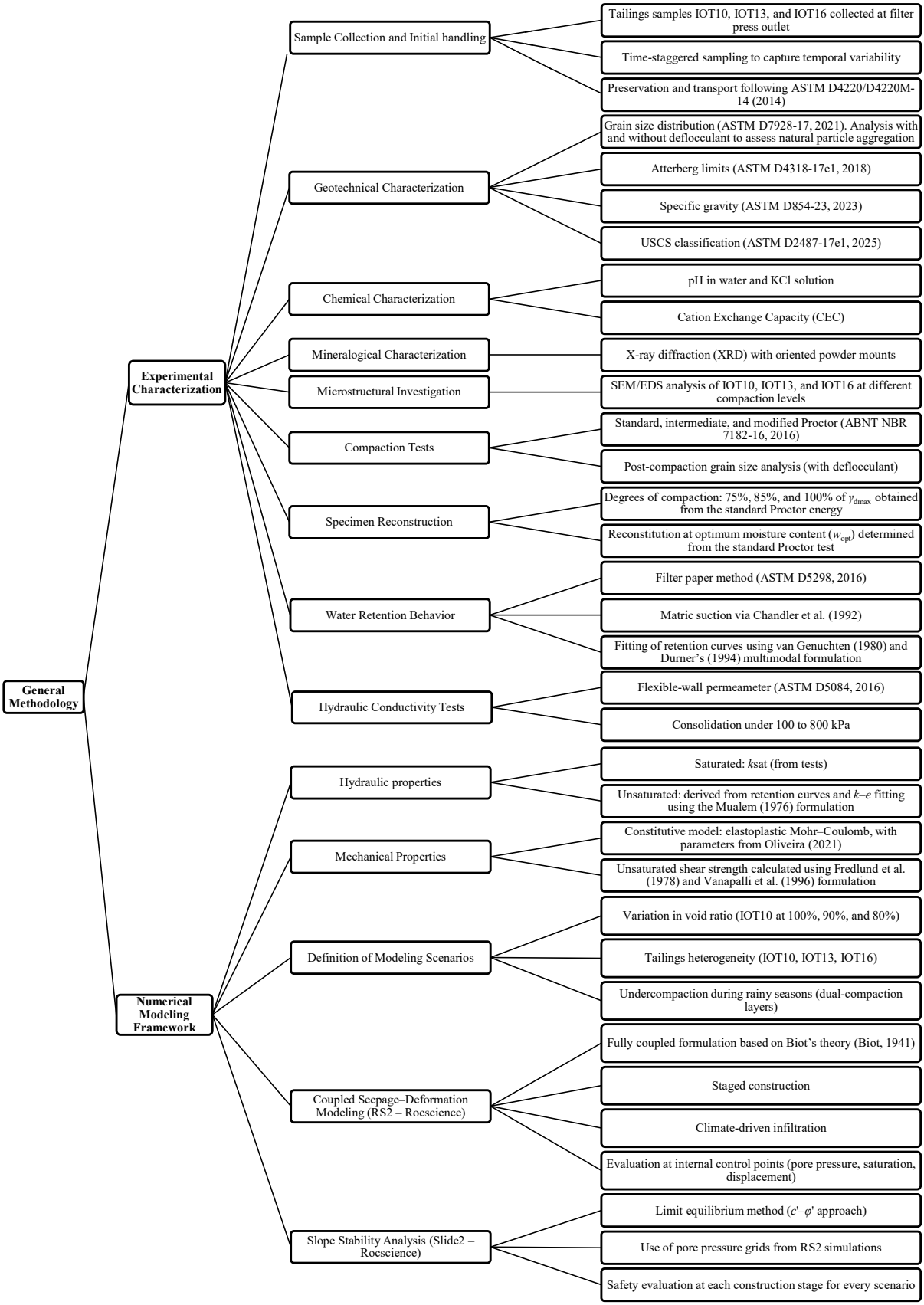

Fig. 7 Overview of the general methodology, including experimental procedures and numerical modeling steps used in this study.

REFERENCES

ASSOCIAÇÃO BRASILERIA DE NORMAS TÉCNICAS (ABNT). **NBR 7182-16: Compaction test**. Rio de Janeiro, 2016.

AMERICAN SOCIETY FOR TESTING AND MATERIALS (ASTM). **D2487-17: Standard Practice for Classification of Soils for Engineering Purposes (Unified Soil Classification System)**. West Conshohocken, 2025.

AMERICAN SOCIETY FOR TESTING AND MATERIALS (ASTM). **D4220/D4220M-14: Standard practices for preserving and transporting soil samples**. West Conshohocken, 2014.

AMERICAN SOCIETY FOR TESTING AND MATERIALS (ASTM). **D4318-17e1: Standard test methods for liquid limit, plastic limit, and plasticity index of soils**. West Conshohocken, 2018.

AMERICAN SOCIETY FOR TESTING AND MATERIALS (ASTM). **D5084-16a: Standard test methods for measurement of hydraulic conductivity of saturated porous materials using a flexible wall permeameter**. West Conshohocken, 2016.

AMERICAN SOCIETY FOR TESTING AND MATERIALS (ASTM). **D5298-16: Standard test method for measurement of soil potential (suction) using filter paper**. West Conshohocken, 2016.

AMERICAN SOCIETY FOR TESTING AND MATERIALS (ASTM). **D7928-17: Standard test method for particle-size distribution (gradation) of fine-grained soils using the sedimentation (hydrometer) analysis**. West Conshohocken, 2021.

AMERICAN SOCIETY FOR TESTING AND MATERIALS (ASTM). **D854-23: Standard test methods for specific gravity of soil solids by the water displacement method**. West Conshohocken, 2023.

BIOT, M. A. **General theory of three-dimensional consolidation.** Journal of Applied Physics, v. 12, p. 155–164. 1941.

CHANDLER, R. J. *et al*. **A low-cost method of assessing clay desiccation for low-rise buildings**. Civil Engineering – Institution of Civil Engineers, p. 82–89. 1992.

DURNER, W. **Hydraulic conductivity estimation for soils with heterogeneous pore structure**. Water Resources Research, v. 30, p. 211–223. 1994.

EMPRESA BRASILEIRA DE PESQUISA AGROPECUÁRIA (EMBRAPA). **Manual of Methods of Soil Analysis**. Brasília, 2017.

FREDLUND, D. G.; MORGENSTERN, N. R.; WIDGER, R. A. **The shear strength of unsaturated soils**. Canadian Geotechnical Journal, v. 15, p. 313–321. 1978.

MUALEM, Y. **A new model for predicting the hydraulic conductivity of unsaturated porous media**. Water Resources Research, v. 12, p. 513–522. 1976.

OLIVEIRA, A. H. C. **Stress-strain analysis in a filtered tailing pile of large dimensions**. 2021. Dissertation (Master's in Civil Engineering) – Federal University of Viçosa, Viçosa, MG, 2021.

VANAPALLI, S. K.; FREDLUND, D. G.; PUFAHL, D. E.; CLIFTON, A. W. **Model for the prediction of shear strength with respect to soil suction**. Canadian Geotechnical Journal, v. 33, p. 379–392. 1996.

VAN GENUCHTEN, M. T. **A closed-form equation for predicting the hydraulic conductivity of unsaturated soils**. Soil Science Society of America Journal, v. 44, p. 892–898. 1980.

CHAPTER 3

HYDRAULIC CHARACTERISTICS OF SILT-SIZED IRON ORE TAILINGS [1]

Abstract Stacked tailings have become increasingly popular in recent years as a more environmentally friendly option for tailings disposal. However, the design and assessment of stacked tailings present unique challenges due to their unprecedented heights and the wide range of factors that affect their behavior, including particle types and sizes, environmental and operational conditions, and post-compaction states. To further understand their behavior, this paper presents a comprehensive characterization of the geotechnical and hydraulic properties of three iron ore tailings (IOT) samples, exploring how their water retention characteristics and hydraulic conductivity are affected by the tailings' variability and void ratio. Using the filter paper method and constant head tests in a flexible wall permeameter, the water retention characteristics and hydraulic conductivity were obtained. Chemical-mineralogical composition and microstructural analyses were conducted using X-ray diffraction (XRD) and scanning electron microscopy (SEM) couple with energy dispersive spectroscopy (EDS). The results revealed that slight variations in particle size distribution can significantly influence the water retention characteristics and hydraulic conductivity of IOT samples. A dual porosity model was used to account for the aggregation of fine particles, and a strong linear relationship between void ratio and both macrostructure and microstructure fitting parameters of the water retention curves was found. Additionally, an exponential function was observed to display how the reduction of void ratio leads to a decrease in hydraulic conductivity. This research provides insight into the distinct properties of iron ore tailings and can be used to enhance the design and evaluation of stacked tailings.

Keywords stacked tailings · iron ore tailings · water retention characteristics · hydraulic conductivity · dual porosity

1. Introduction

Stacked tailings, commonly referred to as filtered tailings or dry stacked tailings, have become increasingly popular in recent years as a more environmentally friendly alternative to

[1] Original paper in *Geotechnical and Geological Engineering*. Accepted on January 24, 2024. Published online on March 7, 2024. First author: Sérgio Leandro Scher Dis Neto. https://doi.org/10.1007/s10706-024-02755-y.

conventional disposal of slurried material in tailings dams (Furnell et al. 2022). New technologies in filtration, reduced footprint for tailings storage, improved water recovery during ore beneficiation, and social and regulatory pressure have all contributed to making stacked tailings a feasible and attractive choice for tailings management (Liu et al. 2019; Sepúlveda et al. 2022; Cacciuttolo and Valenzuela 2022). Dewatering of tailings also reduces the risk of seepage pollution and internal erosion, as well as minimizes the risk of liquefaction associated with the large volumes of water and low densities present in tailings dams (Oldecop et al. 2017; Ke et al. 2019; Sadrekarimi and Riveros 2020; Riveros and Sadrekarimi 2021; Cacciuttolo and Pérez 2022)

From a geotechnical perspective, the primary benefit of stacked tailings is the dewatering process that allows for tailings disposal close to the optimum water content, attained through standard Proctor tests (Davies 2011; Ulrich 2019). This results in better compaction, which in turn increases stiffness and shear strength of the deposit (Amoah et al. 2018). However, the output water content of tailings can vary significantly due to the variability of tailings grain size distribution and mineralogical composition, which affects the filter's effectiveness (Crystal et al. 2018). Another crucial consideration, emphasized by Rissoli et al. (2023), is that the output water content of filtered material is strongly influenced by weather conditions, particularly during the rainy season in the southeast of Brazil.

Even if it was possible to ensure that tailings remain unsaturated after dewatering, there are still potential issues that could cause an excess of water. These include rainfall events, a sudden increase in ore processing rate, or a reduction of deposition area due to construction issues (Montani et al. 2013; Marques et al. 2020). Additionally, as the deposit rises, the overburden stresses will intensify, leading to an increase in the saturation degree due to volume reduction (Ulrich and Coffin 2013). However, Oldecop and Rodari (2021) suggested that stacked tailings are the most likely disposal technology to achieve an unsaturated state, particularly if free drainage is provided by incorporating coarse-grained materials such as waste rock layers between tailing layers.

The water retention curve is a useful and cost-effective method for accounting for the unsaturated behavior of stacked tailings. Combined with the saturated properties, this approach involves the use of theoretical and empirical relationships to predict the unsaturated hydraulic conductivity, shear strength and volume change properties of the tailings (Vanapalli et al. 1999; Fredlund et al. 2012; Schafer and Beier 2020).

Nevertheless, the complexity of designing and assessing stacked tailings has grown significantly, as tailings stacks reach unprecedented heights, such as over 100 m in Brazil (Consoli et al. 2022). Their behavior is further complicated by the diversity in particle types and sizes, as well as environmental and operational factors. Furthermore, with the likely variability of the post-compaction states of the stacked tailings, additional effort must be taken to determine the parameters of models that accurately capture the changes in their behavior caused by changes in the void ratio.

In view of the previous considerations, this paper first characterizes iron ore tailings (IOT), tailings designed for filtered staking, based in their basic geotechnical properties, chemical and mineralogical composition; and then describes an experimental study on the water retention characteristics and hydraulic conductivity of them. The three objectives of this paper are (1) to assess the variability of the IOT samples based on their chemical and mineralogical composition, and basic geotechnical and hydraulic properties; (2) to investigate how void ratio variation affects the hydraulic properties of IOT samples; (3) to explicitly recognize the dependency of the hydraulic properties of IOT samples on void ratio using established empirical equations. The results of the experimental study are validated by microstructural analysis and compared with published results to gain insight into the distinctive properties of these materials.

2. Materials and Methods

2.1 Iron Ore Tailings

Three representative samples of filtered iron ore tailings were obtained from a mining complex situated in the Quadrilátero Ferrífero, Minas Gerais, Brazil. Disturbed samples, collected and transported in airtight plastic bags, as outlined in ASTM D4220/D4220M-14 (2014), were obtained directly from the pressure belt filter before being deposited and subsequently compacted within a dry stacking tailings deposit. In an effort to account for possible geotechnical variability in the stacked tailings, samples were collected at approximately 6-month intervals. Particle size distribution, Atterberg limits, and specific gravity were determined using the procedures outlined in ASTM D7928-17 (2021), ASTM D4318-17e1 (2018), and ASTM D854-23 (2023), respectively.

The classification of the iron ore tailing (IOT) samples was based on their clay content, determined from particle size distribution curves using chemical dispersant (WD). This information is presented in Fig. 1 and Table 1, where IOT10 had 10% (IOT10-WD), IOT13 had

12.8% (IOT13-WD), and IOT16 had 16.2% clay content (IOT16-WD). Curves obtained without dispersant (WOD) correspond to samples IOT10-WOD, IOT13-WOD, IOT16-WOD in Fig. 1 and Table 1. Additional geotechnical-chemical properties of the IOT samples can be found in Table 2.

Fig. 1 also shows the particle size curves for the IOT samples after being compacted with the standard Proctor (approx. 600 kJ/m³) and modified Proctor (approx. 2700 kJ/m³) compaction energy levels. These correspond to samples IOT10-S, IOT13-S and IOT16-S, and IOT10-M, IOT13-M and IOT16-M, respectively. An intermediate compaction energy level (approx. 1300 kJ/m³) was also used and referred to samples IOT10-I, IOT13-I, and IOT16-I. All of these particle size curves were obtained using chemical dispersant.

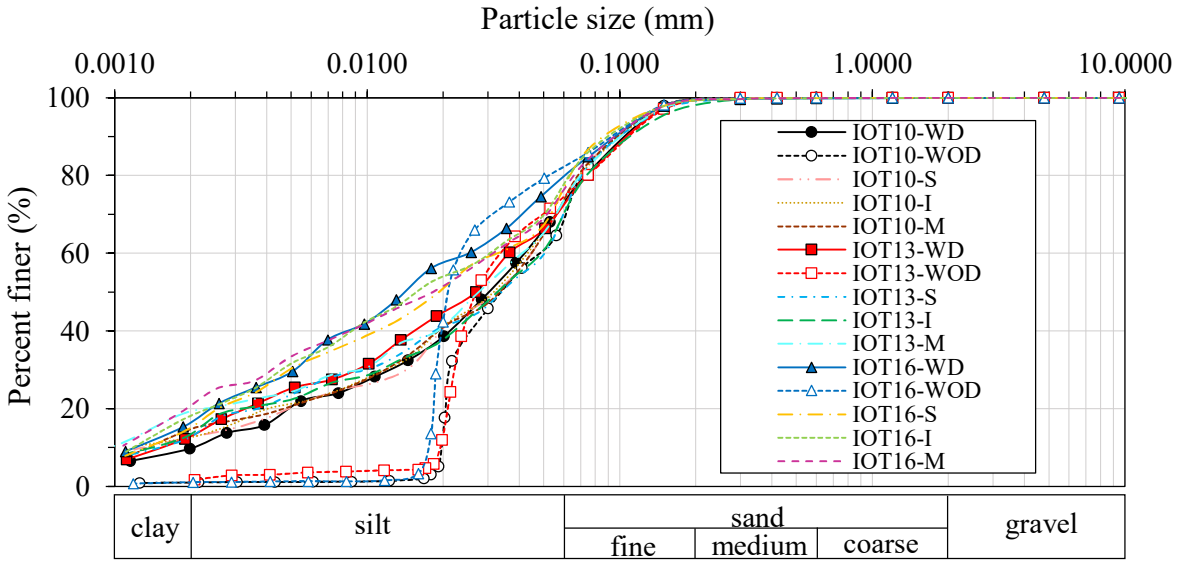

Fig. 1 Particle size distribution curves of the IOT samples

Table 1 Particle size fractions and geotechnical properties inferred from particle size distribution curves

IOT	Clay	Silt	Fine sand	Medium sand	Coarse sand	Gravel	D_{50}	C_U	C_C	Fine content
	< 0.002	0.002 - 0.06	0.06 - 0.2	0.2 - 0.6	0.6 - 2.0	> 2.0				< 0.075 mm
	mm	mm	mm	mm	mm	mm	mm	-	-	%
IOT10-WD	10	63	27	0	0	0	0.029	20.83	1.66	80.7
IOT10-WOD	1.1	67.7	31.2	0	0	0	0.034	2.41	0.5	82.7
IOT10-S	12.6	61.2	25.6	0.6	0	0	0.031	36.62	3.84	83.1
IOT10-I	12.7	60.9	26.1	0.3	0	0	0.033	37.65	2.68	82.8

IOT	Clay	Silt	Fine sand	Medium sand	Coarse sand	Gravel	D_{50}	C_U	C_C	Fine content
	< 0.002	0.002 - 0.06	0.06 - 0.2	0.2 - 0.6	0.6 - 2.0	> 2.0				< 0.075 mm
	mm	mm	mm	mm	mm	mm	mm	-	-	%
IOT10-M	14.8	59	26.2	0	0	0	0.033	33.53	2.38	83.1
IOT13-WD	12.8	59.6	27	0.6	0	0	0.026	22.14	1.43	80.2
IOT13-WOD	1.8	72.9	24.7	0.6	0	0	0.027	1.7	0.73	80.2
IOT13-S	12.8	57.6	28.6	1	0	0	0.034	36	1.19	82.4
IOT13-I	13.5	56.8	27.8	1.9	0	0	0.033	37	1.83	80.6
IOT13-M	19.3	54.3	25.8	0.6	0	0	0.028	45.83	2.18	82.4
IOT16-WD	16.2	63.8	19.4	0.6	0	0	0.014	20.95	0.87	84.9
IOT16-WOD	1.3	81.1	17.6	0	0	0	0.021	1.33	0.85	85.9
IOT16-S	15.1	61.7	22.5	0.7	0	0	0.019	24.46	0.58	86.9
IOT16-I	18.2	59.6	21.5	0.7	0	0	0.016	24.9	0.6	86.1
IOT16-M	20.7	55.6	23.2	0.5	0	0	0.018	29.69	0.55	84.1

D_{50} represents the average particle size. C_U stands for the coefficient of uniformity, while C_C stands for the coefficient of curvature

Table 2 Geotechnical-chemical properties of the IOT samples

	IOT 10	IOT13	IOT16
Liquid limit - w_L (%)	20	23	27
Plastic limit - w_P (%)	14	12	17
Plasticity index - PI (%)	6	11	10
Specific gravity - G_s	3.21	3.33	3.36
pH distilled water	6.66	6.49	6.37
pH KCl solution	6.48	6.27	6.3
CEC (meq/100 g)	0.77	0.63	0.86
USCS classification	CL-ML	CL	CL

From Fig. 1 and Table 1, it is evident that samples IOT10-WD, IOT13-WD, and IOT16-WD have a high fine content (over 80%), with predominance of silt-sized particles. It is noteworthy that the <75μm particle fraction of sample IOT10-WD has larger particles than sample IOT13-WD, which has larger particles than IOT16-WD, as evidenced by the particle size distribution curves of each sample (Fig. 1), with IOT10-WD's curve lying below the IOT13-WD's curve, which lies below that of IOT16-WD. Additionally, the increase in the average particle size D_{50} from sample IOT16-WD to IOT10-WD, as shown in Table 1, further confirms this trend.

This is in line with the findings of Crystal et al. (2018), who observed that most of the filtered tailings had a high fine content, with the majority of particles being silt-sized. Carneiro et al. (2023) gathered a database of the main geotechnical characteristics of 40 particle size distribution curves referring to various silt-sized iron ore tailings collected over the last two decades in the Quadrilátero Ferrífero region, which are presented in Table 3.

Table 3 Particle size fractions and geotechnical properties of silt-sized IOT from the Quadrilátero Ferrífero region (Carneiro et al. 2023)

IOT (40)	Clay	Silt	Fine sand	Medium sand	Coarse sand	Gravel	D_{50}	C_U	C_C	Fine content
	< 0.002 mm	0.002 - 0.06 mm	0.06 - 0.2 mm	0.2 - 0.6 mm	0.6 - 2.0 mm	> 2.0 mm	mm	-	-	< 0.075 mm %
Mean	7.3	53.9	33	4.7	0.5	0.7	0.05	22.9	5.6	72.2
Standard Deviation	6	15.5	13	5.9	1.3	2.9	0.02	29.1	7.9	14.2
Maximum	19.5	82	55	23	5	18	0.12	106	31.7	100
Minimum	0	23	10	0	0	0	0.01	2.3	0.1	50

The results of IOT10-WD, IOT13-WD, and IOT16-WD in Table 1 are consistent with the mean values presented in Table 3, given their high variability. Despite this, Carneiro et al. (2023) has noted that the results in Table 3 were mostly from particle size distributions with a poorly graded composition, lacking in fine silt and clay content. In contrast, the samples IOT10-WD IOT13-WD, and IOT16-WD have their particles well distributed in the fine content range (<75μm), as shown in Fig. 1. Coefficients of uniformity (C_U) and curvature (C_C) in Table 1 also indicated this. All IOT samples have high C_U values and C_C values between 1 and 3, with the exception of sample IOT16-WD. Similar results of well-graded silt-sized iron ore tailings have been reported by other researchers (Gomes et al. 2016; Pires et al. 2019; Li and Coop 2019; Yang et al. 2020; Deng et al. 2021; Mmbando et al. 2023).

Table 2 reveals that sample IOT10 has a very low plasticity. Samples IOT13 and IOT16 have higher liquid limit and plasticity index as they contain higher clay content, but yet they remain as low-plastic materials. This can also be inferred based on their corresponding classifications in the Unified Soil Classification System (USCS) in Table 2. It is known that silt-sized iron ore tailings usually have either low-plastic (Jeong 2014; Hu et al. 2017; Robertson et al. 2019; Oldecop and Rodari 2021; Yüksek 2022; Guedes et al. 2024) or non-plastic (Reid et al. 2018, 2022; Barati et al. 2020; Mendes et al. 2021; Santos Junior et al. 2022;

Rissoli et al. 2023) behavior, with the clay content being a key determinant in the plasticity of these materials.

Fig. 2 displays the compaction curves generated following the test procedures outlined in ABNT NBR 7182 (2016) for the mentioned compaction energy levels. Table 4 presents the compaction parameters corresponding to the optimum conditions.

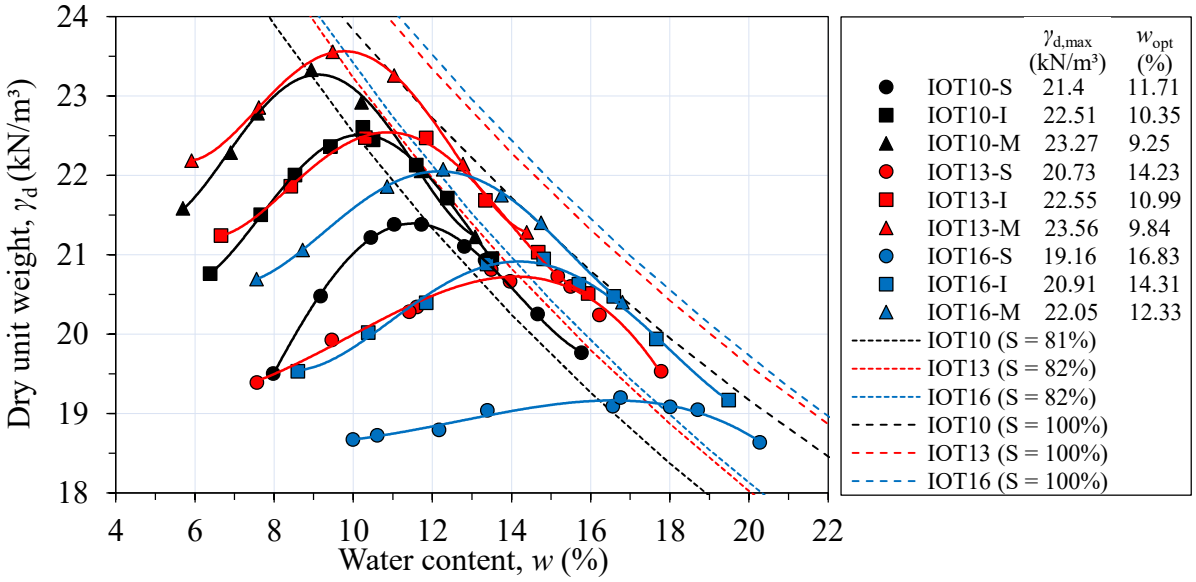

Fig. 2 Compaction curves of the IOT samples

Table 4 Compaction parameters corresponding to the optimum conditions

	Energy of compaction					
	Standard		Intermediate		Modified	
IOT	$\gamma_{d,max}$ (kN/m³)	w_{opt} (%)	$\gamma_{d,max}$ (kN/m³)	w_{opt} (%)	$\gamma_{d,max}$ (kN/m³)	w_{opt} (%)
IOT 10	21.40	11.71	22.51	10.35	23.27	9.25
IOT 13	20.73	14.23	22.55	10.99	23.56	9.84
IOT 16	19.16	16.83	20.91	14.31	22.05	12.33
Mean	20.4	14.3	22.0	11.9	23.0	10.5
Standard Deviation	1.1	2.6	0.9	2.1	0.8	1.6

The results depicted in Fig. 2 and Table 4 reveal that as the compaction energy is raised, the maximum dry unit weight ($\gamma_{d,max}$) increases and the optimum water content (w_{opt}) decreases, with a degree of saturation around 82% for IOT13 and IOT16 and 81% for IOT10. When tested with the standard Proctor energy level, higher clay content caused lower $\gamma_{d,max}$ and higher w_{opt}. However, with intermediate and modified energy levels, IOT10 and IOT13 had similar $\gamma_{d,max}$ and w_{opt} values, while IOT16 had the lowest $\gamma_{d,max}$ and highest w_{opt} of the group. These variations

in the behavior of IOT16 compared to IOT10 and IOT13 did not appear to be significant, given the minimal standard deviation of the compaction parameters, as illustrated in Table 4.

Overall, compaction energy influences the particle size distribution of all IOT samples, particularly in the fine fraction. There is a consistent rise in clay content and a decrease in silt content with increasing compaction energy, as depicted in Fig. 1 and outlined in Table 1. No distinct pattern is observed for medium and coarse sand fractions across all IOT samples, as detailed in Table 1. This behavior is similarly reflected in the D_{50}, C_U, and C_C for all IOT samples, as presented in Table 1.

However, only the IOT13 samples show a gradual reduction in fine sand content with increasing compaction energy (Fig. 1 and Table 1). This phenomenon may be associated with the formation of aggregations of fine sand size, which were progressively eliminated as the compaction energy intensified. As will be discussed later, the clay and silt-sized particles present in all IOT samples aggregate to create larger particles. In the case of IOT13, some of these aggregations seem comparable in size to fine sand particles, although, for the majority of IOT samples, most aggregations occur within the silt size range.

Fig. 3 illustrates the X-ray diffractograms and the identified phases for fine fraction of the IOT samples, obtained with a multifunctional Panalytical X'Pert Pro PW 3040/60 diffractometer equipped with a 1800W, 60kV cobalt tube (Co-Kα radiation, λ = 1.790269 Å) operated at 40 kV and 30 mA. Scans were performed in a step-by-step mode from 5º to 80º 2θ with 0.05º increments per 2 s.

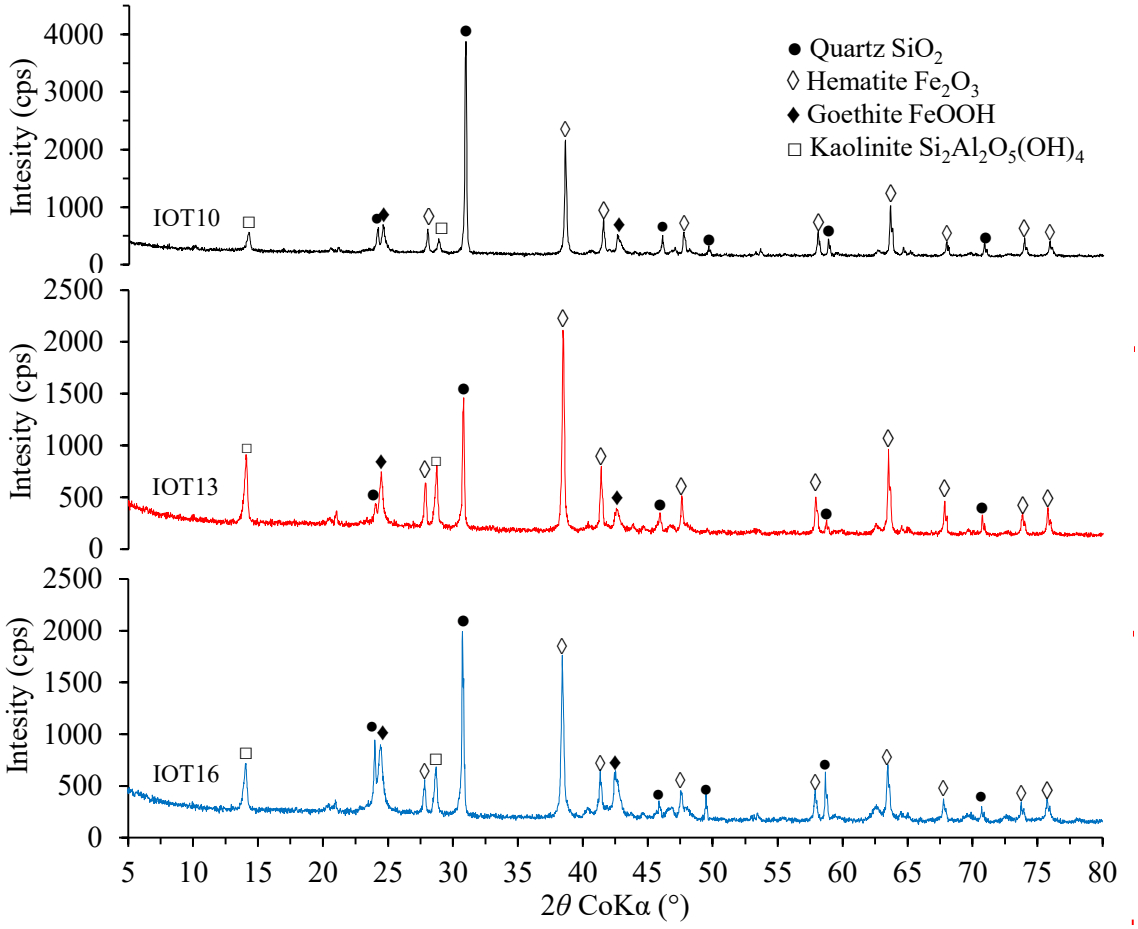

Fig. 3 X-ray diffractograms of the IOT samples

X-ray diffraction analysis of the IOT samples (Fig. 3) reveals the presence of four main phases: quartz and hematite, with higher intensity peaks, as well as goethite and kaolinite, with lower intensity peak. These finding are consistent with the literature, which indicates that the most abundant minerals in iron ore tailings are iron-rich minerals such as hematite and goethite, as well as quartz (McDonald et al. 2016; Dauce et al. 2019; Freitas et al. 2019; Prates et al. 2020; Lima et al. 2020; Rocha et al. 2022). Moreover, X-ray diffraction analysis reveals the presence of kaolinite and gibbsite in lower concentrations in tailings of this nature (Dash et al. 2011; Giri et al. 2011; Pires et al. 2019; Silva and Paiva 2020; Krishna et al. 2021; Souza et al. 2021; Pinto et al. 2022; Ferreira et al. 2022).

Fig. 3 illustrates that silica, and iron and aluminium oxides-hydroxides are the primary components of iron ore tailings, which are commonly found in natural structured soil as laterites (Ng et al. 2019; Oluremi et al. 2019; Gao et al. 2021; Araujo et al. 2021; Santoro et al. 2022). According to Robertson et al. (2019), particle bonding is prevalent in fine tailings due to clay-size iron oxides-hydroxides particles. X-ray diffraction (XRD) and Scanning Electron

Microscopy (SEM) techniques employed by Robertson et al. (2019) showed that higher levels of goethite were present in surface samples, indicating weathering and oxidation of the iron, resulting in particle bonding. Li and Coop (2019) also found particle bonding in coarser fractions of iron ore tailings, as evidenced by aggregated silty particles in and between sandy particles.

SEM/Energy dispersive spectroscopy (EDS) mapping images of iron ore tailings have revealed the presence of smaller agglomerated hematite particles adhering to the surface of larger particles (Sakthivel et al. 2009; Yuan et al. 2021; Prates et al. 2023). Fig. 4 illustrates a SEM/EDS mapping image of sample IOT10, which was compacted with a void ratio of 0.96. That was acquired using a Leo 1430VP scanning electron microscope coupled with EDS (Carl Zeiss Ltd, Cambridge, England).

The mapping of the main elements of the phases found in XRD analysis (Fig. 3) showed a high presence of iron minerals (Fig. 4g) and a lesser amount of kaolinite (Fig. 4e), which were aggregated to form rounded larger particles that were spread across the observed surface (Fig. 4a and 4c). This resulted in larger pores (2-macropores) between the aggregations (Fig. 4a). Furthermore, the fine particles of iron ore tailings were found to be agglomerated on the surface of large particles of quartz (Fig. 4f), indicating particle bonding. Fig. 4b also illustrates the particle aggregations and the pores between (2-macropores) and within them (3-micropores).

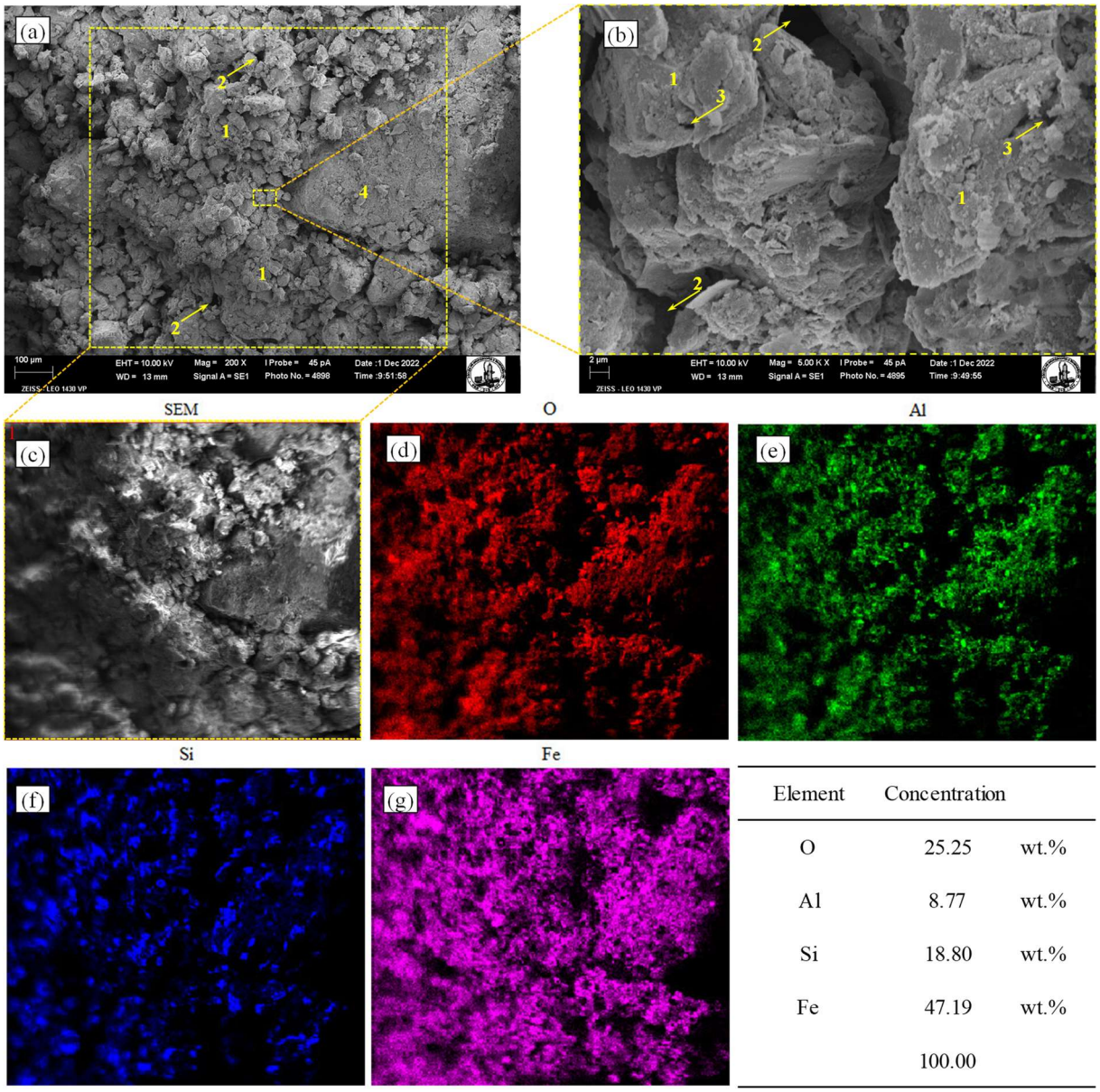

Element	Concentration	
O	25.25	wt.%
Al	8.77	wt.%
Si	18.80	wt.%
Fe	47.19	wt.%
	100.00	

Fig. 4 SEM/EDS mapping images of sample IOT10 macrostructure (200x magnification) and microstructure (5000x magnification). 1: aggregations of fine particles; 2: macropore; 3: micropore; 4: sand particle

Further confirmation of the distinctive characteristic of IOT samples, characterized by a notable concentration of fine particles forming aggregations of considerably larger sizes, becomes apparent when contrasting the particle size curves of the IOT samples with and without dispersant agent, which is shown in Fig. 1. The clay and silt sized particles found for IOT10-WD, IOT13-WD, and IOT16-WD are agglomerated to form larger particles in the coarse silt size range when the dispersant agent is absent (IOT10-WOD, IOT13-WOD, IOT16-WOD).

Overall, the results of the previous data suggests that the decrease in the size of the particles of the finer fraction of the IOT samples with the increase in compaction energy is primarily caused by the destruction of particle aggregations, rather than particle breakage. This

interpretation is reinforced by the absence of significant alterations in the sand content in addition to the consistent pattern of increased clay content and reduced silt content with increasing compaction energy. Notably, the absence of significant particle breakage aligns with the observations made by Carneiro et al. (2023) and Wagner et al. (2023) in their studies on IOT samples from the Quadrilátero Ferrífero region, specifically considering the typical load conditions encountered during dry stack construction. The effects of soil compaction on the structure of IOT samples will be further discussed later. Table 5 shows the mean concentration (in weight %) of the main chemical elements found in the IOT samples, as determined by EDS elemental analysis of four samples from each IOT sample.

Table 5 Mean concentrations of the main chemical elements in the IOT samples

Element	IOT10			IOT13			IOT16		
	Mean (wt.%)	SD	95% CI	Mean (wt.%)	SD	95% CI	Mean (wt.%)	SD	95% CI
O	31.88	2.91	(28.93; 34.83)	30.34	2.12	(27.39; 33.29)	30.40	2.73	(27.45; 33.35)
Al	7.54	0.49	(6.79; 8.27)	8.85	0.90	(8.10; 9.59)	6.53	0.50	(5.79; 7.27)
Si	18.57	1.51	(16.978; 20.16)	16.34	1.68	(14.75; 17.93)	13.12	0.92	(11.53; 14.71)
Fe	42.02	4.77	(37.66; 46.39)	44.48	3.90	(40.11; 48.84)	49.96	2.60	(45.59; 54.32)

SD is standard deviation and 95% CI means 95% confidence interval for mean

ANOVA, at a 95% confidence level, was conducted to evaluate the effect of the IOT sample type on the concentration of the main chemical elements. Results showed that no statistically significant difference was found in the mean concentration of O of different IOT samples [$F(2, 9) = 0.45$, $p = 0.65$] (see Table 5). However, the analysis revealed a significant difference in the statistical understanding between the mean concentrations of Al, Si, and Fe [$F(2, 9) = 12.55$, $p = 0.002$, $F(2, 9) = 15.18$, $p = 0.001$, $F(2, 9) = 4.43$, $p = 0.046$, respectively)].

The results of Tukey's HSD tests for multiple comparisons revealed that sample IOT13 had a higher mean concentration of Al than samples IOT10 and IOT16 [$p = 0.046$, 95% CI = (0.02, 2.61), $p = 0.002$, 95% CI = (-3.61, -1.02), respectively]. No difference in the mean concentration of Al was found between IOT10 and IOT16 ($p = 0.14$). For Si, no difference was observed between IOT10 and IOT13 ($p = 0.12$), but both had higher mean concentrations of Si than sample IOT16 [$p = 0.001$, 95% CI = (-8.23, -2.67), $p = 0.025$, 95% CI = (-6.00, -0.44), respectively]. Regarding Fe, sample IOT16 had a higher mean concentration of Fe than sample IOT10 [$p = 0.042$, 95% CI = (0.31, 15.56)], however, no significant differences were found in the mean concentrations of Fe between the pair-wise samples IOT16-IOT13 ($p = 0.17$) and IOT13-IOT10 ($p = 0.67$).

The similarities in G_s value of the IOT samples, as indicated in Table 2, are attributed to their similar mineralogical composition. Considering that the IOT samples are mainly composed of quartz and hematite, the higher concentration of Fe and the smaller concentration of Si in sample IOT16 explain why it has the greatest value of G_s among all IOT samples (G_s = 3.36). This is also reflected in the lower and intermediate G_s values of IOT10 (3.21) and IOT13 (3.33), respectively. This is consistent with the mean value of 3.71 (with standard deviation of 0.58) for various tailings from Quadrilátero Ferrífero (Carneiro et al. 2023).

2.2 Specimen Preparation

For each IOT sample (IOT10, IOT13, and IOT16), the filter paper method to determine water retention characteristics and hydraulic conductivity tests were conducted on specimens reconstituted with void ratios corresponding to the 75%, 85%, and 100% degrees of compaction achieved in their respective standard Proctor compaction tests (Fig. 2 and Table 4). The choice of 75% and 85% degrees of compaction was made to simulate conditions where the material might not have attained its desired density, primarily because of construction-related factors, notably in areas with high rates of precipitation.

The molding water content of all specimens derived from the same IOT sample was kept constant, equal to the optimum water content determined from the corresponding Standard Proctor compaction curves (Fig. 2 and Table 4). Table 6 presents the reconstitution parameters of the IOT specimens.

Table 6 Reconstitution parameters of the IOT specimens

		Reconstitution parameter	
Sample	Specimen	Void ratio	Water content (%)
IOT10	IOT10-75	0.96	11.71
	IOT10-85	0.73	11.71
	IOT10-100	0.47	11.71
IOT13	IOT13-75	1.10	14.23
	IOT13-85	0.85	14.23
	IOT13-100	0.58	14.23
IOT16	IOT16-75	1.30	16.83
	IOT16-85	1.03	16.83
	IOT16-100	0.72	16.83

Tests with filter paper were conducted on specimens of approximately 50 mm in diameter and 20 mm in height, which were statically compacted in a metal ring with a single layer. Hydraulic conductivity tests, meanwhile, were performed on specimens with a diameter of 50

mm and a height of 100 mm, which were statically compacted in a cylindrical mold with five layers.

2.3 Filter Paper Method

The filter paper method was applied to measure the matric suction of three representative IOT samples (IOT10, IOT13, and IOT16). Three water retention curves were obtained for each IOT sample, corresponding to the void ratios show in Table 6. Approximately 15 specimens were used for each curve to attain a consistent distribution of measurements over a broad range of matric suction values.

After the saturation of the IOT specimens by capillary action (Fig. 5a), they were air-dried to the desired condition as determined by gravimetric difference. For every specimen, three filter paper disks [Whatman No. 42 filter paper, as described in ASTM D5298-16 (2016)] of approximately the same size as the specimen's diameter were used. The first disk was placed in direct contact with the IOT specimens (Fig. 5b), while the second disk, of slightly smaller diameter, was placed over it to measure matric suction (Fig. 5c). The first disk was added to protect the intermediate disk from particle impregnation. The third disk was then placed over the intermediate disk to protect it from contact with other materials (Fig. 5d). The difference in size of the intermediate disk helps to separate it from the other two at the end of the equilibrium phase.

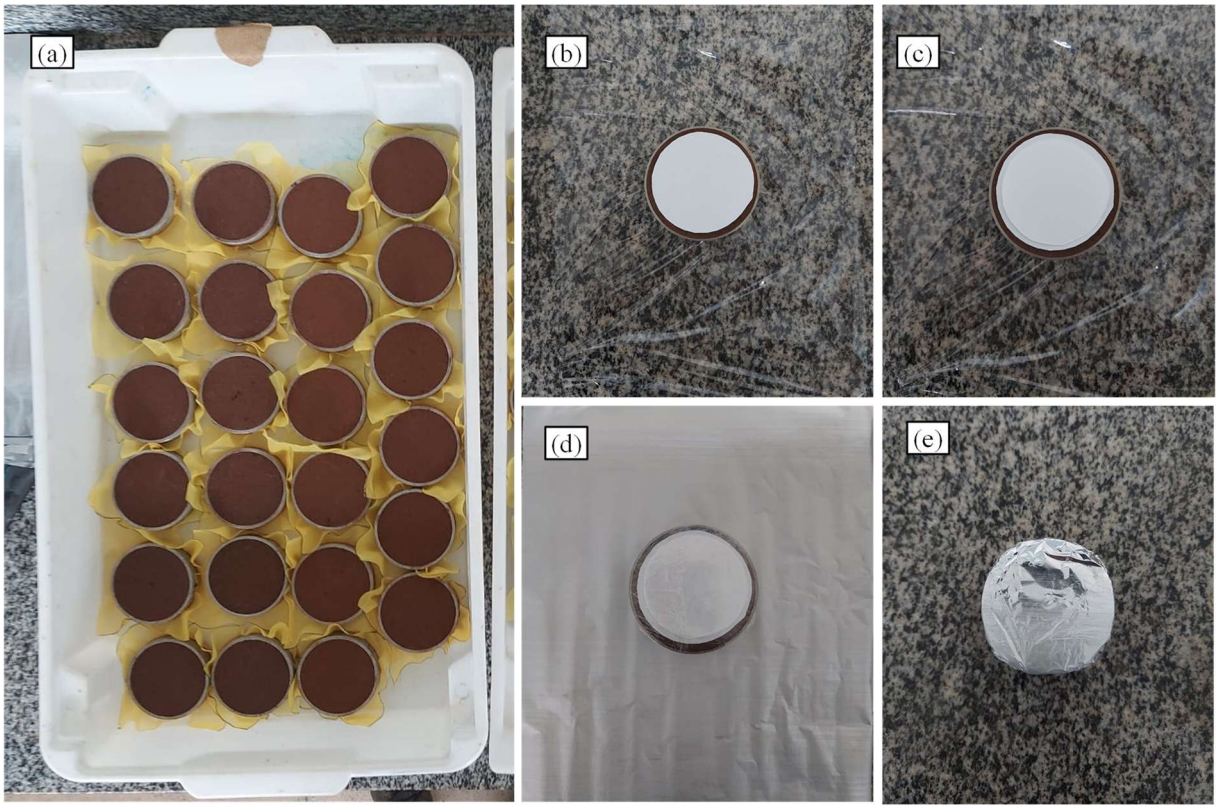

Fig. 5 Filter paper test method. **a** saturation by capillary action; **b** initial filter paper disk; **c** intermediate filter paper disk; **d** final filter paper disk and specimen enclosed in PVC plastic film; **e** specimen wrapped in aluminum foil

After that, the specimens were wrapped in PVC plastic film (Fig. 5d) and aluminum foil (Fig. 5e), then placed in a temperature-controlled box for 14 days to ensure the water content stabilization between the IOT specimens and the filter paper disks. Almeida et al. (2015) reported that, in this situation, the filter paper and porous material have different water contents, but are both subject to the same matric suction. After a 14-day period, the intermediate filter paper disk was carefully removed and weighed with a high-precision scale. The entire process was completed within 3 to 5 s in order to minimize any changes in the filter paper water content.

The matric suction was then calculated from the filter paper water content (w_{FP}) using the relationship described by Chandler et al. (1992). Matric suction (u_a–u_w) can be obtained using Equation 1 for water contents of 47% or less and Equation 2 for water contents greater than 47%.

$$u_a - u_w = 10^{(4{,}84 - 0{,}0622 \cdot w_{FP})} \quad (1)$$

$$u_a - u_w = 10^{(6{,}05 - 2{,}48 \cdot log(w_{FP}))} \quad (2)$$

The approach used to describe the IOT retention characteristics is the multimodal model, according to Durner (1994), which is constructed by a linear superposition of subcurves of the

van Genuchten type (van Genuchten 1980) weighted by a factor w_i. The van Genuchten equation has been employed to fit water retention curves for various mine tailings (Menezes et al. 2015; Gorakhki and Bareither 2017; Bella 2021; Ghandashtani et al. 2021; Oldecop and Rodari 2021; Cao et al. 2021). Therefore, the effective saturation can be described by the following equation:

$$S_e = \sum_{i=1}^{k} w_i \left[\frac{1}{1 + (\alpha_i \cdot (u_a - u_w))^{n_i}}\right]^{1-1/n_i} \quad (3)$$

where w_i are weighting factors for the subcurves, subject to $0 < w_i < 1$ and $\sum w_i = 1$; α_i and n_i are empirical shape parameters, subject to the conditions $\alpha_i > 0$ and $n_i > 1$.

The water retention function written in θ (u_a–u_w) functional form is as follows:

$$\theta = \theta_r + (\theta_s - \theta_r) \cdot S_e \quad (4)$$

where θ is the volumetric water content; θ_s and θ_r are the saturated and residual volumetric water content, respectively.

2.4 Hydraulic Conductivity Tests

Hydraulic conductivity tests were conducted using a triaxial chamber (flexible wall permeameter) on initially saturated specimens with a Skempton B-value of over 95%, following the procedures outlined in ASTM D5084-16a (2016) for constant head tests. The hydraulic gradient varied between 5 and 25, depending on the compaction of the specimens, ranging from very loose (75% degree of compaction) to very dense (100% degree of compaction).

For each representative IOT sample, hydraulic conductivity tests were performed on three specimens with different initial void ratios, as listed in Table 6. Hydraulic conductivity was determined after saturation and again after isotropic consolidation of the specimens under the confining stresses of 100 kPa, 200 kPa, 400 kPa, and 800 kPa. This resulted in a total of 15 measurements for each IOT sample, accounting for a broad range of void ratios.

These measurements, accounting for the inherent variability in IOT samples and variations in void ratios, are of critical importance in unraveling the percolation behavior of tailings materials within stacked disposal systems. They provide valuable insights into the impact of factors such as particle size distribution, void ratio, and mineralogy on percolation, even when these changes are subtle. Furthermore, these measurements play a pivotal role in refining models that adeptly capture the hydraulic behavior of the IOT samples.

3. RESULTS AND DISCUSSION

3.1 Water Retention Curves

The experimental data of the water retention curves (Fig. 6) was best fitted using bimodal functions (k = 2 in Equation 3), with the fitting parameters shown in Table 7. All IOT samples yielded a θ_r value of 0, or very close to it, when undergoing parameter estimation. To ensure consistency with all fittings, θ_r was set to 0 for all IOT samples, as was also done by Zhang et al. (2022) when analyzing dual porosity soils. Additionally, the saturated volumetric water content (θ_s) was assumed to be equal to the total porosity (n_t), as the measurements of the drying water retention curves were conducted on initially saturated specimens.

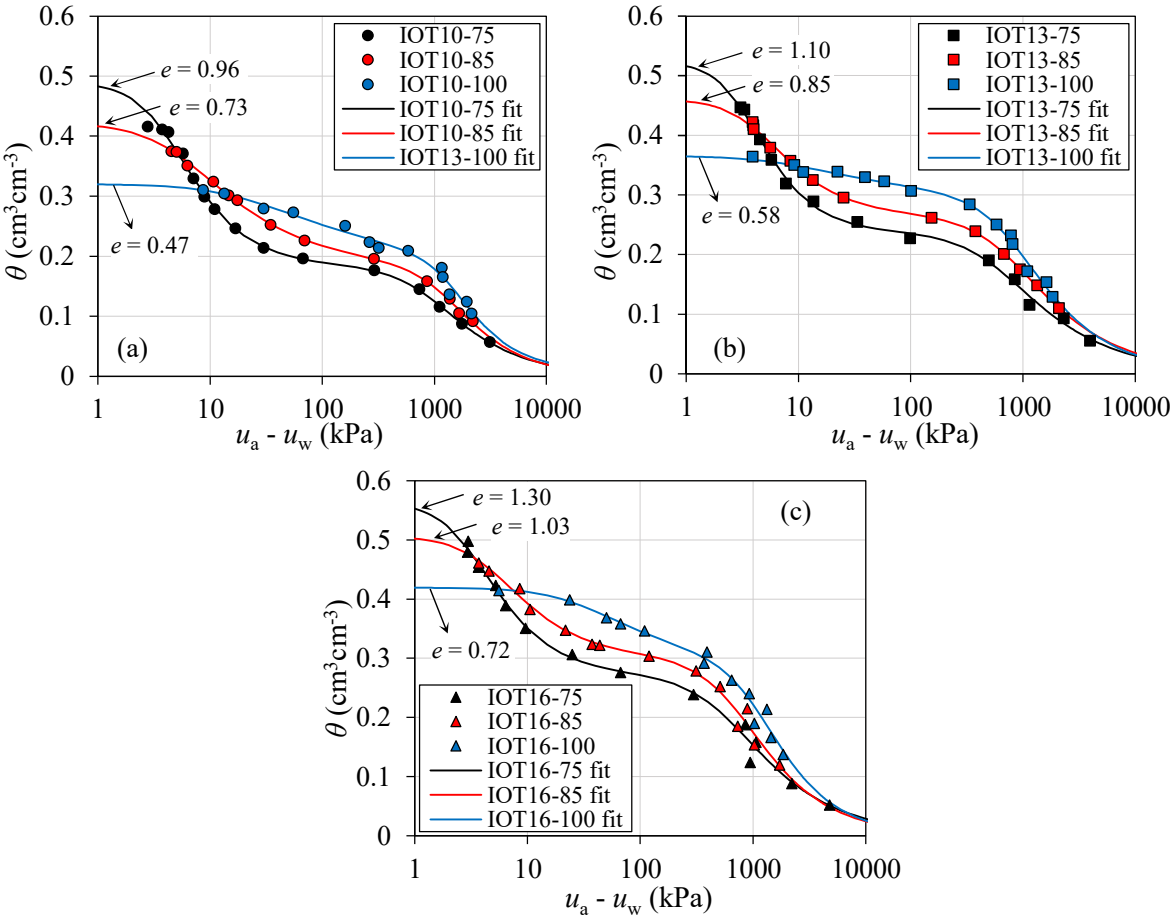

Fig. 6 Measured and fitted water retention curves for IOT samples. **a** IOT10; **b** IOT13; **c** IOT16

Bimodal water retention curves are commonly found for gap-graded soils (Zhang and Chen 2005; Li et al. 2014; Zhao and Zhang 2014; Satyanaga and Rahardjo 2019), compacted clayey soils (Sivakumar and Wheeler 2000; Li and Zhang 2009; Romero 2013; Alonso et al. 2013), and natural structured soils (Miguel and Bonder 2012; Otalvaro et al. 2016; Cordão Neto

et al. 2018; Oliveira et al. 2022). These soils have distinct structural features and properties, and were formed under different conditions; however, they all share two distinct pore types in their soil structure. On the other hand, most water retention curves observed for mine tailings are unimodal (Qiu and Sego 2001; Menezes et al. 2015; Gorakhki and Bareither 2017; Amoah et al. 2018; Liao et al. 2019; Bella 2021; Ghandashtani et al. 2021; Cao et al. 2021; Sepúlveda et al. 2022), although evidence of multimodal behavior has been identified by Zhang et al. (2019), Schafer and Beier (2020) and Oldecop and Rodari (2021).

The bimodal shape of the water retention curves shown in Fig. 6 can be attributed to two different pore-size distributions present in the IOT samples. The first is macroscopic porosity, which is associated with the pore water stored in the larger, intergranular pores between the sand particles and the particle aggregations (macropores). The second is microscopic porosity, which is connected to the pore water trapped within the smaller, intra-aggregate pores (micropores). This dual pore-size distribution is the result of particle aggregation in the IOT samples (Fig. 4).

Furthermore, the shapes of the water retention curve for the IOT samples in Fig. 6 display a gradual shift from bimodal to weakly bimodal curves as the compaction energy increases, from very loose (IOT10-75, IOT13-75, IOT16-75) to dense specimens (IOT10-100, IOT13-100, IOT16-100). This can be attributed to the reduction of the weighting factor w_1 (that describes the contribution of the macropores to the total porosity) and the parameter n_1, which defines the slope of the line connecting macropore water content and matric suction, as seen in Table 7. Additionally, the reduction of void ratio led to a decrease in the parameter controlling the inflexion point in the macropore region (α_1), which in turn caused an increase in macropore air entry values (AEV_1).

Table 7 Fitting parameters of the water retention curves

IOT	e	θ_s (cm^3cm^{-3})	Macrostructure				Microstructure			R^2
			w_1	α_1 (kPa^{-1})	n_1	AEV_1 (kPa)	α_2 (kPa^{-1})	n_2	AEV_2 (kPa)	
IOT10-75	0.96	0.49	0.63	0.23	2.14	4.27	0.0011	1.90	888.3	0.996
IOT10-85	0.73	0.42	0.57	0.18	1.63	5.51	0.0008	2.11	1258.1	0.999
IOT10-100	0.47	0.32	0.45	0.05	1.38	20.64	0.0007	2.47	1493.6	0.985
IOT13-75	1.10	0.52	0.55	0.28	2.35	3.51	0.0017	1.72	588.1	0.997
IOT13-85	0.85	0.46	0.43	0.21	2.08	4.67	0.0014	1.77	734.5	0.999
IOT13-100	0.58	0.37	0.20	0.13	1.46	7.93	0.0012	1.92	809.3	0.993
IOT16-75	1.30	0.56	0.52	0.31	2.12	3.27	0.0017	1.78	573.8	0.993
IOT16-85	1.03	0.51	0.41	0.20	1.97	4.93	0.0015	1.94	683.7	0.987
IOT16-100	0.72	0.42	0.31	0.03	1.63	30.64	0.0009	2.15	1078.6	0.979

All of these changes in the macrostructure parameters of the water retention curve are caused by the reduction of macroporosity, which is the result of decreasing the void ratio. SEM images at 200x magnification of IOT10 (Fig. **7**), IOT13 (Fig. 8) and IOT16 (Fig. 9) illustrate the closure of macropores due to the decrease of void ratio.

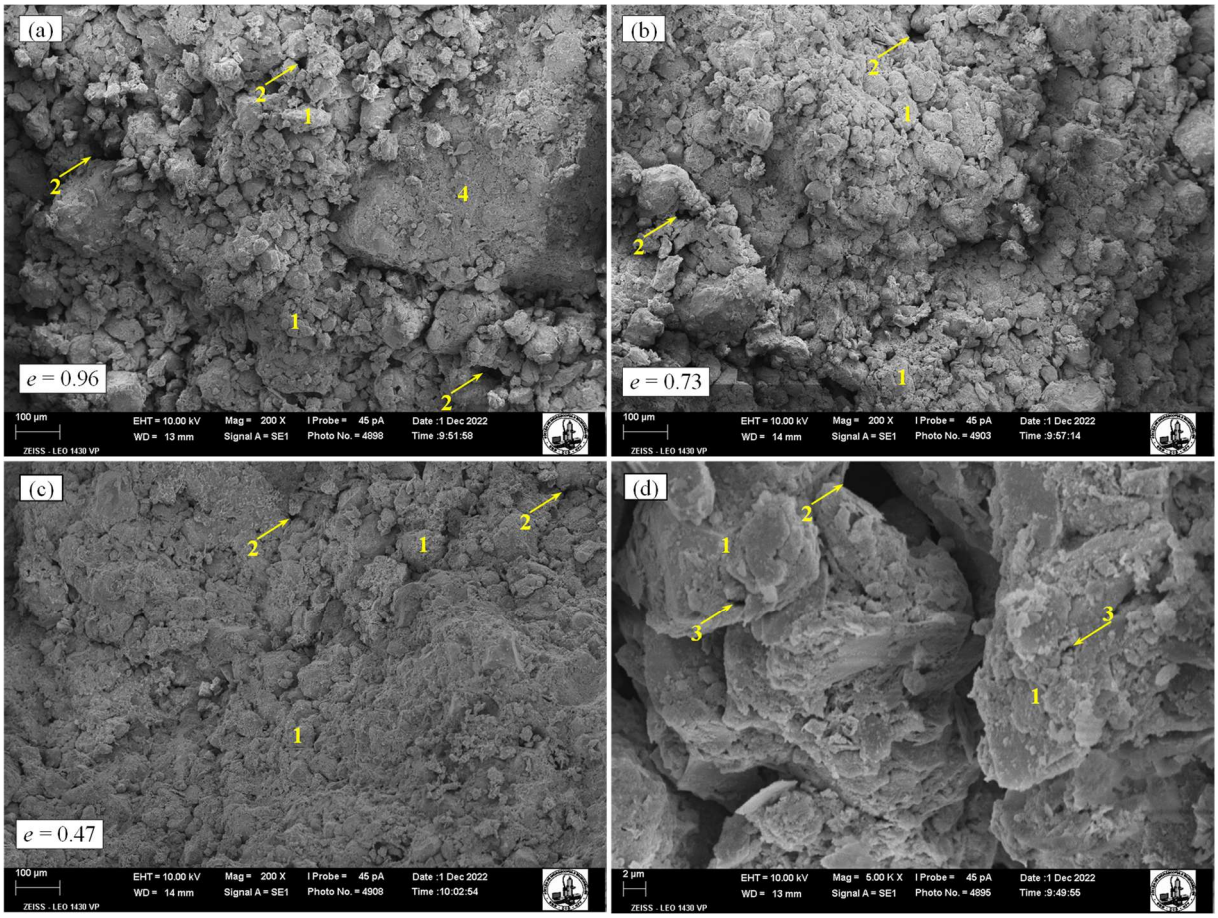

Fig. 7 SEM images of IOT10 structure. **a** IOT10-75 (200x magnification); **b** IOT10-85 (200x magnification); **c** IOT10-100 (200x magnification); **d** IOT10 microstructure (5000x magnification). 1: aggregations of fine particles; 2: macropore; 3: micropore; 4: sand particle

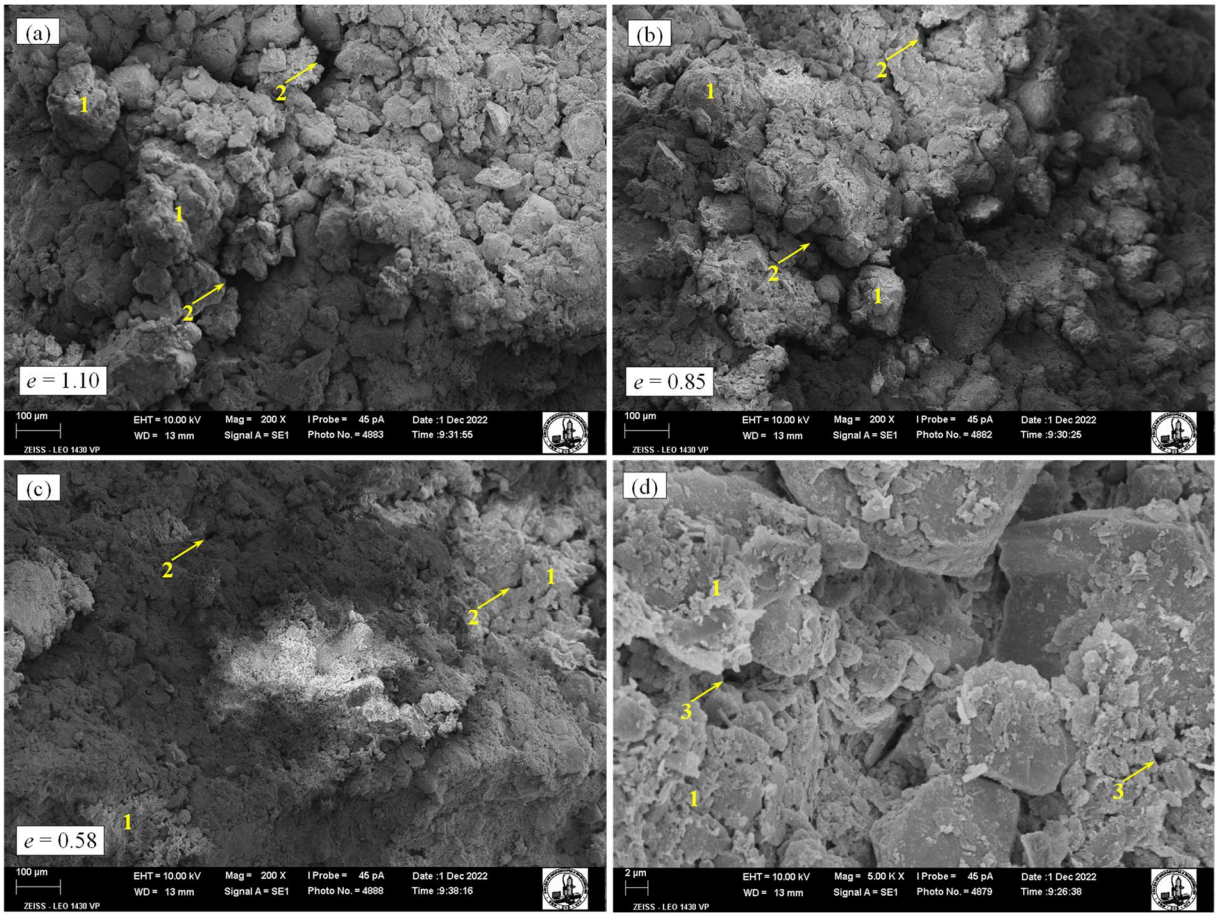

Fig. 8 SEM images of IOT13 structure. **a** IOT13-75 (200x magnification); **b** IOT13-85 (200x magnification); **c** IOT13-100 (200x magnification); **d** IOT13 microstructure (5000x magnification). 1: aggregations of fine particles; 2: macropore; 3: micropore

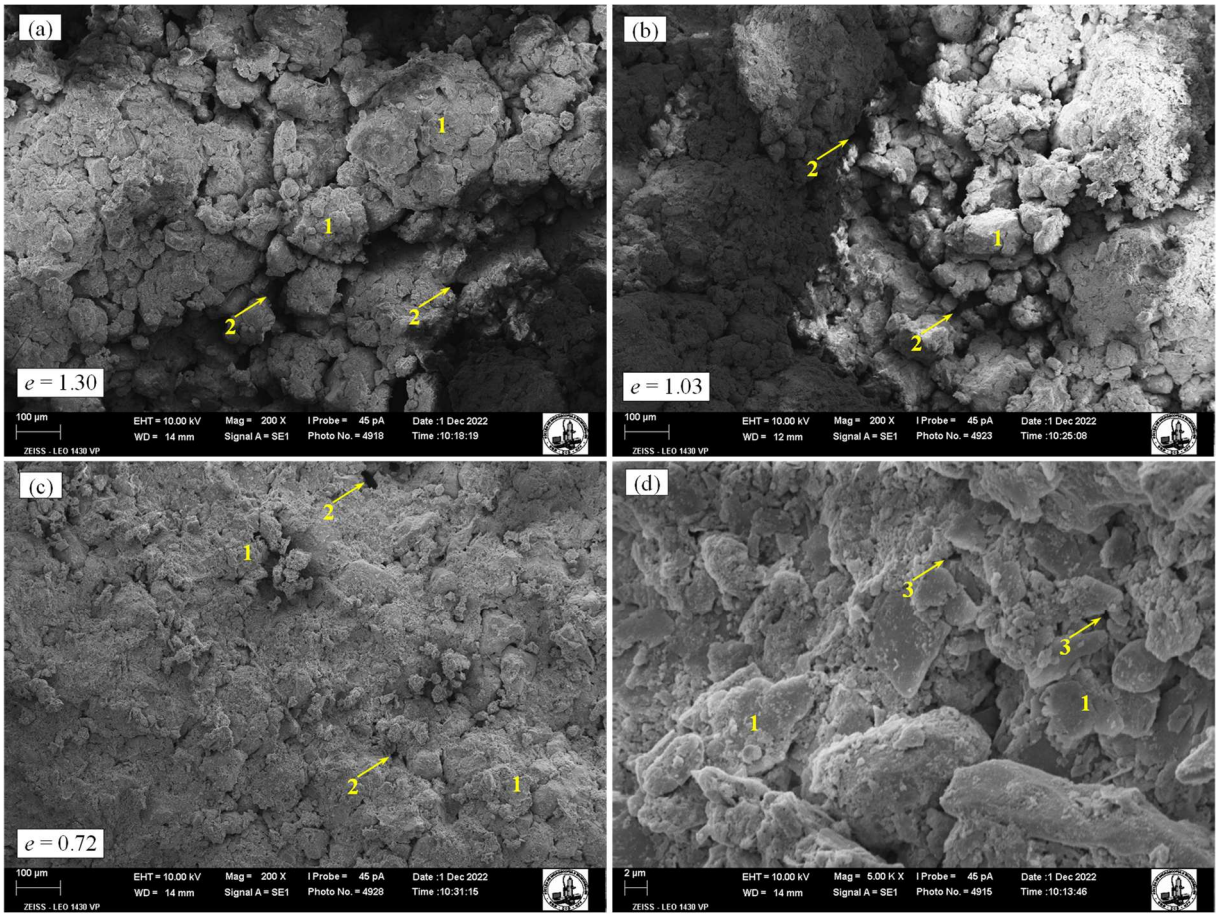

Fig. 9 SEM images of IOT16 structure. **a** IOT16-75 (200x magnification); **b** IOT16-85 (200x magnification); **c** IOT16-100 (200x magnification); **d** IOT16 microstructure (5000x magnification). 1: aggregations of fine particles; 2: macropore; 3: micropore

The very loose IOT specimens (IOT10-75, IOT13-75, and IOT16-75) displayed a high frequency of larger macropores between particles and aggregations, as shown in Fig. **7**a, Fig. 8a, and Fig. 9a. However, as the void ratio decreased with higher energy of compaction, the sizes and frequency of macropores decreased, as seen in Fig. **7**b, Fig. 8b, and Fig. 9b (IOT10-85, IOT13-85, and IOT16-85). Finally, most macropores and the pathways connecting them were eliminated in denser specimens (IOT10-100, IOT13-100, and IOT16-100), with only small macropores remaining, as shown in Fig. **7**c, Fig. 8c, and Fig. 9c. It is important to recognize that with further increases in energy of compaction, or any factor which can cause the void ratio to reduce, such as compression, the macropore volume will be completely erased, and the total porosity of the IOT samples will consist solely of micropores.

The decrease in void ratio was observed to have a direct effect on the microstructure, resulting in an increase in the micropore volume of the IOT samples. The reduction of the weighting factor w_1 also implies an increase of the micropore volume. This was accompanied by a rise in the air entry values (AEV_2), which is associated with the reduction of the parameter

that controls the inflection point in the micropore region (α_2), and the increase of the parameter controlling the slope of the water retention curve in the micropore region (n_2), as seen in Table 7. This suggests that the reduction in void ratio not only decreases the size of micropores, but also decreases the range of sizes in which they are distributed. This pattern was observed for all IOT samples.

In the macrostructure, the decrease of the void ratio resulted in a reduction of the slope of the water retention curve; in the microstructure, however, this slope increases, suggesting the presence of micropores of more uniform sizes. In Fig. **7**d, Fig. 8d, and Fig. 9d, the microstructure of IOT10, IOT13, and IOT16 can be seen, respectively, wherein the aggregation and micropores can be observed. The water retention curves of the IOT samples in Fig. 6 appear to be converging in the micropore region, suggesting that the interval of variability of micropore sizes is quite limited. This cannot be captured by SEM images at high magnification, which only observe a very small section of the samples. To gain better insight into the micropore size distribution, mercury intrusion porosimetry (MIP) should have been used instead.

Based on the previous points, the values of the fitting parameters for all IOT samples are shown in Table 8 as a function of void ratio. A strong linear relationship between all parameters and the void ratio was found for the range of void ratios tested. Using the equations presented in Table 8 combined with Equations 3 and 4, the modelling of the water retention curves can be completed. The final equations corresponding to IOT10, IOT13 and IOT16 are Equations 23, 24, and 25, respectively.

Table 8 Water retention curve fitting parameters as a function of void ratio

IOT	Regression equation	R^2	
IOT 10	$\theta_s = 0.35 \cdot e + 0.16$	0.993	(5)
	$w_1 = 0.36 \cdot e + 0.29$	0.962	(6)
	$\alpha_1 = 0.38 \cdot e - 0.12$	0.955	(7)
	$n_1 = 1.52 \cdot e + 0.62$	0.950	(8)
	$\alpha_2 = 0.0009 \cdot e + 0.0002$	0.920	(9)
	$n_2 = -1.15 \cdot e + 2.99$	0.985	(10)
IOT 13	$\theta_s = 0.30 \cdot e + 0.19$	0.993	(11)
	$w_1 = 0.67 \cdot e - 0.18$	0.981	(12)
	$\alpha_1 = 0.30 \cdot e - 0.05$	0.999	(13)
	$n_1 = 1.71 \cdot e + 0.52$	0.967	(14)
	$\alpha_2 = 0.0009 \cdot e + 0.0007$	0.917	(15)
	$n_2 = -0.37 \cdot e + 2.12$	0.942	(16)
IOT 16	$\theta_s = 0.25 \cdot e + 0.24$	0.993	(17)
	$w_1 = 0.36 \cdot e + 0.05$	0.993	(18)
	$\alpha_1 = 0.48 \cdot e - 0.30$	0.988	(19)
	$n_1 = 0.84 \cdot e + 1.05$	0.962	(20)
	$\alpha_2 = 0.0014 \cdot e - 0.0001$	0.979	(21)
	$n_2 = -0.63 \cdot e + 2.60$	0.997	(22)

$$\theta = (0.35e + 0.16)\left\{(0.36e + 0.29)\left[\frac{1}{1 + ((0.38e - 0.12)(u_a - u_w))^{1.52e+0.62}}\right]^{\frac{1.52e-0.38}{1.52e+0.62}} + (-0.36e + 0.71)\left[\frac{1}{1 + ((0.0009e + 0.0002)(u_a - u_w))^{-1.15e+2.99}}\right]^{\frac{-1.15e+1.99}{-1.15e+2.99}}\right\} \quad (23)$$

$$\theta = (0.30e + 0.19)\left\{(0.67e - 0.18)\left[\frac{1}{1 + ((0.30e - 0.05)(u_a - u_w))^{1.71e+0.52}}\right]^{\frac{1.71e-0.48}{1.71e+0.52}} + (-0.67e + 1.18)\left[\frac{1}{1 + ((0.0009e + 0.0007)(u_a - u_w))^{-0.37e+2.12}}\right]^{\frac{-0.37e+1.12}{-0.37e+2.12}}\right\} \quad (24)$$

$$\theta = (0.25e + 0.24)\left\{(0.36e + 0.05)\left[\frac{1}{1 + ((0.48e - 0.30)(u_a - u_w))^{0.84e+1.05}}\right]^{\frac{0.84e-0.05}{0.84e+1.05}} + (-0.36e + 0.95)\left[\frac{1}{1 + ((0.0014e - 0.0001)(u_a - u_w))^{-0.63e+2.60}}\right]^{\frac{-0.63e+1.60}{-0.63e+2.60}}\right\} \quad (25)$$

In order to guarantee that $\alpha_i > 0$, $n_i > 1$, and $0 < w_1 < 1$, the value of e in Equations 23, 24, and 25 must be between 0.35 and 1.73, 0.28 and 1.75, and 0.64 and 2.52, respectively. However, it is important to note that for very dense IOT samples, with void ratios lower than those tested in the experimental study, unimodal models would better simulate the water-retention characteristics of IOT samples. Fig. 10 presents the predicted curves using the Equations 23, 24, and 25 for the void ratios tested in this study.

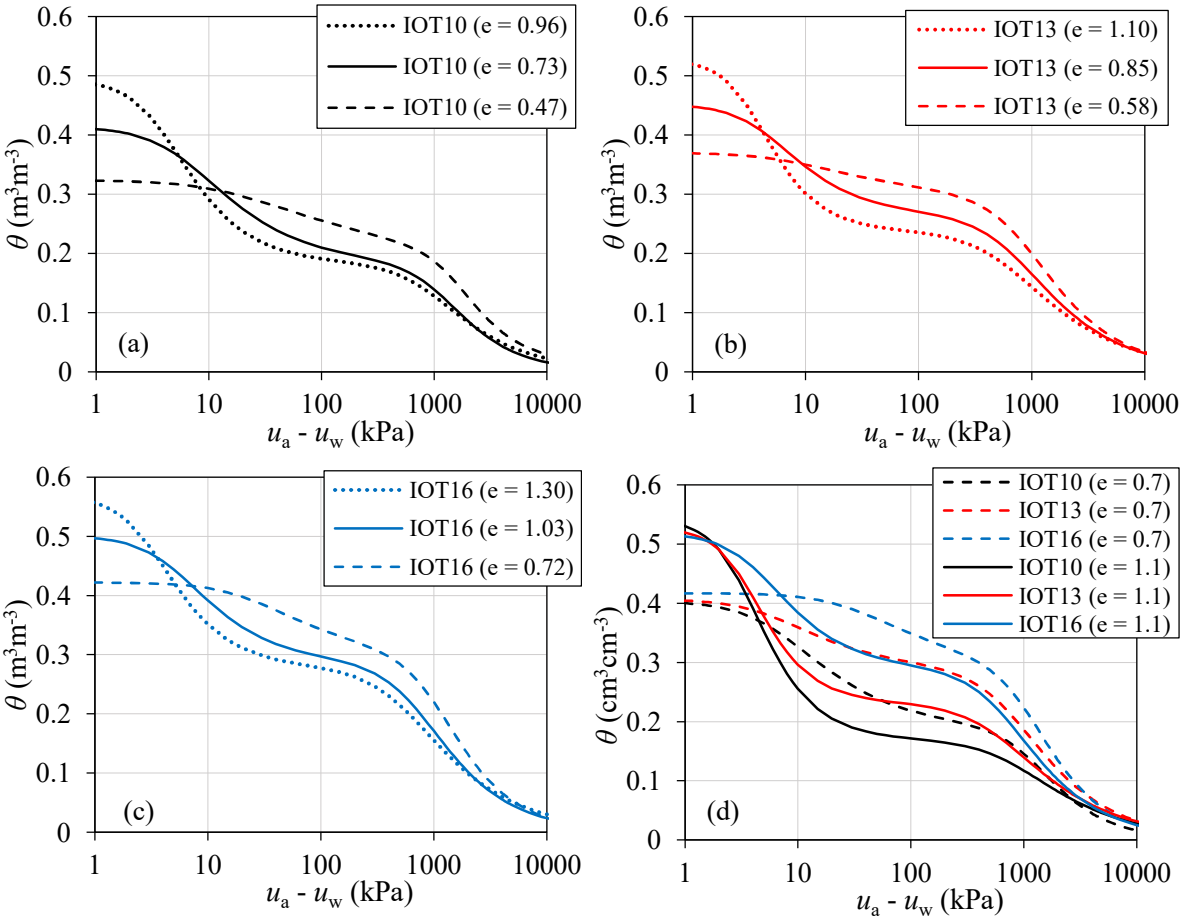

Fig. 10 Predicted water retention curves. **a** IOT10; **b** IOT13; **c** IOT16; **d** influence of particle size

When comparing the curves in Fig. 10a, Fig. 10b, and Fig. 10c with those in Fig. 6, it is evident that the curves closely resemble each other, indicating successful fits. Thus, the influence of the particle size of the IOT samples on the water retention curve and on the pore size distribution can be observed by comparing the predicted curves for void ratios of 0.7 and 1.1, as seen in Fig. 10d.

The increase in clay content of the IOT samples is reflected in the upward shift of the water retention curves for almost the entire matric suction range shown in Fig. 10d, for both void ratios. The shift of the curves is attributed to the increase in porosity corresponding to the micropores with the increase in clay content. Since smaller particle sizes are expected to result in smaller pore sizes, this observation is consistent with the predictions shown in Fig. 10.

Given the small differences in the mineralogy of IOT samples and the previous considerations, it is clear that the particle size distribution of fines, especially the clay content, governs the water-retention characteristics of the IOT samples. The differences in the pore size distribution, resulting from small variations in clay content, remain prominent across a wide

range of voids ratios. This indicates that IOT10, IOT13, and IOT16 are distinct from one another.

3.2 Hydraulic Conductivity

Fig. 11 illustrates the correlation between void ratio and the saturated hydraulic conductivity (k) of samples IOT10, IOT13, and IOT16. Fig. 12 demonstrates how the void ratio of this samples evolves with changing confining stress, in accordance with the reconstitution parameters provided in Table 6. Fig. 12 serves as a supplementary illustration, depicting the stress levels to which the samples were subjected for specific void ratios observed in Fig. 11.

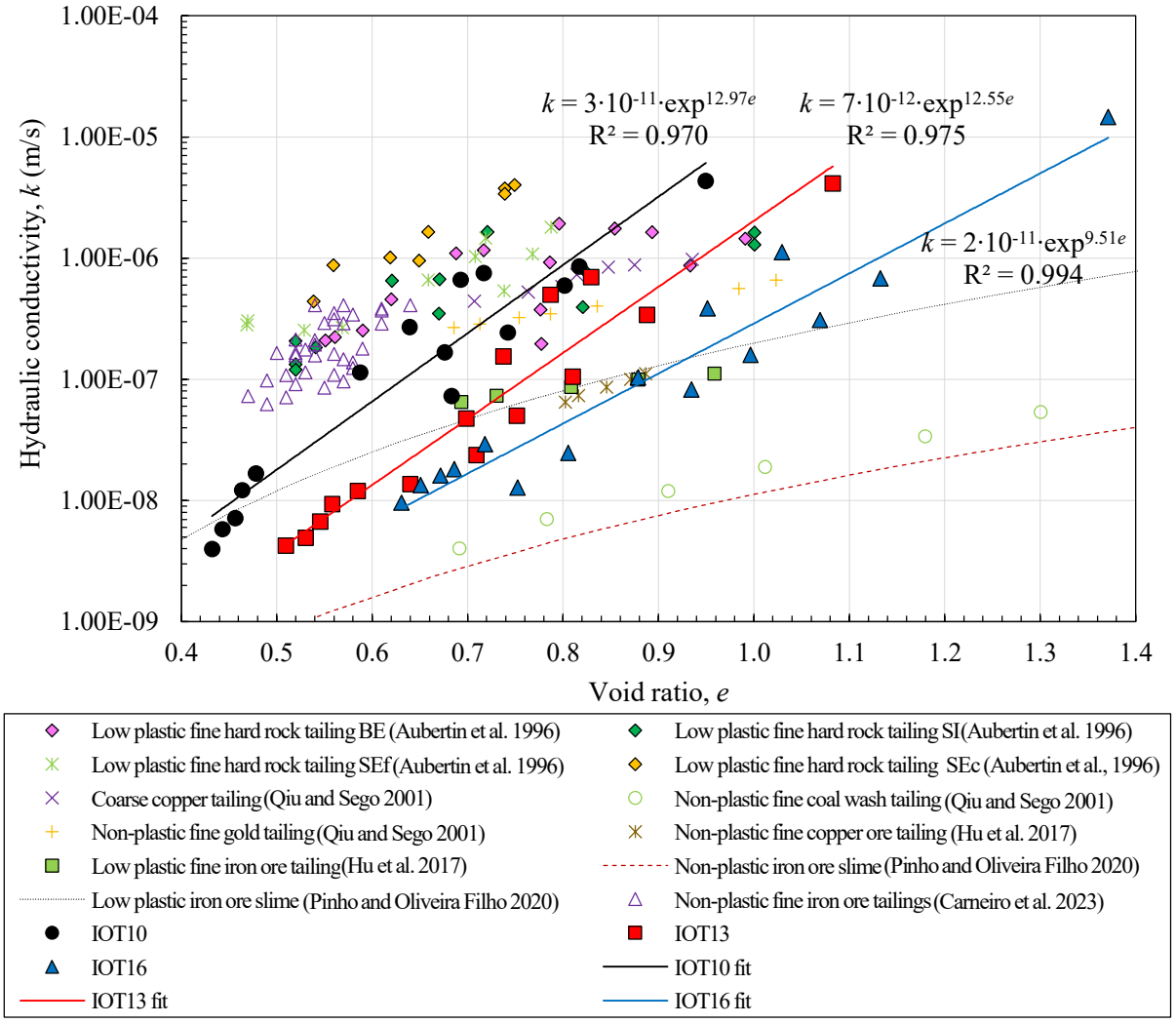

Fig. 11 Relationship between hydraulic conductivity and void ratio of mine tailings

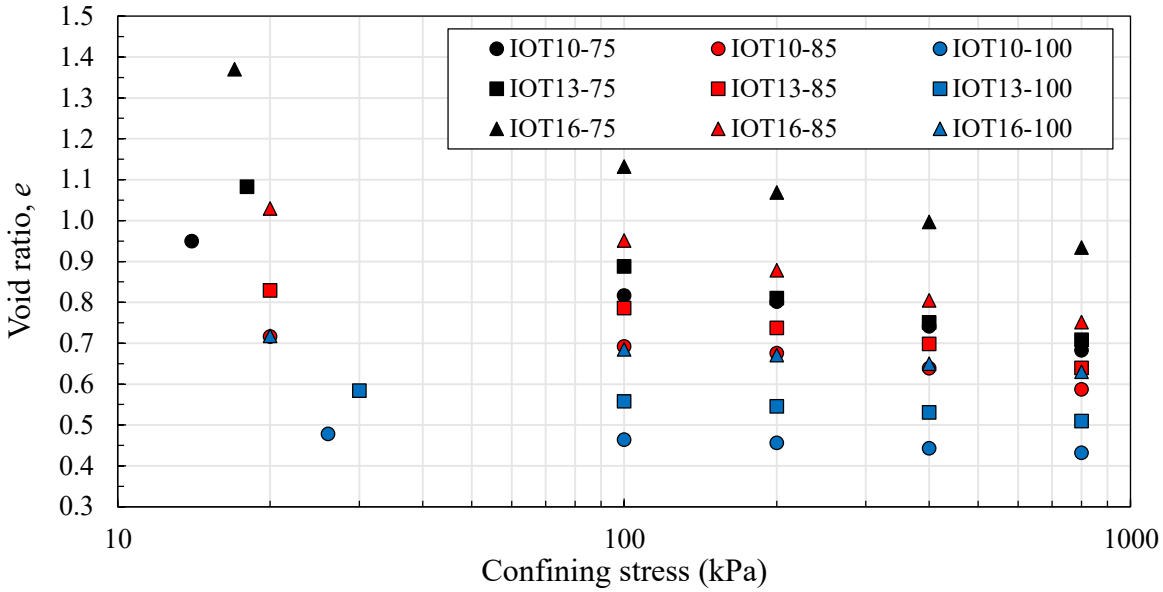

Fig. 12 Void ratio evolution under confining stress for samples IOT10, IOT13, IOT16

In addition to data generated from samples IOT10, IOT13, and IOT16, Fig. 11 combines information from various types of mine tailings found in the literature (Aubertin et al. 1996; Qiu and Sego 2001; Hu et al. 2017; Pinho and Oliveira Filho 2020; Carneiro et al. 2023). The values of k for IOT10, IOT13, and IOT16 were observed to mostly fall within the typical range for silt-sized mine tailings ($1 \cdot 10^{-6}$ to $1 \cdot 10^{-8}$ m/s). This is consistent with the range of $1.7 \cdot 10^{-8}$ to $2.5 \cdot 10^{-5}$ m/s, with an average k of $6.3 \cdot 10^{-7}$ m/s, reported by Robertson et al. (2019) for iron ore tailings from the Quadrilátero Ferrífero.

The hydraulic conductivity of the IOT samples tested in this study decreased by a factor of approximately 1000 as the void ratio (e) decreased, from 1.10^{-5} to 1.10^{-8} m/s for sample IOT16 and from 1.10^{-6} to around 1.10^{-9} m/s for samples IOT10 and IOT13 (as seen in Fig. 11). This trend was accurately described by an exponential function, as expressed by the following equation:

$$k = A \cdot exp^{B \cdot e} \tag{26}$$

where k represents hydraulic conductivity, e is the void ratio, and A, B are fitting parameters. Here, A is the amplitude, and B controls the sensitivity of hydraulic conductivity to changes in void ratio, influencing the steepness of the exponential function.

However, despite the decrease in void ratio, the differences between the k values of the IOT samples remained. As the void ratio changed within the tested range in Fig. 11, sample

IOT16 had the lowest hydraulic conductivity, followed by sample IOT13, and then IOT10. This can be attributed to variations in the pore size distribution among the IOT samples. These variations are caused by differences in their distributions of fine particles, and persist even when the void ratio is changed. This also confirms the distinctive water retention characteristics of these materials, shown in Fig. 6, even when porosity is mainly constituted of micropores.

The trend of increasing hydraulic conductivity with increasing particle size can be seen by comparing the iron ore tailings/slime data in Fig. 11. The lowest values of k were found to correspond to the low plastic and non-plastic iron ore slimes, which contained around 100% and 90% fine content (<75μm) respectively (Pinho and Oliveira Filho 2020). Intermediate values of k (central region of Fig. 11) corresponded to the low-plastic, well-graded silt-sized tailings, composed of the IOT samples investigated in this study and the one studied by Hu et al. (2017). The highest values of k correspond to the non-plastic, poorly graded silt-sized tailing investigated by Carneiro et al. (2023). Thus, the pattern of k values supports the expected increase in hydraulic conductivity with increasing particle size.

Upon explicit recognition that the hydraulic properties of each IOT sample depend on the void ratio, incorporating both water retention properties and saturated hydraulic conductivity, it becomes practical to model a transient saturated-unsaturated seepage problem that considers the variability of the materials and the void ratio along the height of dry stacking tailings deposits. The permeability function and water storage function required for this seepage analysis can be estimated from water retention curves and saturated hydraulic conductivity data, following the examples provided by Thieu et al. (2001). Equations 23, 24, and 25, along with the Equations depicted in Fig. 11, respectively, can be used for this purpose.

4. CONCLUSION

This study examined the hydraulic characteristics of IOT samples intended for staking, focusing on the effect of void ratio and sample variability on the water retention characteristics and hydraulic conductivity. The distinctive geotechnical and hydraulic properties of the studied iron ore tailings stem from their dual porosity structure, resulting from the aggregation of fine particles into larger formations. This particular microstructure, coupled with bimodal water retention curves and the sensitivity of hydraulic conductivity to small variations, sets iron ore tailings apart from typical mine tailings and some other silt soils. Accurate understanding

necessitates specialized modeling approaches, emphasizing their exceptional characteristics in water retention and flow dynamics. Key points discussed in the manuscript include:

(1) IOT samples are low plastic, well-graded silt-sized tailings with very similar physical properties and mineralogy, primarily composed of hematite and quartz. However, this study demonstrates that even slight variations in particle size distribution, particularly clay content, can significantly affect the hydraulic behavior of IOT samples.

(2) All IOT samples have a common distinguishing feature of a high concentration of fine particles forming aggregations of much larger sizes. A typical conceptual model of dual porosity materials, taking into account the pores left between and within these aggregations, was proposed and verified by the experimental results.

(3) A strong linear relationship between void ratio and both macrostructure and microstructure fitting parameters were found by successfully modelling water retention experimental data using bimodal functions. Interestingly, a simultaneous reduction of α_2 and an increase of n_2 were both observed for all IOT samples as the microstructure evolved with the decrease of void ratio.

(4) The hydraulic conductivity of IOT samples is largely determined by the water movement within the macropores, and its value is highly affected by the void ratio and particle size distribution. An exponential function displays how the reduction of void ratio leads to a decrease in hydraulic conductivity. Furthermore, literature has supported the expected increase in hydraulic conductivity with increasing particle size.

(5) The differences in water retention curves and hydraulic conductivity of the IOT samples remains prominent, regardless of their void ratios. This suggests that IOT samples cannot be treated as a single material and should instead be modeled using separate sets of constitutive parameters.

This study has shown that iron ore tailings possess distinctive geotechnical and hydraulic properties, offering practical applications for the design and assessment of stacked tailings. The outcomes contribute in the following ways:

(1) Enhanced Understanding: The research provides a comprehensive characterization of the geotechnical and hydraulic properties of iron ore tailings, improving the understanding of their behavior and the factors that influence these properties.

(2) Dual Porosity Model: The incorporation of a dual porosity model, accounting for the aggregation of fine particles, ensures a more accurate representation of the hydraulic behavior of the tailings. This model takes into account water storage and flow within both macropores and micropores, providing a more comprehensive understanding of the tailings disposal system.

(3) Void Ratio and Hydraulic Properties Relationship: The study establishes a direct link between void ratio and hydraulic properties, enabling the development of more precise percolation models accounting for the variability of void ratio along stacked tailings disposal systems.

(4) The hydraulic conductivity's sensitivity to water movement within macropores, highly influenced by small changes in void ratio and particle size distribution (particularly in clay content) is an important input for percolation analysis on stacked tailings as this can improve the quality of this analysis, so providing a more reliable comprehension of water flow within the stack and its effects on slope stability and on design of drainage systems.

The insights and methodologies outlined in this paper have the potential to be applied to other tailings materials, establishing a groundwork for future research and practical applications. This framework provides the basis for conducting a comprehensive transient saturated-unsaturated seepage analysis, taking into consideration the varying characteristics of the tailings and their multiple post-compacted conditions in stacked tailings. This saturated-unsaturated seepage is an issue that should be better understand for a proper characterization of percolation through tailings, and this information should be considered on the improvement of design of stacked tailings and their drainage systems.

REFERENCES

ABNT NBR 7182-16 (2016) Compaction test. Brazilian Association of Technical Standards, Rio de Janeiro (in Portuguese)

Almeida EL, Teixeira AS, Silva Filho FC et al (2015) Filter paper method for the determination of the soil water retention curve. Rev Bras Ciência do Solo 39:1344–1352. https://doi.org/10.1590/01000683rbcs20140546

Alonso EE, Pinyol NM, Gens A (2013) Compacted soil behaviour: initial state, structure and constitutive modelling. Géotechnique 63:463–478. https://doi.org/10.1680/geot.11.P.134

Amoah N, Dressel W, Fourie A (2018) Characterization of unsaturated geotechnical

properties of filtered magnetite tailings in a dry stack facility. In: Jewel RJ, Fourie AB (eds) Paste 2018, Australian Centre for Geomechanics, Perth, pp 375–388. https://doi.org/10.36487/ACG_rep/1805_31_Amoah

Araujo GLS, Moreno JAS, Zornberg JG (2021) Shear behavior of mixtures involving tropical soils and tire shreds. Constr Build Mater. https://doi.org/10.1016/j.conbuildmat.2020.122061

ASTM D4220/D4220M-14 (2014) Standard practices for preserving and transporting soil samples. American Society for Testing and Material, West Conshohocken

ASTM D4318-17e1 (2018) Standard test methods for liquid limit, plastic limit, and plasticity index of soils. American Society for Testing and Material, West Conshohocken

ASTM D5084-16a (2016) Standard test methods for measurement of hydraulic conductivity of saturated porous materials using a flexible wall permeameter. American Society for Testing and Material, West Conshohocken

ASTM D5298-16 (2016) Standard test method for measurement of soil potential (suction) using filter paper. American Society for Testing and Material, West Conshohocken

ASTM D7928-17 (2021) Standard test method for particle-size distribution (gradation) of fine-grained soils using the sedimentation (hydrometer) analysis. American Society for Testing and Material, West Conshohocken

ASTM D854-23 (2023) Standard test methods for specific gravity of soil solids by the water displacement method. American Society for Testing and Material, West Conshohocken

Aubertin M, Bussiere B, Chapuis RP (1996) Hydraulic conductivity of homogenized tailings from hard rock mines. Can Geotech J 33:470–482. https://doi.org/10.1139/t96-068

Barati S, Tabatabaie SP, Samani N, Asadi S (2020) Stabilization of iron ore tailings with cement and bentonite: a case study on Golgohar mine. Bull Eng Geol Environ 79:4151–4166. https://doi.org/10.1007/s10064-020-01843-6

Bella G (2021) Water retention behaviour of tailings in unsaturated conditions. Geomech Eng 26:117–132. https://doi.org/doi.org/10.12989/gae.2021.26.2.117

Cacciuttolo C, Pérez GC (2022) Practical experience of filtered tailings technology in chile and peru: an environmentally friendly solution. Minerals. https://doi.org/10.3390/min12070889

Cacciuttolo C, Valenzuela F (2022) Efficient use of water in tailings management: new technologies and environmental strategies for the future of mining. Water. https://doi.org/10.3390/w14111741

Cao B, Tian Y, Gui R, Liu Y (2021) Experimental study on the effect of key factors on the soil–water characteristic curves of fine-grained tailings. Front Environ Sci. https://doi.org/10.3389/fenvs.2021.710986

Carneiro JJV, Marques EAG, Viana da Fonseca AJP et al (2023) Characterization of an iron ore tailing sample and the evaluation of its representativeness. Geotech Geol Eng 41:2833–2852. https://doi.org/10.1007/s10706-023-02430-8

Chandler RJ, Crilly MS, Smith M et al (1992) A low-cost method of assessing clay desiccation for low-rise buildings. In: Institution of civil engineers, Civil engineering, pp 82–89. https://doi.org/10.1680/icien.1992.18771

Consoli NC, Vogt JC, Silva JPS et al (2022) Behaviour of compacted filtered iron ore tailings–portland cement blends: new brazilian trend for tailings disposal by stacking. Appl Sci. https://doi.org/10.3390/app12020836

Cordão Neto MP, Hernández O, Lorenzo RR et al (2018) Study of the relationship between hydro-mechanical soil behavior and microstructure of a structured soil. Earth Sci Res J 22:91–101. https://doi.org/10.15446/esrj.v22n2.65640

Crystal C, Hore C, Ezama I (2018) Filter-pressed dry stacking: design considerations based on practical experience. In: Tailings and mine waste 2018, UBC Studios, University of British Columbia, Keystone, pp 209–219

Dash M, Dwari RK, Biswal SK et al (2011) Studies on the effect of flocculant adsorption on the dewatering of iron ore tailings. Chem Eng J 173:318–325. https://doi.org/10.1016/j.cej.2011.07.034

Dauce PD, Castro GB, Lima MMF, Lima RMF (2019) Characterisation and magnetic

concentration of an iron ore tailings. J Mater Res Technol 8:1052–1059. https://doi.org/10.1016/j.jmrt.2018.07.015

Davies M (2011) Filtered dry stacked tailings: the fundamentals. In: Tailings and mine waste, University of British Columbia Library, Vancouver

Deng D, Cao G, Zhang Y (2021) Experimental study on the fine iron ore tailing containing gypsum as backfill material. Adv Mater Sci Eng 2021:1–9. https://doi.org/10.1155/2021/5576768

Durner W (1994) Hydraulic conductivity estimation for soils with heterogeneous pore structure. Water Resour Res 30:211–223. https://doi.org/10.1029/93WR02676

Ferreira IC, Galéry R, Henriques AB et al (2022) Reuse of iron ore tailings for production of metakaolin-based geopolymers. J Mater Res Technol 18:4194–4200. https://doi.org/10.1016/j.jmrt.2022.03.192

Fredlund DG, Rahardjo H, Fredlund MD (2012) Unsaturated soil mechanics in engineering practice. John Wiley & Sons, Inc., Hoboken, NJ, USA

Freitas VAA, Breder SM, Silvas FPC et al (2019) Use of iron ore tailing from tailing dam as catalyst in a fenton-like process for methylene blue oxidation in continuous flow mode. Chemosphere 219:328–334. https://doi.org/10.1016/j.chemosphere.2018.12.052

Furnell E, Bilaniuk K, Goldbaum M et al (2022) Dewatered and stacked mine tailings: a review. ACS ES&T Eng 2:728–745. https://doi.org/10.1021/acsestengg.1c00480

Gao HY, Xu ZM, Ren Z et al (2021) Laterite as a potential seepage barrier from a karst-depression tailings impoundment. Clays Clay Miner 69:1–22. https://doi.org/10.1007/s42860-020-00103-8

Ghandashtani MB, Edraki M, Costine A, Baumgartl T (2021) Investigation of geotechnical, hydromechanical, and chemical behaviour of polymer-treated tailings. In: Fourie AB, Reid D (eds) Paste 2021, Australian Centre for Geomechanics, Perth, pp 79–90. https://doi.org/10.36487/ACG_repo/2115_08

Giri SK, Das NN, Pradhan GC (2011) Magnetite powder and kaolinite derived from waste iron ore tailings for environmental applications. Powder Technol 214:513–518.

https://doi.org/10.1016/j.powtec.2011.09.017

Gomes RB, Tomi G, Assis PS (2016) Iron ore tailings dry stacking in Pau Branco mine, Brazil. J Mater Res Technol 5:339–344. https://doi.org/10.1016/j.jmrt.2016.03.008

Gorakhki M, Bareither C (2017) Sustainable reuse of mine tailings and waste rock as water-balance covers. Minerals. https://doi.org/10.3390/min7070128

Guedes JPC, Silvani C, Carvalho JVA et al (2024) Mechanical behaviour of fibre-reinforced cemented iron ore tailings across the compaction curve. Geotech Geol Eng. https://doi.org/10.1007/s10706-023-02736-7

Hu L, Wu H, Zhang L et al (2017) Geotechnical properties of mine tailings. J Mater Civ Eng. https://doi.org/10.1061/(ASCE)MT.1943-5533.0001736

Jeong SW (2014) The effect of grain size on the viscosity and yield stress of fine-grained sediments. J Mt Sci 11:31–40. https://doi.org/10.1007/s11629-013-2661-1

Ke X, Chen J, Shan Y (2019) A new failure criterion for determining the cyclic resistance of low-plasticity fine-grained tailings. Eng Geol. https://doi.org/10.1016/j.enggeo.2019.105273

Krishna RS, Quezada GR, Sahu JK, Sadangi JK (2021) Rheological characterization and performance of flocculants in iron ore tailings management. Mater Today Proc 43:2888–2894. https://doi.org/10.1016/j.matpr.2021.01.128

Li W, Coop MR (2019) Mechanical behaviour of Panzhihua iron tailings. Can Geotech J 56:420–435. https://doi.org/10.1139/cgj-2018-0032

Li X, Li JH, Zhang LM (2014) Predicting bimodal soil–water characteristic curves and permeability functions using physically based parameters. Comput Geotech 57:85–96. https://doi.org/10.1016/j.compgeo.2014.01.004

Li X, Zhang LM (2009) Characterization of dual-structure pore-size distribution of soil. Can Geotech J 46:129–141. https://doi.org/10.1139/T08-110

Liao S, Mishra PN, Scheuermann A (2019) Some laboratory scale tests on an australian coal tailings sample. Japanese Geotech Soc Spec Publ 7:445–449.

https://doi.org/10.3208/jgssp.v07.071

Lima RE, Lima Picanço J, Silva AF, Acordes FA (2020) An anthropogenic flow type gravitational mass movement: the Córrego do Feijão tailings dam disaster, Brumadinho, Brazil. Landslides 17:2895–2906. https://doi.org/10.1007/s10346-020-01450-2

Liu D, Edraki M, Malekizadeh A et al (2019) Introducing the hydrate gel membrane technology for filtration of mine tailings. Miner Eng 135:1–8. https://doi.org/10.1016/j.mineng.2019.02.030

Marques A, Oliveira S, Paes B, Coelho A (2020) Evaluation of the liquefaction susceptibility of filtered iron ore tailings from the Iron Quadrangle (Brazil). In: Quelopana H (ed) Paste 2020, Gecamin Publications, Santiago. https://doi.org/10.36487/ACG_repo/2052_79

McDonald JED, Roache SC, Kawatra SK (2016) Repurposing mine tailings: Cold bonding of siliceous iron ore tailings. Miner Metall Process 33:47–52. https://doi.org/10.19150/mmp.6467

Mendes BC, Pedroti LG, Bonomo BR et al (2021) Effect of the incorporation of bauxite and iron ore tailings on the properties of clay bricks. In: Li J et al (eds) Characterization of minerals, metals, and materials 2021, Springer, Cham, pp 361–372. https://doi.org/10.1007/978-3-030-65493-1_35

Menezes LP, Oliveira Filho WL, Silva CHC (2015) Determination of the soil water retention curve using the flow pump. Rem Rev Esc Minas 68:207–213. https://doi.org/10.1590/0370-44672015680108

Miguel MG, Bonder BH (2012) Soil–water characteristic curves obtained for a colluvial and lateritic soil profile considering the macro and micro porosity. Geotech Geol Eng 30:1405–1420. https://doi.org/10.1007/s10706-012-9545-y

Mmbando E, Fourie A, Reid D (2023) Mechanics of an iron ore tailings exhibiting transitional behaviour. Geotech Geol Eng. https://doi.org/10.1007/s10706-023-02379-8

Montani JL, Pornillos E, Munoz H (2013) Geotechnical-geochemical and operational considerations for the application of dry stacking tailings deposits – state-of-the-art. In: Jewell R, Fourie A, Caldwell J, Pimenta J (eds) Paste 2013, Australian Centre for

Geomechanics, Perth, pp 249–260

Ng CWW, Akinniyi DB, Zhou C, Chiu CF (2019) Comparisons of weathered lateritic, granitic and volcanic soils: Compressibility and shear strength. Eng Geol 249:235–240. https://doi.org/10.1016/j.enggeo.2018.12.029

Oldecop L, Rodari G (2021) Unsaturated mine tailings disposal. Soil Rocks 44:1–12. https://doi.org/10.28927/SR.2021.067421

Oldecop LA, Rodari GJ, Muñoz JJ (2017) Atmosphere interaction and capillary barrier in filtered tailings. Geotech Geol Eng 35:1803–1817. https://doi.org/10.1007/s10706-017-0210-3

Oliveira A, Pelaquim F, Zanin R et al (2022) The structure of tropical lateritic soils as an impacting factor in the shape of soil-water characteristic curves. Soil Rocks 45:1–13. https://doi.org/10.28927/SR.2022.070521

Oluremi JR, Eberemu AO, Ijimdiya ST, Osinubi KJ (2019) Lateritic soil treated with waste wood ash as liner in landfill construction. Environ Eng Geosci 25:127–139. https://doi.org/10.2113/EEG-2023

Otalvaro IF, Cordão Neto MP, Delage P, Caicedo B (2016) Relationship between soil structure and water retention properties in a residual compacted soil. Eng Geol 205:73–80. https://doi.org/10.1016/j.enggeo.2016.02.016

Pinho MQ, Oliveira Filho WL (2020) Large strain consolidation analyses of fine tailings disposal in mining pits. REM - Int Eng J 73:411–419. https://doi.org/10.1590/0370-44672018730195

Pinto P, Milagre L, Moreira L (2022) Iron recovery from iron ore tailings by direct hydrogen reduction at low temperature and magnetic separation. J Braz Chem Soc. https://doi.org/10.21577/0103-5053.20220053

Pires KS, Mendes JJ, Figueiredo VC (2019) Mineralogical characterization of iron ore tailings from the quadrilatero ferrifero, brazil, by eletronic quantitative mineralogy. Mater Res. https://doi.org/10.1590/1980-5373-mr-2019-0194

Prates C, Lima A, Ferreira I et al (2023) Use of iron ore tailing as raw material for two

products: sodium silicate and geopolymers. J Braz Chem Soc. https://doi.org/10.21577/0103-5053.20220149

Prates CD, Ballotin FC, Limborço H et al (2020) Heterogeneous acid catalyst based on sulfated iron ore tailings for oleic acid esterification. Appl Catal A Gen. https://doi.org/10.1016/j.apcata.2020.117624

Qiu Y (Jason), Sego DC (2001) Laboratory properties of mine tailings. Can Geotech J 38:183–190. https://doi.org/10.1139/t00-082

Reid D, Fanni R, DiDonna P (2022) The effect of tamping conditions on undrained shear strengths of a non-plastic sandy silt tailings. Can Geotech J 59:783–795. https://doi.org/10.1139/cgj-2020-0269

Reid D, Fanni R, Koh K, Orea I (2018) Characterisation of a subaqueously deposited silt iron ore tailings. Géotechnique Lett 8:278–283. https://doi.org/10.1680/jgele.18.00105

Rissoli ALC, Pereira GS, Mendes AJC et al (2023) Dry stacking of filtered iron ore tailings: comparing on-field performance of two drying methods. Geotech Geol Eng. https://doi.org/10.1007/s10706-023-02689-x

Riveros GA, Sadrekarimi A (2021) Static liquefaction behaviour of gold mine tailings. Can Geotech J 58:889–901. https://doi.org/10.1139/cgj-2020-0209

Robertson PK, Melo L, Williams DJ, Wilson GW (2019) Report of the expert panel on the technical causes of the failure of Feijão dam I

Rocha GM, Cruz MVM, Lima NP, Lima RMF (2022) Reverse cationic flotation of iron ore by amide-amine: bench studies. J Mater Res Technol 18:223–230. https://doi.org/10.1016/j.jmrt.2022.02.039

Romero E (2013) A microstructural insight into compacted clayey soils and their hydraulic properties. Eng Geol 165:3–19. https://doi.org/10.1016/j.enggeo.2013.05.024

Sadrekarimi A, Riveros GA (2020) Static liquefaction analysis of the fundão dam failure. Geotech Geol Eng 38:6431–6446. https://doi.org/10.1007/s10706-020-01446-8

Sakthivel R, Das B, Satpati B, Mishra BK (2009) Gold supported iron oxide–hydroxide

derived from iron ore tailings for CO oxidation. Appl Surf Sci 255:6577–6581. https://doi.org/10.1016/j.apsusc.2009.02.079

Santoro L, Putzolu F, Mondillo N et al (2022) Trace element geochemistry of iron-(oxy)-hydroxides in Ni(Co)-laterites: Review, new data and implications for ore forming processes. Ore Geol Rev. https://doi.org/10.1016/j.oregeorev.2021.104501

Santos Junior MP, Gomes RC, Ribeiro SGS, Delgado BG (2022) Evaluation of flow liquefaction susceptibility of a sandy-silt tailings using the CPTu. In: Gottardi G, Tonni L (eds) Cone penetration testing 2022, 1st edn. CRC Press, pp 913–919. https://doi.org/10.1201/9781003308829

Satyanaga A, Rahardjo H (2019) Unsaturated shear strength of soil with bimodal soil-water characteristic curve. Géotechnique 69:828–832. https://doi.org/10.1680/jgeot.17.P.108

Schafer H, Beier N (2020) Estimating soil-water characteristic curve from soil-freezing characteristic curve for mine waste tailings using time domain reflectometry. Can Geotech J 57:73–84. https://doi.org/10.1139/cgj-2018-0145

Sepúlveda RG, Robert ES, Camacho-Tauta J (2022) Assessment of the self-compaction effect in filtered tailings disposal under unsaturated condition. Minerals. https://doi.org/10.3390/min12040422

Silva CB, Paiva PRP (2020) Artificial stone production using iron ore tailing (IOT). Cerâmica 66:164–171. https://doi.org/10.1590/0366-69132020663782854

Sivakumar V, Wheeler SJ (2000) Influence of compaction procedure on the mechanical behaviour of an unsaturated compacted clay. Part 1: Wetting and isotropic compression. Géotechnique 50:359–368. https://doi.org/10.1680/geot.2000.50.4.359

Souza AH de, Krüger FL, Araújo FGS, Mendes JJ (2021) Mineralogical characterization applied to iron ore tailings from the desliming stage with emphasis on quantitative electron microscopy (Qem). Mater Res. https://doi.org/10.1590/1980-5373-mr-2019-0677

Thieu NTM, Fredlund MD, Fredlund DG, Vu HQ (2001) Seepage modelling in a saturated/unsaturated soil system. In: Hai VT, Chau NM (eds) International Conference

on Management of the Land and Water Resources, Hanoi, pp 49–56

Ulrich B (2019) Practical thoughts regarding filtered tailings. In: Paterson A, Fourie A, Reid D (eds) Paste 2019, Australian Centre for Geomechanics, Perth, pp 71–79. https://doi.org/10.36487/ACG_rep/1910_01_Ulrich

Ulrich B, Coffin J (2013) Considerations for tailings facility design and operation using filtered tailings. In: Jewell R, Fourie A, Caldwell J, Pimenta J (eds) Paste 2013, Australian Centre for Geomechanics, Perth, pp 201–210. https://doi.org/10.36487/ACG_rep/1363_15_Ulrich

van Genuchten MT (1980) A closed-form equation for predicting the hydraulic conductivity of unsaturated soils. Soil Sci Soc Am J 44:892–898. https://doi.org/10.2136/sssaj1980.03615995004400050002x

Vanapalli SK, Fredlund DG, Pufahl DE (1999) The influence of soil structure and stress history on the soil–water characteristics of a compacted till. Géotechnique 49:143–159. https://doi.org/10.1680/geot.1999.49.2.143

Wagner AC, Carvalho JVA, Sousa Silva JP et al (2023) Dry stacking of iron ore tailings: possible particle breakage during compaction. In: Geng X (ed) Institution of Civil Engineers, Geotechnical Engineering, pp 1–9. https://doi.org/10.1680/jgeen.22.00216

Yang M, Sun J, Dun C et al (2020) Cementitious activity optimization studies of iron tailings powder as a concrete admixture. Constr Build Mater. https://doi.org/10.1016/j.conbuildmat.2020.120760

Yuan S, Zhang Q, Yin H, Li Y (2021) Efficient iron recovery from iron tailings using advanced suspension reduction technology: A study of reaction kinetics, phase transformation, and structure evolution. J Hazard Mater. https://doi.org/10.1016/j.jhazmat.2020.124067

Yüksek S (2022) Electroosmotic dewatering of iron ore tailings: a laboratory study to improve geotechnical properties. Adv Civ Eng 2022:1–12. https://doi.org/10.1155/2022/7662997

Zhang F, Wilson GW, Fredlund DG (2019) Estimation of permeability function for

bulyanhulu tailings. Geotech Test J. https://doi.org/10.1520/GTJ20170303

Zhang L, Chen Q (2005) Predicting bimodal soil–water characteristic curves. J Geotech Geoenviron Eng 131:666–670. https://doi.org/10.1061/(ASCE)1090-0241(2005)131:5(666)

Zhang Y, Weihermüller L, Toth B et al (2022) Analyzing dual porosity in soil hydraulic properties using soil databases for pedotransfer function development. Vadose Zo J. https://doi.org/10.1002/vzj2.20227

Zhao HF, Zhang LM (2014) Effect of coarse content on shear behavior of unsaturated coarse granular soils. Can Geotech J 51:1371–1383. https://doi.org/10.1139/cgj-2012-0292

CHAPTER 4

NUMERICAL EVALUATION OF HYDRAULIC AND STABILITY RESPONSES IN FILTERED TAILINGS STACKS UNDER VARIABLE CONSTRUCTION CONDITIONS[2]

Abstract The increasing demand for sustainable mining practices has intensified the focus on filtered tailings stacking as a safer and more environmentally responsible alternative for waste management. However, the inherent variability in tailings material properties and environmental conditions poses significant challenges for achieving optimal compaction, which can compromise geotechnical stability if not adequately addressed. This study investigates the influence of unsaturated hydraulic properties on the seepage and mechanical behavior of iron ore tailings (IOT) stacks, focusing on the effects of void ratio variations, material heterogeneity, and undercompaction during construction under alternating weather conditions. The numerical evaluation applies fully coupled seepage–deformation simulations to investigate transient hydraulic responses and slope stability across various construction scenarios. Key findings reveal that lower void ratios, despite material heterogeneity, effectively enhance geotechnical stability by limiting seepage within the tailings stack and allowing matric suction to prevail, particularly along the slope of the stack. In contrast, undercompacted scenarios exhibit rapid saturation, perched water tables, and increased pore pressures, significantly reducing Factors of Safety (FoS), especially during early construction stages. These scenarios are highly sensitive to weather conditions, with rainy periods intensifying saturation and pore pressure buildup. These insights highlight the importance of precise compaction strategies to mitigate risks associated with tailings variability and seasonal rainfall. The proposed framework offers a robust foundation for designing and assessing filtered tailings stacks, enhancing their safety and resilience while addressing the challenges of unsaturated soil mechanics and environmental interactions.

Keywords filtered tailings · numerical modeling · hydraulic behavior · unsaturated soil mechanics · stability analysis

[2] Original paper in *Geotechnical and Geological Engineering*. Accepted on July 21, 2025. First author: Sérgio Leandro Scher Dis Neto. https://doi.org/10.1007/s10706-025-03321-w.

Abbreviations and Symbols

A: Saturated hydraulic conductivity function fitting parameter (m/s)

AEV: Air-entry value (kPa)

B: Saturated hydraulic conductivity function fitting parameter (dimensionless)

c': Effective cohesion intercept (kPa)

c'_p: Effective peak cohesion intercept (kPa)

c'_{res}: Effective residual cohesion intercept (kPa)

CEC: Cation exchange capacity (meq/100 g)

C_C: Coefficient of curvature (dimensionless)

C_U: Coefficient of uniformity (dimensionless)

D_{50}: Average particle size (mm)

e: Void ratio (dimensionless)

E: Elastic modulus (kPa)

ETP_{pot}: Potential evapotranspiration (mm/month)

FoS: Factor of Safety (dimensionless)

G_s: Specific gravity of solids (dimensionless)

IOT: Iron ore tailings

k_s: Saturated hydraulic conductivity (m/s)

$k(u_a - u_w)$: Unsaturated hydraulic conductivity function (m/s)

n: Porosity (dimensionless)

n_1, n_2: Water retention curve fitting parameters (dimensionless)

PI: Plasticity index (%)

QF: Quadrilátero Ferrífero

S_e: Effective saturation (dimensionless)

$u_a - u_w$: Matric suction (kPa)

USCS: Unified Soil Classification System

w: Water content (%)

$w_{L:}$ Liquid limit (%)

w_{opt}: Optimum water content (%)

w_P: Plastic limit (%)

w_1: Weighting factor in bimodal water retention function (dimensionless)

α_1, α_2: Water retention curve fitting parameters (kPa^{-1})

γ: Unit weight (kN/m^3)

γ_d: Dry unit weight (kN/m^3)

$\gamma_{d,max}$: Maximum dry unit weight (kN/m^3)

γ_{sat}: Saturated unit weight (kN/m³)
θ: Volumetric water content (dimensionless)
θ_r: Residual volumetric water content (dimensionless)
θ_s: Saturated volumetric water content (dimensionless)
τ: Shear strength (kPa)
v: Poisson's ratio (dimensionless)
φ': Effective angle of internal friction (degrees)
φ^b: Friction angle related to suction contribution (degrees)
φ'_p: Effective peak angle of internal friction (degrees)
φ'_{res}: Effective residual angle of internal friction (degrees)
$\sigma - u_a$: Net normal stress on the plane of failure at failure (kPa)

1. Introduction

Filtered tailings represent a significant advancement in mining waste management, offering numerous advantages that enhance environmental safety, particularly due to the unsaturated state achieved in the stacked tailings systems (Doi et al. 2023; Guedes et al. 2024a). Dewatering effectively reduces the storage volume and footprint, minimizes the risk of contaminating seepage, and lowers the potential for internal erosion (Cacciuttolo and Pérez 2022; Sako and Pabst 2023). It also allows for the recovery of a substantial portion of the water used in ore beneficiation (Fränkle et al. 2024). Additionally, unsaturated tailings exhibit increased shear strength, reducing their susceptibility to both static and dynamic liquefaction compared to slurried tailings stored in dams (Williams 2021; Servi et al. 2022).

In response to Brazil's new regulations—introduced after the failures at Mariana and Brumadinho, which now prohibit upstream tailings dams and require the decharacterization of existing ones—filtered tailings technology emerges as a viable alternative (Consoli et al. 2024; Guedes et al. 2024b). This method not only complies with the new legal framework but also provides a safer solution for managing both newly generated tailings and those from decharacterized dams (Consoli et al. 2022; Silva et al. 2024). By eliminating surface ponds, promoting unsaturated conditions through effective drainage, and ensuring dilatant conditions throughout the deposits via mechanical compaction, filtered tailings address both regulatory requirements and safety concerns (Farenzena et al. 2024).

However, achieving the desired unsaturated condition for tailings involves significant design and operational challenges, largely due to the variability in water content (Tebechrani Neto et al. 2025). Factors such as grain size distribution and mineral composition can influence

filtration efficiency, while disposal methods—including transportation, discharge, and spreading—directly affect water content (Burden and Wilson 2023; Cacciuttolo and Atencio 2023). Additionally, segregation, water bleeding, drainage, evaporation, and rainfall further impact water content (Oldecop and Rodari 2021). The rate of tailings production affects the frequency of lifts and exposure to atmospheric conditions, while varying lift heights and discharge areas also contribute to fluctuations in water content (Ulrich 2019).

In Brazil, these challenges are compounded by intense rainfall during the wet seasons, which poses additional obstacles to maintaining optimal conditions for filtered tailings compaction (Rissoli et al. 2024). Heavy precipitation often increases the water content of tailings beyond acceptable limits, preventing compaction within specified design parameters (Vargas and Campomanes 2022). While arid climates allow natural drying to be enhanced through methods such as repeated dozing, disking, or ripping, which expose more surface area to evaporation (Ulrich 2019), continuous rainfall in wet climates often renders these techniques ineffective. Under such conditions, tailings can either be temporarily stored in drying areas until their moisture content decreases to acceptable levels—causing operational delays—or placed in the non-structural zones of the dry stack as out-of-specification material, where they are managed with limited or no mechanical compaction (Crystal et al. 2018).

Managing the disposal of filtered tailings in light of these complexities requires precise control of the saturation profile. This involves integrating the net infiltration rate with the hydraulic properties of the tailings, as determined by the water retention curve and unsaturated hydraulic conductivity function (Wilson 2021). Seepage management relies on coupled tailings-atmosphere modeling, considering both hydraulic properties and local microclimatic and atmospheric conditions (Cao et al. 2021; Sepúlveda et al. 2022). This becomes especially important for tailings with distinct structural features, as they exhibit multimodal porosity, which affects water retention and flow behavior (Zhang et al. 2019; Schafer and Beier 2020; Dias Neto et al. 2024).

The hydro-mechanical behavior of unsaturated filtered tailings is highly influenced by factors such as degree of compaction, initial void ratio, and applied stress conditions. Finer-grained tailings tend to retain more moisture and exhibit greater compressibility than coarser flotation tailings, even when subjected to the same compaction energy (Wagner et al. 2024). Laboratory evidence indicates that higher compaction levels combined with slightly wet-of-optimum moisture conditions enhance water retention across a wide range of suction values (Aghazamani et al. 2024). In parallel, denser compaction significantly reduces hydraulic

conductivity, especially in loosely structured tailings, thereby limiting infiltration and suppressing the development of excess pore pressures (Medina et al. 2024; Santos et al. 2024). In addition to compaction strategies, small amounts of cement have also been shown to enhance moisture retention and reduce hydraulic conductivity in unsaturated iron ore tailings (Bruschi et al. 2025).

Mechanically, increased dry density enhances the stiffness and shear strength of filtered tailings, limiting both settlement and deformation under operational loads (Andrade et al. 2025; Chaves et al. 2025). However, under high stress conditions, particle breakage becomes a governing factor—altering the grain structure, increasing compressibility, and reducing the friction angle (Zhang et al. 2020; Consoli et al. 2024). The addition of cementitious agents has proven to mitigate some of these effects, especially in low-density or fine-grained iron ore tailings. Under high confining pressures, artificially cemented tailings exhibited enhanced fabric stability and reduced compressibility, supporting their use in critical zones of dry stacks (Consoli et al. 2025; Zhang et al. 2025).

A further challenge lies in the transition from unsaturated to saturated conditions under both monotonic and cyclic loading. Even with initially low saturation, localized wetting can occur during shearing due to air phase volume collapse (Bella 2021; Wang et al. 2024; Gallardo et al. 2025). This reduction in effective stress may trigger contractive behavior and liquefaction, particularly under rapid loading or infiltration conditions (Sepúlveda et al. 2022; Nayanthara et al. 2024).

Residual matric suction, when preserved, plays a critical stabilizing role in dry stacking systems. Field-scale observations confirm that suction can persist after deposition, contributing to high shear strength and enabling steep slope construction in unsaturated conditions (Amoah et al. 2018). Despite its benefits, suction is highly sensitive to environmental factors, especially rainfall, which can rapidly elevate the degree of saturation, reduce suction, and compromise slope stability—particularly in shallow layers and low-permeability zones where infiltration accumulates (Simms 2021).

These complex hydromechanical interactions, influenced by both environmental conditions and stress history, highlight the need for predictive modeling tools. Recent studies have demonstrated that unsaturated conditions significantly influence pore pressure development, seepage patterns, and slope stability in filtered tailings stacks. For instance, Sanchez et al. (2023) analyzed the seepage behavior during stack construction and found that

coupled hydromechanical models predicted thicker saturated zones compared to uncoupled models, particularly under rainfall or in the absence of protective covers. Similarly, Garcia et al. (2024) highlighted the role of compaction and parameter uncertainty in high-rainfall regions, showing that infiltration variability is most pronounced during early construction phases, especially at the base of the stack, before saturation dominates.

Other studies have explored how operational and geotechnical parameters influence stability under unsaturated conditions. Vizcarra (2021) used coupled numerical modeling to evaluate how stacking rate and foundation permeability affect pore pressure dissipation and safety factors over time. The results showed that higher stacking rates and low-permeability foundations lead to slower pore pressure dissipation, resulting in lower safety factors and increased instability risks during staged construction. Extending this understanding, Gallardo et al. (2024) presented a fully coupled hydromechanical model for copper tailings, identifying a saturation threshold of 65–70% at which failure surfaces begin to form, and revealing that faster stacking rates consistently reduce the factor of safety due to limited drainage and uneven saturation distribution.

While these studies offer valuable insights into the hydromechanical behavior of filtered tailings under unsaturated conditions, they also present limitations that constrain broader applicability. These include the use of one-dimensional models that neglect lateral flow (Sanchez et al. 2023), fixed parameter sets across varying stress and suction conditions (Gallardo et al. 2024), uncertainties in hydraulic function calibration under different compaction levels (Garcia et al. 2024), and the case-specific nature of partially drained simulations (Vizcarra 2021). Such limitations are particularly critical in tropical climates, where alternating wet and dry seasons hinder consistent compaction and suction control. In these settings, the natural variability of IOT (Pires et al. 2019; Carmignano et al. 2021; Laureano et al. 2022; Carneiro et al. 2023) can intensify heterogeneities, leading to perched water tables, restricted drainage, and elevated pore pressures—ultimately compromising slope stability.

To address these challenges, the analysis focused on the geotechnical behavior of IOT during the construction of a filtered tailings stack, with emphasis on three key factors: void ratio variations, material heterogeneity, and undercompaction resulting from reduced efficiency during rainy periods. The numerical modeling combined fully coupled seepage–deformation analyses under transient flow conditions with limit equilibrium methods accounting for the contribution of unsaturated shear strength. By integrating seepage dynamics, pore pressure development, and mechanical performance, the proposed framework supports a comprehensive

understanding of how unsaturated hydraulic properties and construction practices influence the stability of filtered tailings stacks. This approach advances current modeling efforts by applying a 2D coupled model strategy capable of capturing the transient behavior of partially compacted, heterogeneous layers under rainfall-driven infiltration—conditions representative of tropical mining environments and field-scale compaction constraints.

2. Materials and Methods

2.1 Iron Ore Tailings

Dias Neto et al. (2024) conducted a thorough characterization of the geotechnical and hydraulic properties of three representative IOT samples from a mining complex located in the Quadrilátero Ferrífero (QF), Minas Gerais, Brazil. These samples were collected directly from the pressure belt filter before being deposited and subsequently compacted within a tailings stack. The three samples, designated as IOT10, IOT13, and IOT16, were named based on their clay content, which corresponds to 10.0%, 12.8%, and 16.2%, respectively, as depicted in Fig. 1 and detailed in Table 1.

Fig. 1 also presents the particle size distribution curve for an additional IOT sample, referred to as IOTmech, which was analyzed by Carneiro et al. (2023), Venturin (2022), and Oliveira (2021) and originates from the same mining complex previously mentioned. The mechanical properties of IOTmech were employed in the numerical analyses of this study. According to Carneiro et al. (2023), tailings from mines within the QF exhibit similarities due to their common geological formation. This alignment justifies the use of IOTmech's properties as a representative basis for the other tailings studied. Additional geotechnical and chemical properties for all the IOT samples are provided in Table 2.

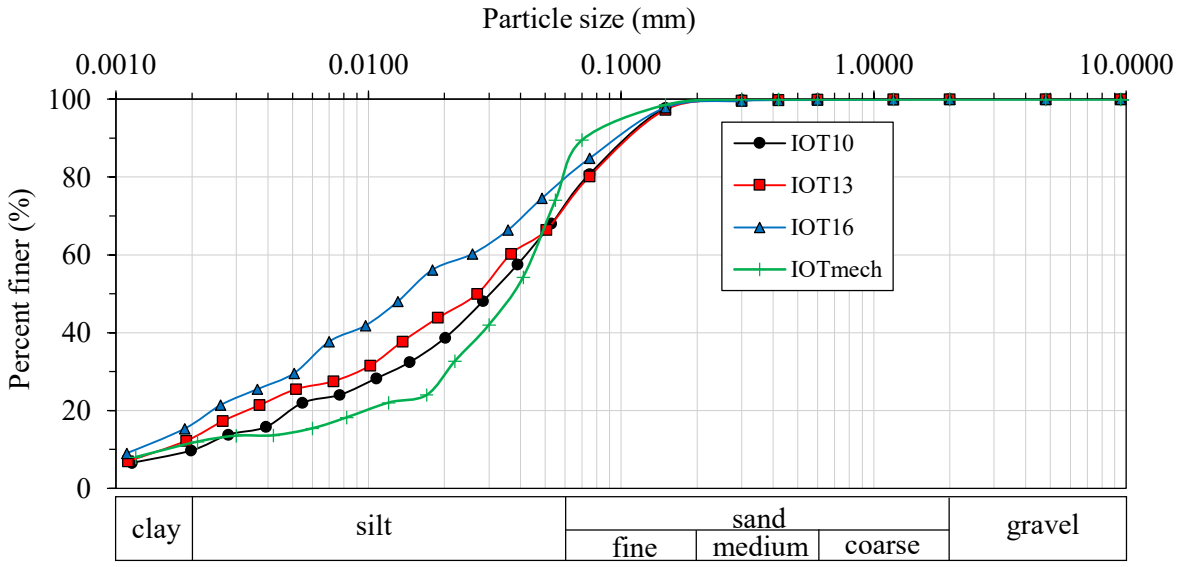

Fig. 1 Particle size distribution curves of the IOT samples

Table 1 Particle size fractions and geotechnical properties inferred from particle size distribution curves

IOT	Clay	Silt	Fine sand	Medium sand	Coarse sand	Gravel	D_{50}	C_U	C_C	Fine content
	< 0.002	0.002 - 0.06	0.06 - 0.2	0.2 - 0.6	0.6 - 2.0	> 2.0				< 0.075 mm
	mm	mm	mm	mm	mm	mm	mm	-	-	%
IOT10	10.0	63.0	27.0	0.0	0.0	0.0	0.029	20.83	1.66	80.7
IOT13	12.8	59.6	27.0	0.6	0.0	0.0	0.026	22.14	1.43	80.2
IOT16	16.2	63.8	19.4	0.6	0.0	0.0	0.014	20.95	0.87	84.9
IOTmech	12.0	67.5	19.9	0.6	0.0	0.0	0.037	28.80	5.60	89.6

D_{50} represents the average particle size. C_U stands for the coefficient of uniformity, while C_C stands for the coefficient of curvature

Table 2 Geotechnical-chemical properties of the IOT samples

	IOT 10	IOT13	IOT16	IOTmech
Liquid limit - w_L (%)	20	23	27	NP
Plastic limit - w_P (%)	14	12	17	NP
Plasticity index - PI (%)	6	11	10	NP
Specific gravity - G_s	3.21	3.33	3.36	3.22
Maximum dry unit weight - $\gamma_{d,max}$ (kN/m³)	21.40	20.73	19.16	21.05
Optimum water content - w_{opt} (%)	11.71	14.23	16.83	11.80
pH distilled water	6.66	6.49	6.37	-
pH KCl solution	6.48	6.27	6.30	-
CEC (meq/100 g)	0.77	0.63	0.86	-
USCS classification	CL-ML	CL	CL	ML

NP represents Non-Plastic; $\gamma_{d,max}$ and w_{opt} are determined using the Standard Proctor compaction test

The samples IOT10, IOT13, and IOT16 are low-plastic, well-graded silt-sized tailings with very similar physical properties and mineralogy. They are primarily composed of hematite

and quartz, with traces of goethite and kaolinite. The presence of these iron and aluminum oxides-hydroxides gives these IOT samples a common characteristic: a high concentration of fine particles that form larger aggregations. This phenomenon results in a dual porosity structure, where water is stored and flows within both macropores and micropores (Dias Neto et al. 2024). IOTmech, while non-plastic, also exhibits a particle size distribution and Standard Proctor compaction properties that are consistent with those of the other IOT samples.

Fig. 2 presents Scanning Electron Microscopy (SEM) images of sample IOT10, which was compacted to a void ratio of 0.96. In Fig. 2a, larger pores (macropores) are visible between particle aggregations. Fig. 2b depicts these macropores along with smaller pores (micropores) within the aggregations. The bimodal shape of the water retention curve shown in Fig. 2c is a result of two distinct pore-size distributions arising from the particle aggregation in sample IOT10.

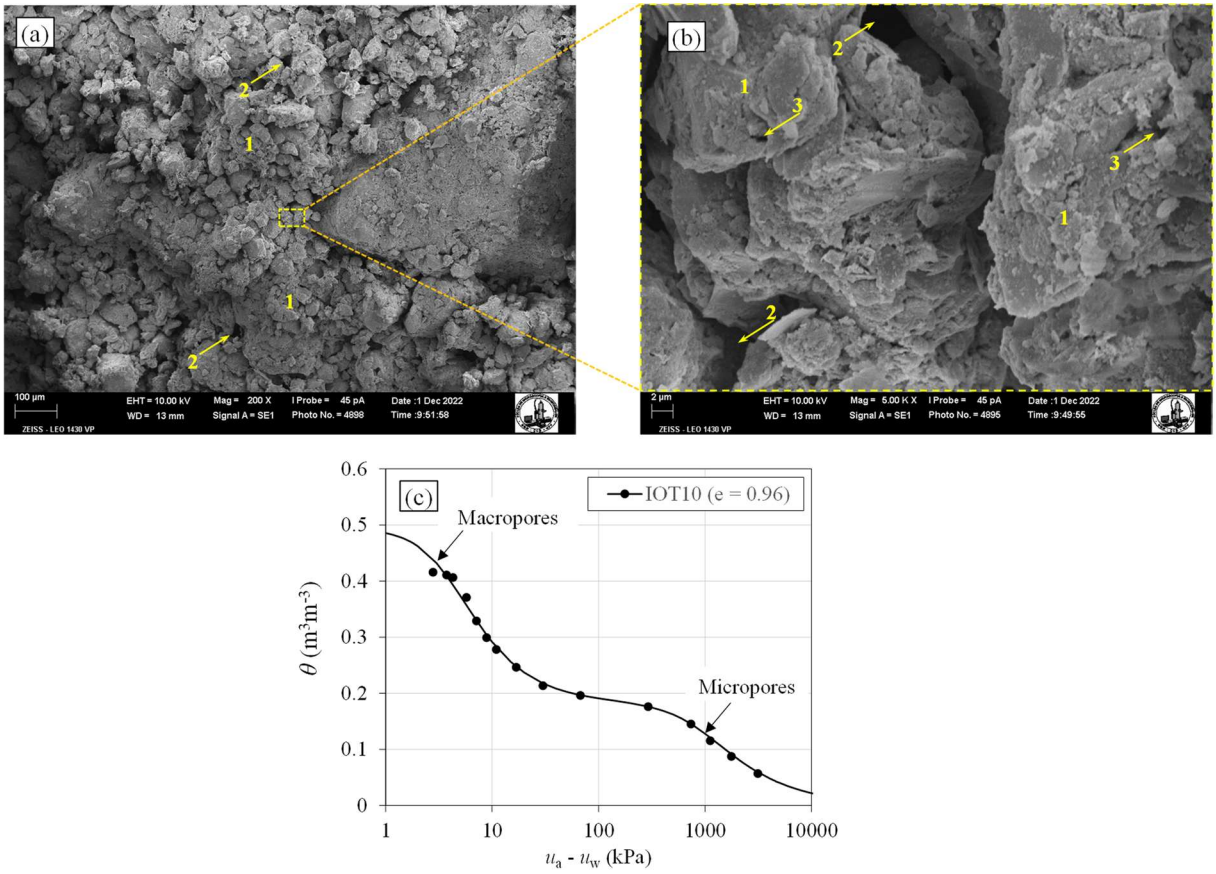

Fig. 2 SEM images and water retention behavior of sample IOT10 (e = 0.96). **a** macrostructure (200x magnification); **b** microstructure (5000x magnification); **c** water retention curve illustrating the relationship between matric suction ($u_a - u_w$) and volumetric water content (θ). 1: aggregations of fine particles; 2: macropore; 3: micropore (Dias Neto et al. 2024)

2.2 Unsaturated Hydraulic Properties of Iron Ore Tailings

Dias Neto et al. (2024) demonstrated that, due to the bimodal pore size distribution of the IOT samples, bimodal water retention functions were required to fully capture the hydraulic characteristics of both macropores and micropores. To achieve this, the authors employed the bimodal model proposed by Durner (1994), with $k = 2$ in Eq. 1. This model consists of overlapping van Genuchten-type subcurves (van Genuchten 1980), each weighted by a factor wi associated with macropores and micropores.

$$S_e = \sum_{i=1}^{k} w_i \left[\frac{1}{1 + (\alpha_i \cdot (u_a - u_w))^{n_i}}\right]^{1-1/n_i} \quad (1)$$

where S_e is the effective saturation; w_i are the weighting factors for the subcurves, constrained by $0 < w_i < 1$ and $\sum w_i = 1$; $(u_a – u_w)$ represents matric suction; α_i and n_i are empirical shape parameters, with the conditions $\alpha_i > 0$ and $n_i > 1$.

The water retention function expressed in terms of θ as a function of $(u_a – u_w)$ is given by Eq. 2:

$$\theta = \theta_r + (\theta_s - \theta_r) \cdot S_e \quad (2)$$

where θ is the volumetric water content; θ_s and θ_r are the saturated and residual volumetric water content, respectively. For all the IOT samples, the θ_r value was found to be 0 (Dias Neto et al. 2024).

The saturated hydraulic conductivity (k_s) variation with void ratio of IOT samples was described by an exponential function, as expressed by the Eq. 3:

$$k_s = A \cdot exp^{B \cdot e} \quad (3)$$

where e is the void ratio; A and B are fitting parameters. Here, A denotes the amplitude, while B controls the sensitivity of saturated hydraulic conductivity to changes in void ratio, influencing the steepness of the exponential function. Table 3 presents the regression equations for estimating the saturated hydraulic conductivity of the IOT samples based on void ratio.

Table 3 Saturated hydraulic conductivity as a function of void ratio (Dias Neto et al. 2024)

IOT	Regression equation	R^2
IOT10	$k_s = 3 \cdot 10^{-11} \cdot exp^{12.97 \cdot e}$	0.970
IOT13	$k_s = 7 \cdot 10^{-12} \cdot exp^{12.55 \cdot e}$	0.975
IOT16	$k_s = 2 \cdot 10^{-11} \cdot exp^{9.51 \cdot e}$	0.994

In this study, the bimodal unsaturated hydraulic conductivity function, $k(u_a–u_w)$, is integrated with the Mualem (1976) and van Genuchten (1980) models, as shown in Eq. 4. The fitting parameters for k_s as a function of e are summarized in Table 3, while those for the water retention curves are provided in Table 4. A detailed calibration and validation of these parameters, including comparisons with experimental data, is provided in Dias Neto et al. (2024). For instance, the k_s values obtained from Eq. 3 (Table 5) align with those reported by Saleh-Mbemba and Aubertin (2018), who found approximately $2.5 \cdot 10^{-07}$ m/s at e = 0.76 in triaxial tests on low-plasticity silt tailings. Their self-weight consolidation tests also showed a drop in vertical conductivity from $2.5 \cdot 10^{-06}$ to $2.3 \cdot 10^{-07}$ m/s as e decreased from 1.18 to 1.00, reinforcing the inverse relationship between density and hydraulic conductivity incorporated into the present model.

$$k(u_a - u_w) = k_s \cdot \left\{ \sum_{i=1}^{k} w_i \cdot [1 + (\alpha_i \cdot (u_a - u_w))^{n_i}]^{\frac{1}{n_i}-1} \right\}^{0.5} \cdot \left(\frac{\sum_{i=1}^{k} w_i \cdot \alpha_i \cdot \left\{ 1 - (\alpha_i \cdot (u_a - u_w))^{n_i-1} \cdot [1 + (\alpha_i \cdot (u_a - u_w))^{n_i}]^{\frac{1}{n_i}-1} \right\}}{\sum_{i=1}^{k} w_i \cdot \alpha_i} \right)^2 \quad (4)$$

Table 4 Water retention curve fitting parameters as a function of void ratio (Dias Neto et al. 2024)

IOT	Regression equation	R^2
IOT10	$\theta_s = 0.35 \cdot e + 0.16$	0.993
	$w_1 = 0.36 \cdot e + 0.29$	0.962
	$\alpha_1 = 0.38 \cdot e - 0.12$	0.955
	$n_1 = 1.52 \cdot e + 0.62$	0.950
	$\alpha_2 = 0.0009 \cdot e + 0.0002$	0.920
	$n_2 = -1.15 \cdot e + 2.99$	0.985
IOT13	$\theta_s = 0.30 \cdot e + 0.19$	0.993
	$w_1 = 0.67 \cdot e - 0.18$	0.981
	$\alpha_1 = 0.30 \cdot e - 0.05$	0.999
	$n_1 = 1.71 \cdot e + 0.52$	0.967
	$\alpha_2 = 0.0009 \cdot e + 0.0007$	0.917
	$n_2 = -0.37 \cdot e + 2.12$	0.942
IOT16	$\theta_s = 0.25 \cdot e + 0.24$	0.993
	$w_1 = 0.36 \cdot e + 0.05$	0.993
	$\alpha_1 = 0.48 \cdot e - 0.30$	0.988
	$n_1 = 0.84 \cdot e + 1.05$	0.962
	$\alpha_2 = 0.0014 \cdot e - 0.0001$	0.979
	$n_2 = -0.63 \cdot e + 2.60$	0.997

2.3 Simulated Scenarios: Tailings Variability, Void Ratio, and Undercompaction

This study aims to analyze how variations in water retention characteristics and hydraulic conductivity of IOT affect seepage behavior and overall stability in a filtered tailings stack. To

achieve this, three primary factors were examined: variations in void ratio, tailings heterogeneity, and undercompaction resulting from reduced compaction efficiency during the rainy seasons.

Undercompaction, as considered in this study, is introduced as a hypothetical scenario rather than a reflection of current operational practices. It assumes that, to reduce delays caused by the drying time required for off-specification tailings, compaction could occur at water contents above the Proctor-optimum. While this approach might expedite operations, it could result in a significantly reduced degree of compaction, falling outside specified design parameters and potentially affecting the hydromechanical behavior of the stack. Although not commonly practiced, this scenario highlights the consequences of compacting tailings with higher water contents.

The simulation of the filtered tailings stack construction, using the unsaturated hydraulic properties of the IOT10 sample at a void ratio corresponding to 100% degree of compaction, as per the standard Proctor test (IOT10-100%), was established as the reference scenario. To assess the influence of void ratio variations on seepage behavior and stack stability, additional scenarios were simulated using the unsaturated hydraulic properties of the IOT10 sample at compaction levels of 80% (IOT10-80%) and 90% (IOT10-90%), alongside the reference scenario (IOT10-100%). To further investigate the effects of tailings heterogeneity, two additional samples, IOT13 and IOT16, were incorporated into the analysis, each modeled at a 100% degree of compaction (IOT13-100% and IOT16-100%) based on their respective standard Proctor test results.

The calculation of hydraulic properties is based on the equations outlined in Section 2.2. Table 5 provides a summary of the geotechnical parameters used in the simulations, while Figs. 3 and 4 present the water retention and unsaturated hydraulic conductivity curves implemented for each void ratio/sample in the numerical model.

Table 5 Variation in hydraulic properties due to changes in void ratio and tailings variability: geotechnical parameters employed in the simulations.

	IOT10-100%	IOT10-90%	IOT10-80%	IOT13-100%	IOT16-100%
Void ratio – e	0.47	0.64	0.84	0.58	0.72
Porosity - n	0.32	0.39	0.46	0.37	0.42
Dry unit weight - γ_d (kN/m³)	21.4	19.3	17.1	20.7	19.2
Unit weight - γ (kN/m³)	23.9	21.5	19.1	23.7	22.4
Saturated unit weight - γ_{sat} (kN/m³)	24.5	23.1	21.6	24.3	23.3
Saturated hydraulic conductivity - k_s (m/s)	$1.33 \cdot 10^{-08}$	$1.21 \cdot 10^{-07}$	$1.62 \cdot 10^{-06}$	$1.01 \cdot 10^{-08}$	$1.88 \cdot 10^{-08}$
Weighting factor - w_1	0.46	0.52	0.59	0.21	0.31
Water retention curve fitting parameter α_1 (kPa^{-1})	0.06	0.12	0.20	0.13	0.04
Water retention curve fitting parameter n_1	1.34	1.59	1.90	1.51	1.66
Air entry value - AEV_1 (kPa)	16.94	8.07	5.00	7.78	25.18
Water retention curve fitting parameter α_2 (kPa^{-1})	0.0006	0.0008	0.0010	0.0012	0.0010
Water retention curve fitting parameter n_2	2.45	2.25	2.02	1.90	2.14

The saturated volumetric water content (θ_s) was assumed to be equal to the total porosity (n)

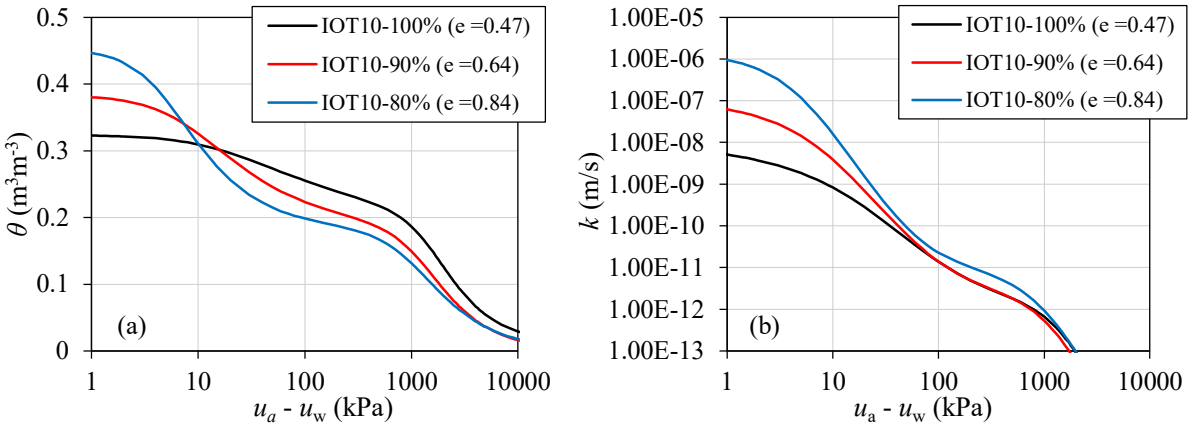

Fig. 3 Variation in hydraulic properties with changes in void ratio. **a** water retention curves; **b** unsaturated hydraulic conductivity curves

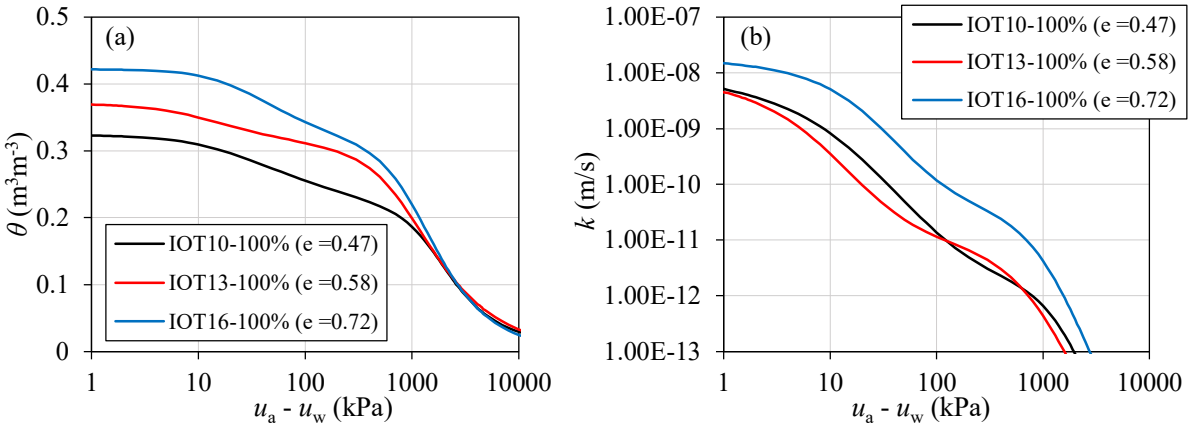

Fig. 4 Variation in hydraulic properties due to tailings variability. **a** water retention curves; **b** unsaturated hydraulic conductivity curves

The effects of undercompaction were assessed through two additional scenarios, compared with the filtered tailings stack modeled using the unsaturated hydraulic properties of the reference scenario (IOT10-100%). The first scenario simulated reduced compaction efficiency during rainy periods, where higher water contents in the tailings reduced machinery efficiency, resulting in a void ratio equivalent to a 90% degree of compaction (IOT10-90%). The second scenario represented even more limited compaction, where only bulldozer spreading occurred during the rainy season, leading to a void ratio corresponding to an 80% degree of compaction (IOT10-80%). These scenarios were designed to reflect hypothetical conditions of undercompaction caused by alternating wet and dry periods. As described in Section 2.5, these scenarios were modeled by alternating successive 10-meter lifts, incorporating IOT10-100% properties for dry periods and IOT10-80%/IOT10-90% properties for rainy periods.

Since the primary focus of this study is on the behavior of the stacked tailings, the foundation of the filtered tailings stack was modeled as a homogeneous, single material. For the unsaturated hydraulic properties of the foundation, a pre-existing "simple" model available in the RS2 finite element software (Rocscience Inc.) was employed to represent both the water retention and unsaturated hydraulic functions (Fig. 5). These functions were based on a porosity of 0.4 and a saturated hydraulic conductivity of $1 \cdot 10^{-08}$ m/s, a value derived from infiltration tests conducted during field investigations at the stack's site, as reported by Venturin (2022).

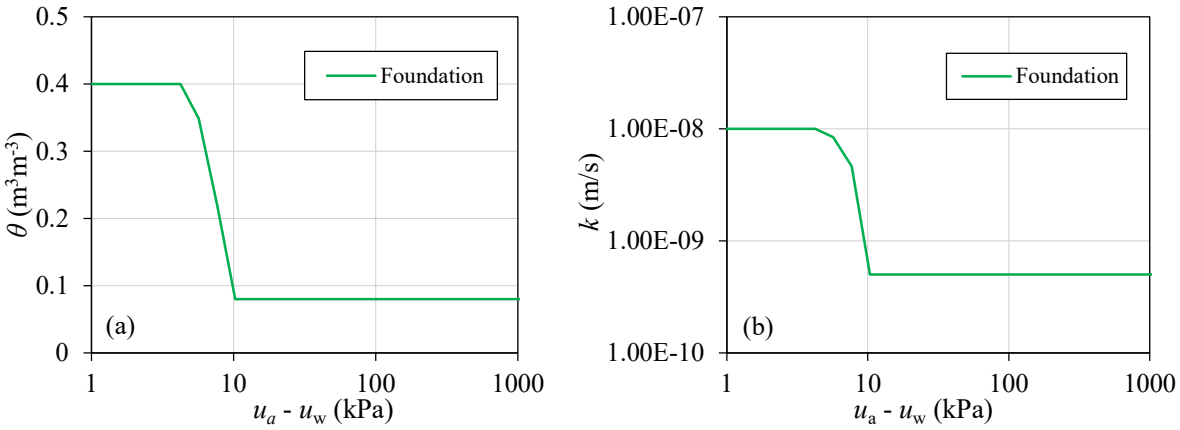

Fig. 5 Hydraulic properties of the foundation. **a** water retention curve; **b** unsaturated hydraulic conductivity curve

2.4 Mechanical Properties

The elastoplastic model with the Mohr-Coulomb (MC) failure criterion, as implemented in RS2 finite element software by Rocscience Inc., was employed to simulate the stress-strain behavior of a filtered tailings stack during its construction. Unsaturated soil mechanics were incorporated using Vanapalli et al. (1996) unsaturated shear strength formulation, which is based on the Mohr-Coulomb criterion and calculates shear strength (τ) as a function of volumetric water content (θ), as shown in Eq. 5.

$$\tau = c' + (\sigma - u_a) \cdot \tan\varphi' + (u_a - u_w) \cdot \left[\tan\varphi' \cdot \left(\frac{\theta - \theta_r}{\theta_s - \theta_r}\right)\right] \quad (5)$$

where c' is the effective cohesion intercept, ($\sigma - u_a$) is the net normal stress on the plane of failure at failure and φ' is the effective angle of internal friction.

To assess the mechanical stability of the stack, slope stability analyses were conducted using Slide2 limit equilibrium software, also by Rocscience Inc., which incorporated the pore pressure grids generated across the different construction stages of the filtered tailings stack simulated in the numerical analyses.

The decision to evaluate stack stability using limit equilibrium analysis aligns with Brazilian standards and global regulations, which establish this method as a primary reference for assessing the stability of mine waste disposal facilities. As noted by Schnaid et al. (2020), the standard practice among engineers continues to rely on stability verifications and the interpretation of monitoring data based on threshold limits implicitly associated with limit equilibrium analysis.

In Slide2, the Fredlund et al. (1978) formulation (Eq. 6) is the only available approach to account for unsaturated shear strength when negative pore pressures (commonly referred to as matric suction) result from water pressure grid interpolation.

$$\tau = c' + (\sigma - u_a) \cdot \tan \varphi' + (u_a - u_w) \cdot \tan \varphi^b \quad (6)$$

where φ^b is angle of friction accounting for matric suction contribution to shear strength. While Vanapalli et al. (1996) uses the water retention functions presented in Section 2.3 to determine φ^b, the Fredlund et al. (1978) method requires users to input φ^b and an air-entry value.

The effect of the air-entry value in the Fredlund et al. (1978) formulation is as follows: for matric suctions below the air-entry value, the saturated effective stress friction angle is used to account for the contribution of suction to shear strength; for matric suctions exceeding the air-entry value, the unsaturated shear strength angle, φ^b, is applied. The air-entry values used in the slope stability analysis were presented in Table 5, and φ^b was assumed to be 15° for all cases. The two formulations yield nearly identical increases in shear strength for matric suctions below the air-entry value. For values exceeding the air-entry value, a conservative estimate of the shear strength increase is obtained using φ^b = 15º in Eq. 6 compared to Eq. 5, particularly for the matric suction levels developed within the tailings during the simulations, as will be further discussed in Section 3.

The adoption of φ^b = 15º is supported by Zhang et al. (2014), who demonstrated that this value provides a reliable estimate of shear strength gains from matric suction for soils with air-entry values between 20 and 200 kPa. Li et al. (2021) similarly reported that assuming φ^b = 15º yields reasonable stability predictions under moderate suction conditions. Huat et al. (2006) and Oliveira et al. (2022) also found that φ^b values ranging from 10° to 20° are consistent with the behavior of tropical unsaturated soils under infiltration. For mining applications, Jesus et al. (2023) observed that compacted, partially saturated iron ore tailings maintain elevated shear strength, indicating that φ^b may approach φ' in such materials. Altogether, adopting φ^b = 15º remains a conservative and technically justified assumption in the absence of unsaturated shear strength data for filtered tailings.

Additionally, the application of the water retention parameters presented in Table 5 within the Vanapalli et al. (1996) formulation reveals a clear relationship between compaction levels and suction-induced shear strength increase. For a suction level of 100 kPa—representative of

the maximum values observed in the simulations—the predicted increase in shear strength reached approximately 55 kPa for all samples compacted to 100% of standard Proctor energy, regardless of material type (IOT10, IOT13, or IOT16). However, for lower compaction levels of IOT10, the increase was reduced to approximately 40 kPa for IOT10-90% and 30 kPa for IOT10-80%, reflecting the influence of higher void ratios and saturated volumetric water contents. Although lower void ratio samples tend to develop reduced suction levels due to their proximity to saturation, the higher suctions observed in loosely compacted materials amplify the relative contribution of suction to shear strength.

Since the primary objective of this study is to evaluate how variations in unsaturated hydraulic properties affect seepage and the stability of a filtered tailings stack, all simulations will consistently use the same set of strength and stiffness parameters for the filtered tailings. The MC model parameters are derived from Oliveira (2021), who conducted a geotechnical characterization of the IOTmech sample and evaluated the performance of various constitutive models based on triaxial test results. Table 6 summarizes these parameters, along with those for the foundation material (Oliveira 2021). In the numerical and slope stability analyses, the increase in shear strength due to suction was not considered for the foundation material.

Table 5 Parameters for elastoplastic model with Mohr-Coulomb failure criterion (Oliveira 2021)

Parameter	IOTmech	Foundation	Description
φ'_p	34.00	35.00	Effective peak friction angle (degrees)
c'_p	0.00	10.50	Effective peak cohesion intercept (kPa)
φ'_{res}	33.00	35.00	Effective residual friction angle (degrees)
c'_{res}	0.00	10.50	Effective residual cohesion intercept (kPa)
E	66,200	75,000	Elastic modulus (kPa)
v	0.20	0.30	Poisson's ratio

2.5 Modeling Strategy

For all the seven scenarios described in Section 2.3, transient, fully coupled seepage-deformation analyses were conducted using the consolidation theory developed by Biot (1941), as implemented in RS2 software, to model the interlayer deposition of tailings during stack construction under alternating dry and wet conditions. The construction sequence was modeled to capture both the buildup and dissipation of strain-induced pore pressure, influenced by the hydraulic properties of the compacted tailings.

The stack evaluated in this study is designed for the storage of compacted, filtered tailings generated from iron ore beneficiation in the QF. Table 7 summarizes the key characteristics of the stack, while Fig. 6 illustrates its layout. Fig. 7 shows the critical section A-A′ at the end of construction, which serves as the basis for the numerical analyses. Special attention is given to the left slope of section A-A′, which will be the focus of the discussions in this study. Fig. 7 also depicts the various construction stages leading up to the stack's maximum height at section A-A′.

Table 6 Key characteristic of the filtered tailings stack

Characteristics	Details
Stored Material	Filtered iron ore tailings
Location	Quadrilátero Ferrífero, Brazil
Maximum height (m)	161.00
Stack volume (m³)	6,430,000
Total occupied area (ha)	5.7
Overall slope inclination	1V:3.4H
Slope inclination between berms	1V:2.5H
Bench height (m)	10.00
Berm width (m)	10.00

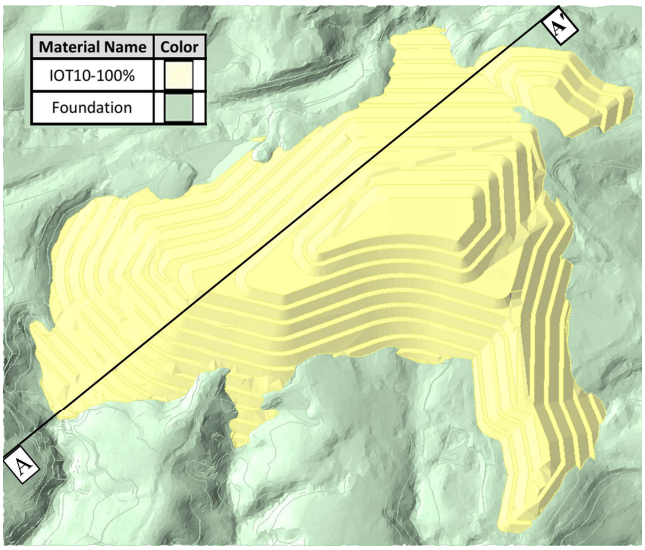

Fig. 6 Layout of the filtered tailings stack

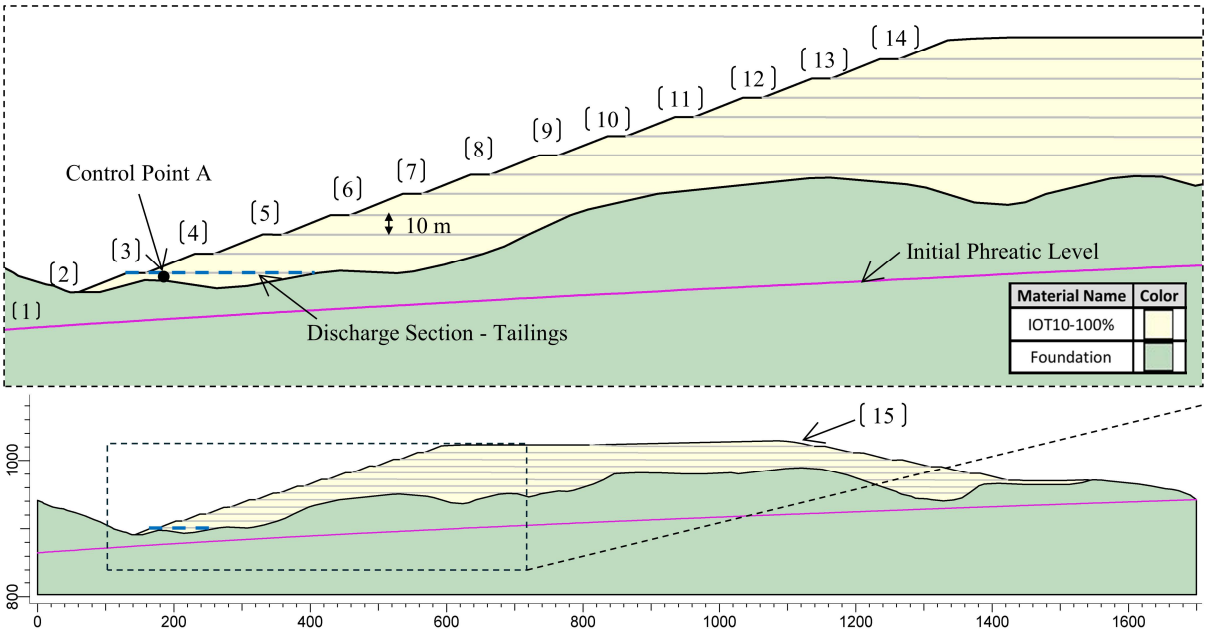

Fig. 7 Critical section A-A′ of the filtered tailings stack at the end of construction

The final geometry of the stack was simulated in 15 construction stages. The initial phreatic surface, corresponding to Stage 1 (Initial Stage), was established through steady-state seepage analysis and was located approximately 15 meters below the foundation surface at the base of the left slope in Section A-A′ (Fig. 7). To reproduce this condition, a constant total head of 942 m was applied at the right lateral boundary and 864.5 m at the left lateral boundary. These boundary conditions were maintained throughout all construction stages.

In subsequent stages (Stages 2 to 15), stack construction was modeled under transient flow conditions, with compacted layers of 10 meters added sequentially until the stack reached its final height (Fig.7). Each stage lasted six months, with even-numbered stages corresponding to dry periods and odd-numbered stages to rainy seasons. An additional stage (Stage 16) was simulated to represent the first dry period after completing the stack's final geometry.

A discharge section was implemented in the model at the top of the first compacted layer (Fig. 7) to evaluate seepage through the compacted tailings during stack construction. This modeling strategy is supported by the findings of Vizcarra (2021), which demonstrate—based on numerical simulations—the critical role of low-permeability layers in controlling pore pressure dissipation and maintaining slope stability during staged construction.

A control point A was established at the upper surface of the first compacted tailings layer (Fig. 7) to monitor degree of saturation, pore pressure, and total displacement during construction. This point, chosen for its proximity to most failure surfaces identified in the slope

stability analyses, provides critical insights into the evolution of the Factor of Safety (FoS) during the stack construction, which will be discussed in detail in Section 3.

To ensure consistent interpretation of the results, the safety assessment focused on the overall stability of the stack, with the critical slip surface defined as the one representing global failure. In later stages, this typically corresponds to deeper surfaces, while in early stages—when the stack consisted of only a few benches—shallower slip surfaces near bench levels were also considered representative of overall failure due to scale.

During the rainy periods of the filtered tailings stack construction, a constant infiltration rate of 0.26 mm/day was uniformly applied across the entire stack surface. This value was defined based on a water balance analysis conducted by Venturin (2022) for the area adjacent to the footprint of the stack designed in this study. The modeling approach adopted by Venturin (2022) included calibration using observed phreatic levels from boreholes and discharge measurements from natural springs at the foundation. Additionally, a sensitivity analysis was performed to assess the influence of different surface runoff coefficients (0.45, 0.55, and 0.65) on the simulated drainage response. The results indicated that variations in the runoff coefficient had minimal effect on the overall performance of the drainage system.

Fig. 8 presents the mean monthly precipitation records along with the average monthly potential evapotranspiration ETP_{pot}, calculated using the Reichardt and Timm (2004) method, which defines ETP_{pot} as the product of actual evaporation measurements and a correlation factor of 0.7, specific to stack areas. The infiltration rate used in the numerical modeling was derived by applying a surface runoff coefficient of 0.65, based on the mean infiltration rates during the months of highest precipitation (November to March). According to Venturin (2022), this value represents the lower bound of net infiltration under wet-season conditions. Although rainfall variability was not explicitly represented in the model, the use of a constant infiltration rate served to underscore the relevance of incorporating climatic boundary conditions into unsaturated coupled flow–deformation analyses.

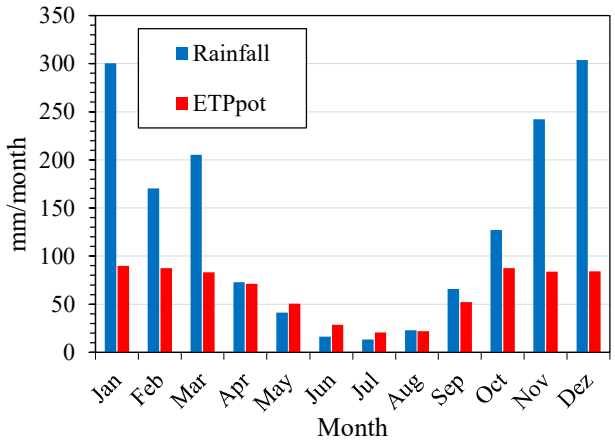

Fig. 8 Climate data for the area surrounding the stack: rainfall and potential evapotranspiration

The finite element mesh used in the analyses consists of 17,921 six-noded triangular elements and 36,662 nodes. A finer mesh was applied to the region of interest, which corresponds to the successive layers of compacted tailings, to more accurately capture the behavior of water retention, flow, and deformation. Regarding the mechanical boundary conditions, the base of the model was assumed to be fully fixed, with the lateral boundaries constrained horizontally. The surface was treated as a free boundary.

3. RESULTS AND DISCUSSION

3.1 Variations in Void Ratio

The influence of void ratio on the behavior of the filtered tailings stack during construction was investigated through numerical simulations of three different scenarios: IOT10-100% (e = 0.47), IOT10-90% (e = 0.64), and IOT10-80% (e = 0.84). Fig. 9 illustrates the fluctuations in FoS, degree of saturation, pore pressure, and seepage, assessed at the upper surface of the first compacted tailings layer for each scenario. The degree of saturation and pore pressure were monitored at control point A, as shown in Fig. 7. As previously discussed, this point was chosen as a critical location near most failure surfaces identified in the slope stability analyses.

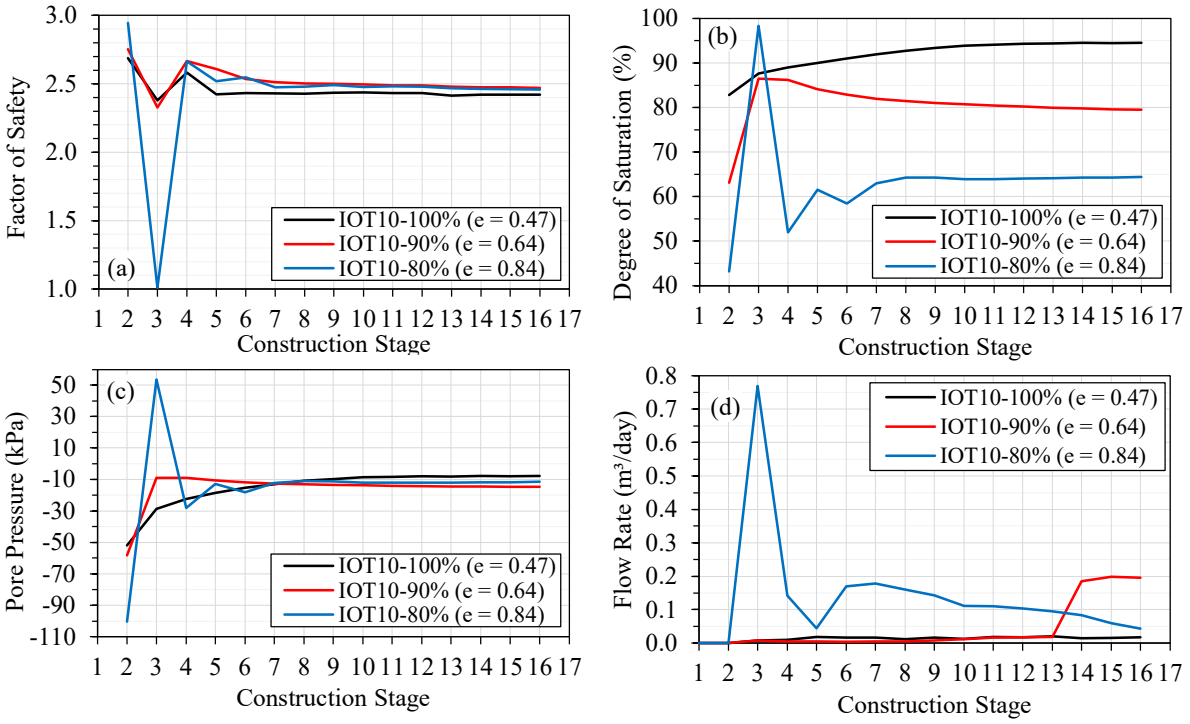

Fig. 9 Influence of void ratio variations on **a** stability, **b** saturation, **c** pore pressure, and **d** seepage through the tailings during construction stages

Fig. 9a shows that the FoS reaches its minimum value during Stage 3, corresponding to the first rainy period. This drop is most pronounced for IOT10-80%, where the FoS approaches critical instability (FoS ~ 1.0), highlighting the increase vulnerability of undercompacted tailings during rainy periods. In contrast, for IOT10-90% and IOT10-100%, the FoS remains above 2.3, reflecting improved stability due to higher compaction levels.

After the sharp drop in FoS observed in Stage 3, all scenarios exhibit a significant recovery in Stage 4, corresponding to the subsequent dry period (Fig. 9a). However, Stage 5 (a rainy period) induces a small drop in FoS, reflecting the ongoing influence of alternating weather conditions on stability during construction. From Stage 6 onward, the FoS undergoes smaller changes, signaling a transition toward equilibrium as construction progresses. Among the scenarios, IOT10-80% exhibits greater sensitivity to subsequent rainy periods, with more noticeable fluctuations in FoS before stabilizing. In contrast, IOT10-100% demonstrates the least variation in FoS throughout construction, despite having a slightly lower FoS in the final stack geometry configuration.

The FoS in Fig. 9a is closely linked to the pore pressure behavior shown in Fig. 9c, as pore pressure plays a critical role in defining the effective stress and the suction contribution to shear strength. The emergence of a positive pore pressure peak for the scenario IOT10-80% at

control point A during Stage 3 explains its critically low FoS (~ 1.0). The larger void ratio in IOT10-80% (e = 0.84) creates a more porous structure, which retains more water during rainy periods, resulting in higher degrees of saturation compared to more compacted scenarios (Fig. 9b).

During Stage 3, the higher degree of saturation in IOT10-80% leads to a significant increase in hydraulic conductivity, accelerating water infiltration into the tailings (Fig 9d). In the early stages, when the stack is relatively small, saturation is reached more quickly as water infiltrates and fills the larger pore spaces (Fig 9b). This rapid saturation causes matric suction to decrease (negative pore pressures become less negative) as air-filled voids are replaced by water (Fig 9c). Once full saturation is reached, pore pressures continue to rise, transitioning into positive values and further reducing effective stress, which explains the critical drop in FoS observed during this stage (Fig 9a). In contrast, during the subsequent stages, as the degree of saturation decreases, the hydraulic conductivity diminishes significantly, slowing water movement and allowing suction to recover, which in turn stabilizes the stack.

The scenarios IOT10-90% and IOT10-100% exhibit similar trends throughout the construction process, with both demonstrating higher stability due to maintaining matric suction (negative pore pressures) throughout construction (Fig 9c). However, in Stage 3, both scenarios experience a significant rise in degree of saturation (Fig. 9b) follow by the reduction in matric suction, as pore pressure becomes less negative, which contributes to a drop in their FoS (Fig 9a). Over subsequent construction stages, as saturation levels and pore pressures stabilize, the corresponding stabilization in the FoS reflects the balance between load application, water storage and the dissipation of excess pore pressures.

While these trends suggest similarities between IOT10-90% and IOT10-100%, their distinct void ratios (e = 0.64 for IOT10-90% and e = 0.47 for IOT10-100%) lead to subtle but important differences in hydraulic behavior and stability. IOT10-100%, with its smaller void ratio, exhibits lower hydraulic conductivity due to its denser structure but operates closer to saturation, which increases its hydraulic conductivity under near-saturated conditions. In contrast, IOT10-90%, with a larger void ratio, inherently has higher hydraulic conductivity but maintains a lower degree of saturation, which limits water movement and reduces its overall hydraulic conductivity. This interplay between void ratio and saturation results in similar seepage rates through the tailings (Fig. 9d) for both scenarios until Stage 13, after which IOT10-90% shows increased seepage.

Pore pressure development further distinguishes the scenarios. The higher degree of saturation in IOT10-100% during the later stages results in slightly reduced matric suction compared to IOT10-90% and IOT10-80% (Fig. 9c). This reduction in matric suction explains the slightly lower FoS of IOT10-100% in the final stages (Fig. 9a).

Figs. 10, 11, and 12 complement the observations from Fig. 9 by presenting the contours of degree of saturation, pore pressure, and the slope failure surface corresponding to the minimum FoS at Stage 3, which represents the most critical stability condition throughout construction for the IOT10-100%, IOT10-90%, and IOT10-80% scenarios, respectively.

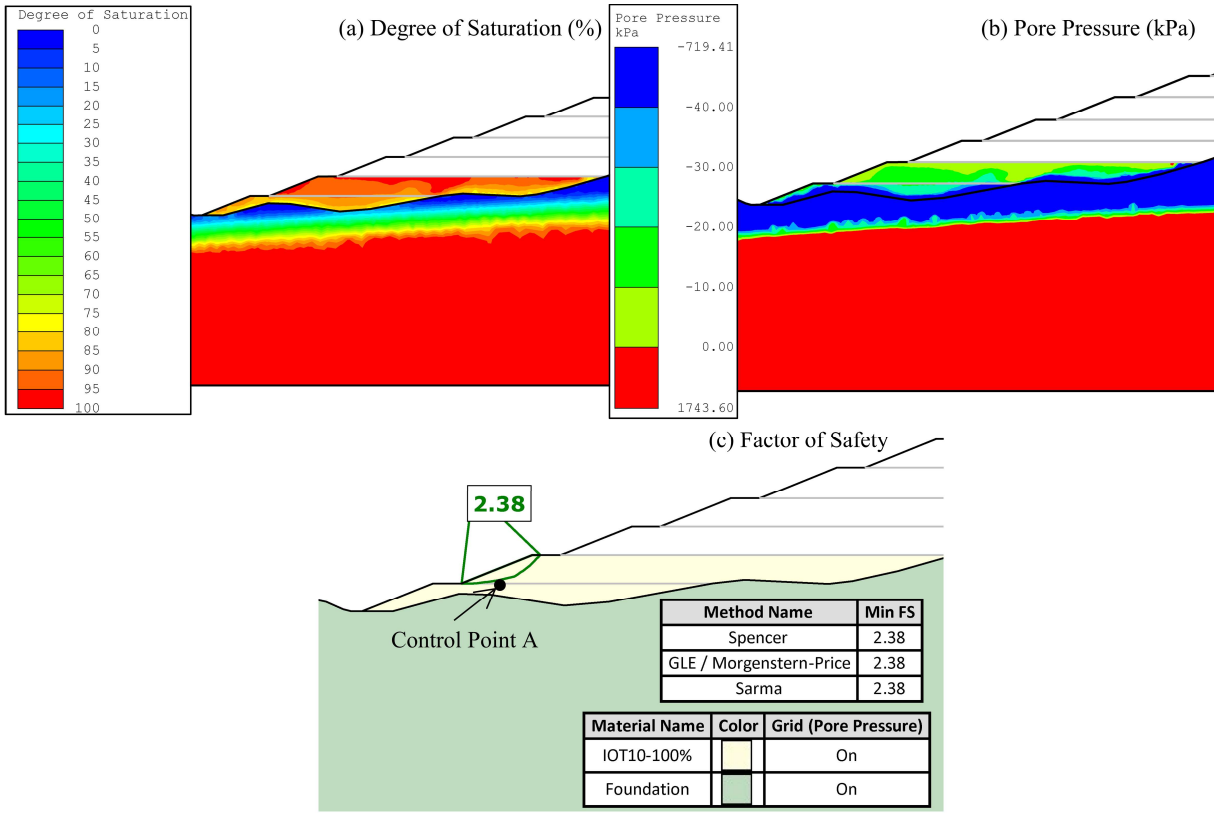

Fig. 10 Response of the filtered tailings stack construction with IOT10-100% at Stage 3. **a** degree of saturation. **b** pore pressure. **c** factor of safety

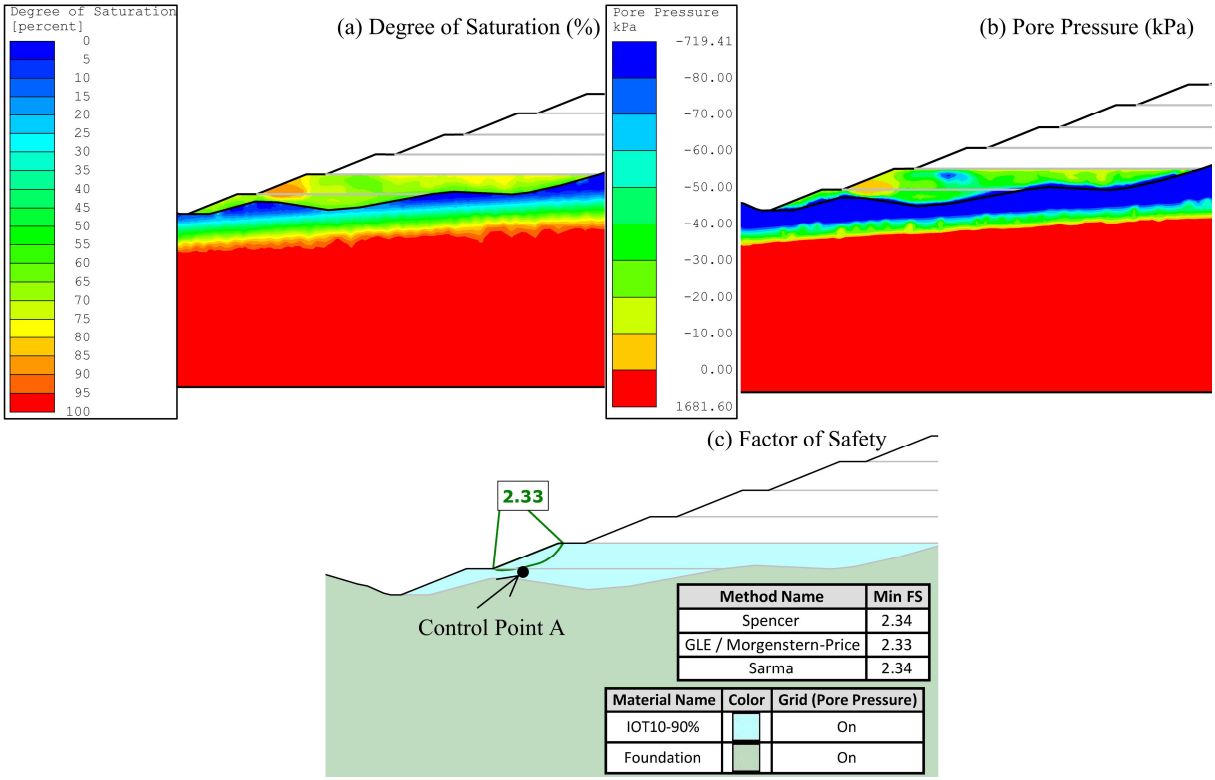

Fig. 11 Response of the filtered tailings stack construction with IOT10-90% at Stage 3. **a** degree of saturation. **b** pore pressure. **c** factor of safety

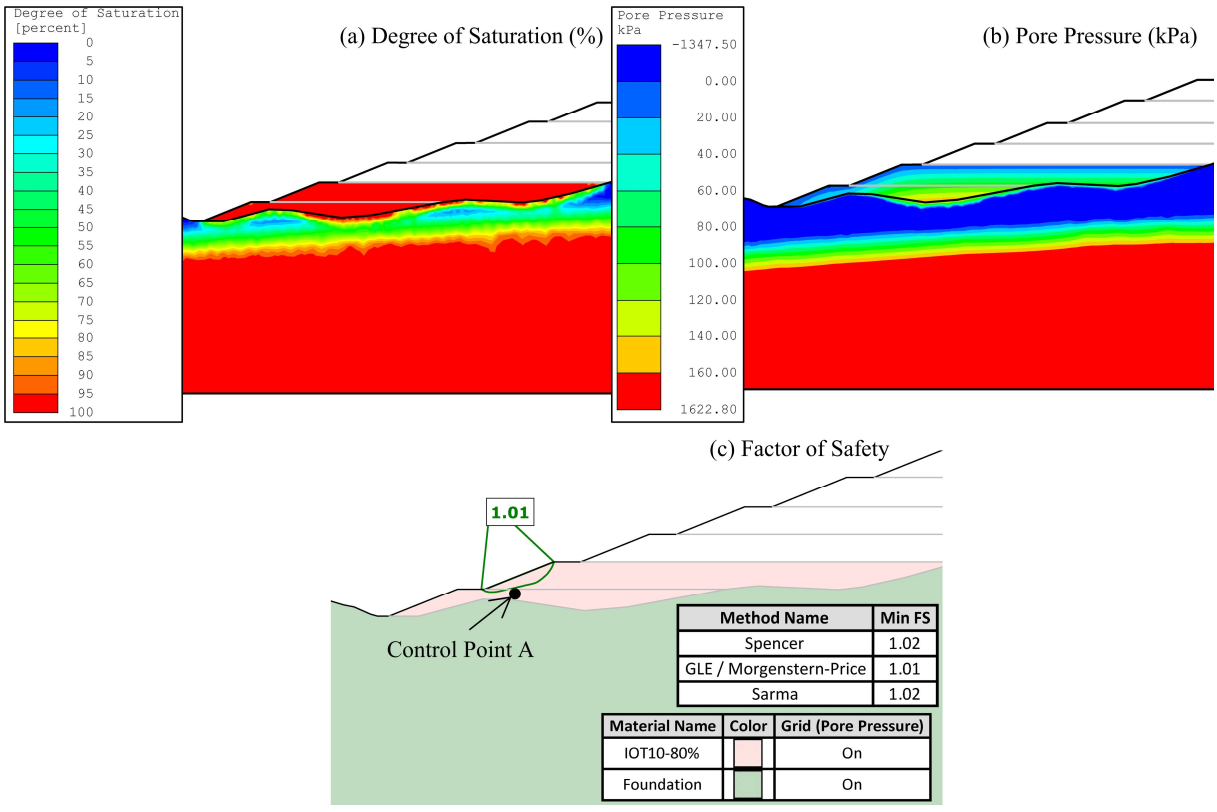

Fig. 12 Response of the filtered tailings stack construction with IOT10-80% at Stage 3. **a** degree of saturation. **b** pore pressure. **c** factor of safety

In Fig. 10a, corresponding to the IOT10-100% scenario, degrees of saturation exceed 95% near the surface and gradually decrease toward the base of the stack. Despite the high saturation levels, the pore pressure contours in Fig. 10b indicate that matric suction persists throughout the stack, with no development of positive pore pressures. This behavior is attributed to the lower void ratio (e = 0.47) and denser structure of IOT10-100%, which limit hydraulic conductivity and reduce water infiltration. These factors ensure stability even under near-saturated conditions, resulting in the highest FoS = 2.38 among the scenarios (Fig. 10c).

In contrast, IOT10-80% (Fig. 12a) is fully saturated throughout the stack due to its higher void ratio (e = 0.84), which allows for greater water infiltration and faster saturation. This condition leads to the formation of a perched water table near the surface, as shown in Fig. 12b, where positive pore pressures develop and increase linearly with depth, exceeding 140 kPa. These elevated pore pressures significantly reduce effective stress, resulting in the critically low FoS = 1.01 (Fig. 12c).

In Fig. 11a, corresponding to the IOT10-90% scenario, maximum saturation occurs near the slope face but remains below 90%. Positive pore pressures, as shown in Fig. 11b, are confined to this localized area, reaching values above 40 kPa, while matric suction prevails throughout most of the stack. These localized positive pore pressures reduce effective stress at the slope face, resulting in a slightly lower FoS = 2.33 compared to the FoS = 2.38 observed in the IOT10-100% scenario (Figs. 11c and 10c, respectively).

Figs. 13, 14, and 15 refer to the contours of degree of saturation, pore pressure, total displacement, and the slope failure surface corresponding to the minimum FoS at Stage 16, representing the final stack geometry configuration at the end of construction for the IOT10-100%, IOT10-90%, and IOT10-80% scenarios, respectively.

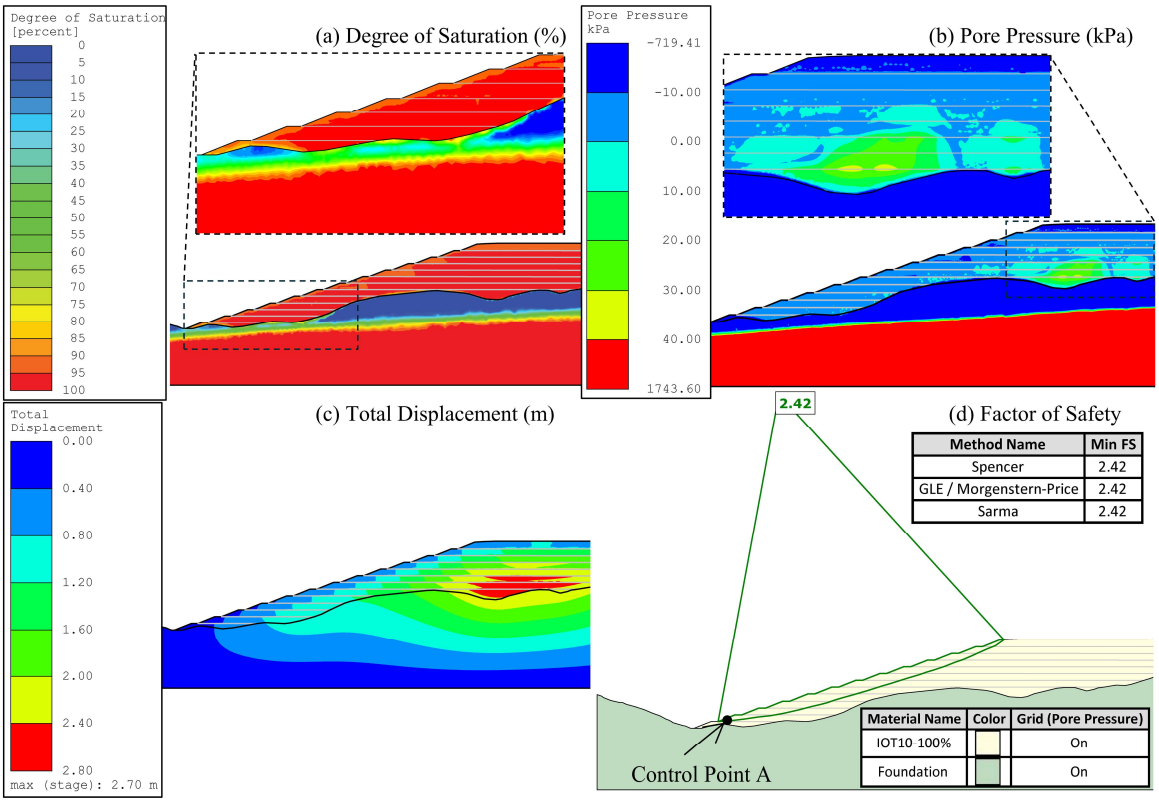

Fig. 13 Response of the filtered tailings stack construction with IOT10-100% at Stage 16. **a** degree of saturation. **b** pore pressure. **c** total displacement. **d** factor of safety

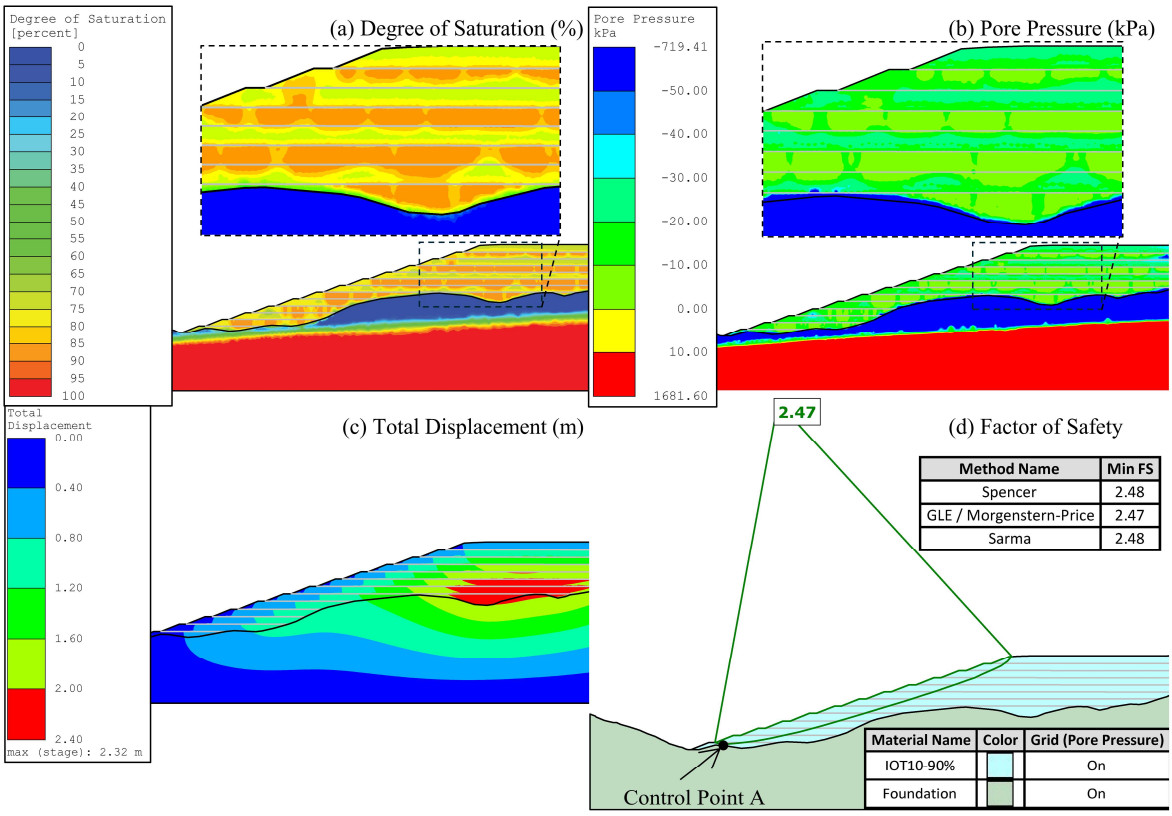

Fig. 14 Response of the filtered tailings stack construction with IOT10-90% at Stage 16. **a** degree of saturation. **b** pore pressure. **c** total displacement. **d** factor of safety

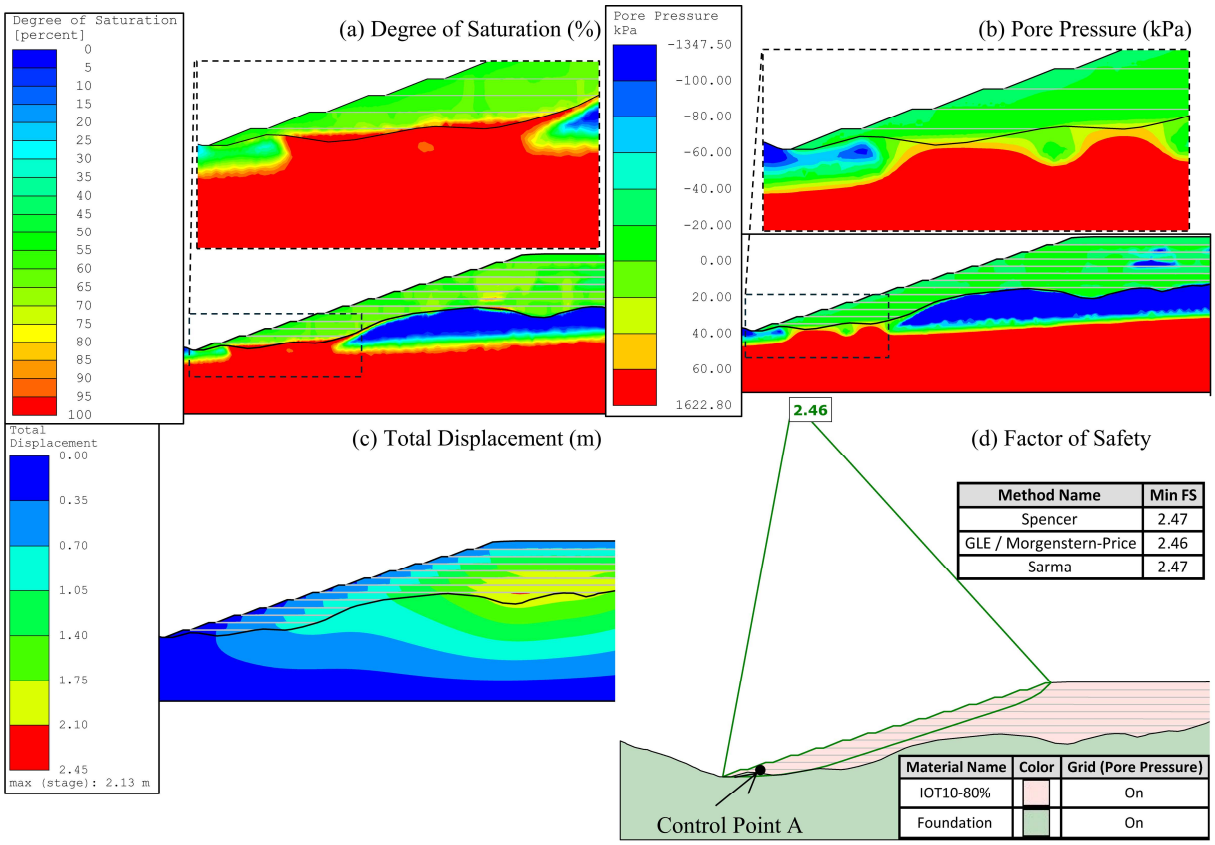

Fig. 15 Response of the filtered tailings stack construction with IOT10-80% at Stage 16. **a** degree of saturation. **b** pore pressure. **c** total displacement. **d** factor of safety

By the end of construction in the IOT10-100% scenario, as shown in Fig. 13a, increased saturation levels are primarily driven by void ratio reduction caused by overburden stresses. The lower void ratio of these dense tailings (e = 0.47) limits seepage and water mobility, as seen in Fig. 9d, minimizing the influence of infiltration during rainy seasons. Degrees of saturation exceed 95% across most of the stack, except near the slope surface, where levels range between 90% and 95%. Pore pressure development is confined to regions with the greatest tailings thickness, exceeding 30 kPa, while the rest of the stack retains matric suction up to 10 kPa (Fig. 13b). These conditions ensure the stability of the stack, resulting in a FoS = 2.42 (Fig. 13d).

In contrast, by the end of construction in the IOT10-90% scenario, the degree of saturation in compacted layers reflects the seasonal conditions during deposition (Fig. 14a). Layers compacted during rainy seasons (odd stages) maintain higher saturation levels (85%–90%), while those compacted during dry seasons (even stages) exhibit lower saturation levels (70%–80%). Although the increased void ratio allows for greater water retention during rainy periods, seepage remains restricted within the tailings, as saturation differences persist throughout

construction. Matric suction predominates across the stack, reaching up to 30 kPa (Fig. 14b), contributing to overall stability and resulting in a FoS = 2.47 (Fig. 14d).

As shown in Fig. 9d, in the IOT10-80% scenario, significant water movement toward the base of the stack occurs throughout construction, driven by its higher compacted void ratio (e = 0.84) and greater hydraulic conductivity. The lower permeability of the foundation delays further infiltration, leading to the formation of a saturated zone at the base of the stack by the end of construction (Fig. 15a), where positive pore pressures exceed 40kPa (Fig. 15b) within the tailings. This water accumulation gradually causes the water table within the stack to merge with the groundwater in the foundation as construction progresses. In contrast, the rest of the stack remains unsaturated, with degrees of saturation ranging from 50% to 65% and matric suction values up to 30 kPa (Fig. 15a), contributing to the overall stability of the stack with a FoS = 2.46 (Fig. 15d).

The contours of total displacement at the end of stack construction, presented in Figs. 13c, 14c, and 15c for the IOT10-100%, IOT10-90%, and IOT10-80% scenarios, respectively, exhibit consistent trends, with the greatest displacement observed in regions of maximum tailings thickness. Maximum displacements are recorded as 2.70 m for IOT10-100%, 2.32 m for IOT10-90%, and 2.13 m for IOT10-80%. These differences in displacement magnitude are attributed to variations in unit weight across the scenarios (Table 5), as identical stiffness parameters were adopted in all cases.

3.2 Tailings Heterogeneity

The impact of tailings variability on the behavior of the filtered tailings stack during construction was analyzed using numerical simulations for three distinct scenarios: IOT10-100% (e = 0.47), IOT13-100% (e = 0.58), and IOT16-100% (e = 0.72). Fig. 16 presents the changes in FoS, degree of saturation, pore pressure and seepage, evaluated at the upper surface of the first compacted tailings layer for each scenario. Consistent with previous analyses, degree of saturation and pore pressure were monitored at control point A.

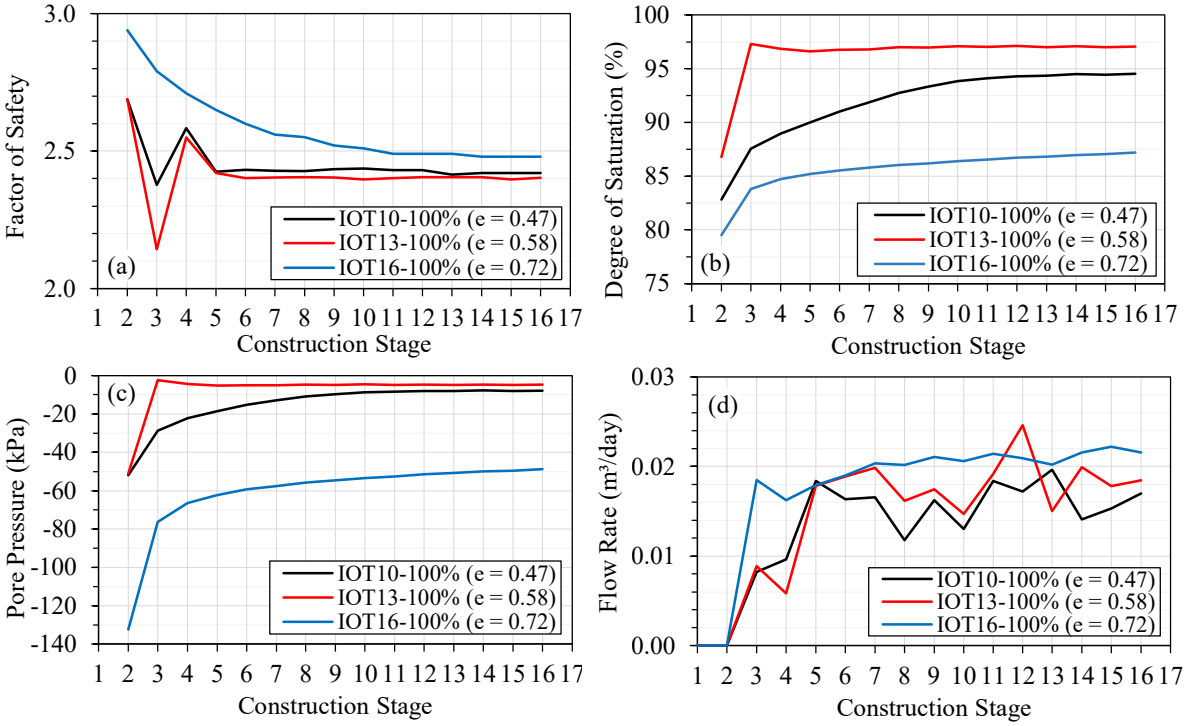

Fig. 16 Influence of tailings heterogeneity on **a** stability, **b** saturation, **c** pore pressure, **d** seepage through the tailings during construction stages

The FoS trends shown in Fig. 16a reveal that, across all construction stages, IOT16-100% achieves the highest FoS, followed by IOT10-100%, while IOT13-100% exhibits the lowest values. This behavior aligns closely with the degree of saturation and pore pressure trends observed at control point A (Fig. 16b). Among the scenarios, IOT13-100% consistently exhibits the highest degree of saturation, followed by IOT10-100% and then IOT16-100%. The lower degree of saturation in IOT16-100% results in higher matric suction throughout construction, as shown in Fig. 16c, contributing to its higher FoS. In contrast, the higher degree of saturation in IOT13-100% reduces matric suction, leading to its comparatively lower FoS.

Despite the distinctions among the three scenarios, the behavior of IOT10-100% closely resembles that of IOT13-100% in terms of FoS, degree of saturation, and pore pressure trends (Figs. 16a, 16b and 16c, respectively). Although IOT13-100% has a higher void ratio than IOT10-100%, their similar air entry values (Table 5) and unsaturated hydraulic conductivity functions, as shown in Fig. 4b, result in comparable responses. In contrast, IOT16-100%, with the highest void ratio, demonstrates a distinct behavior by effectively retaining infiltration water while maintaining a relatively lower degree of saturation. This reduced saturation enhances matric suction development, contributing to its consistently higher FoS throughout the construction of the stack.

Nevertheless, all scenarios exhibit matric suction (negative pore pressure) at control point A throughout the construction stages, maintaining consistent FoS values above 2, as shown in Fig. 16a. Denser tailings, although compacted closer to saturation, sustain an unsaturated state that preserves matric suction by limiting water infiltration and mobility within the stack. This behavior is evident when comparing the results in Figs. 9d and 16d, where internal seepage within tailings compacted to 100% of their respective standard Proctor test remains restricted throughout construction. These findings highlight the critical importance of compacting tailings to denser states, as all materials, despite their distinct properties, have consistently demonstrated stable performance.

Figs. 17 and 18 complement the findings from Fig. 16 by presenting the contours of degree of saturation, pore pressure, and the slope failure surface corresponding to the minimum FoS at Stage 3 for IOT13-100% and IOT16-100%, respectively.

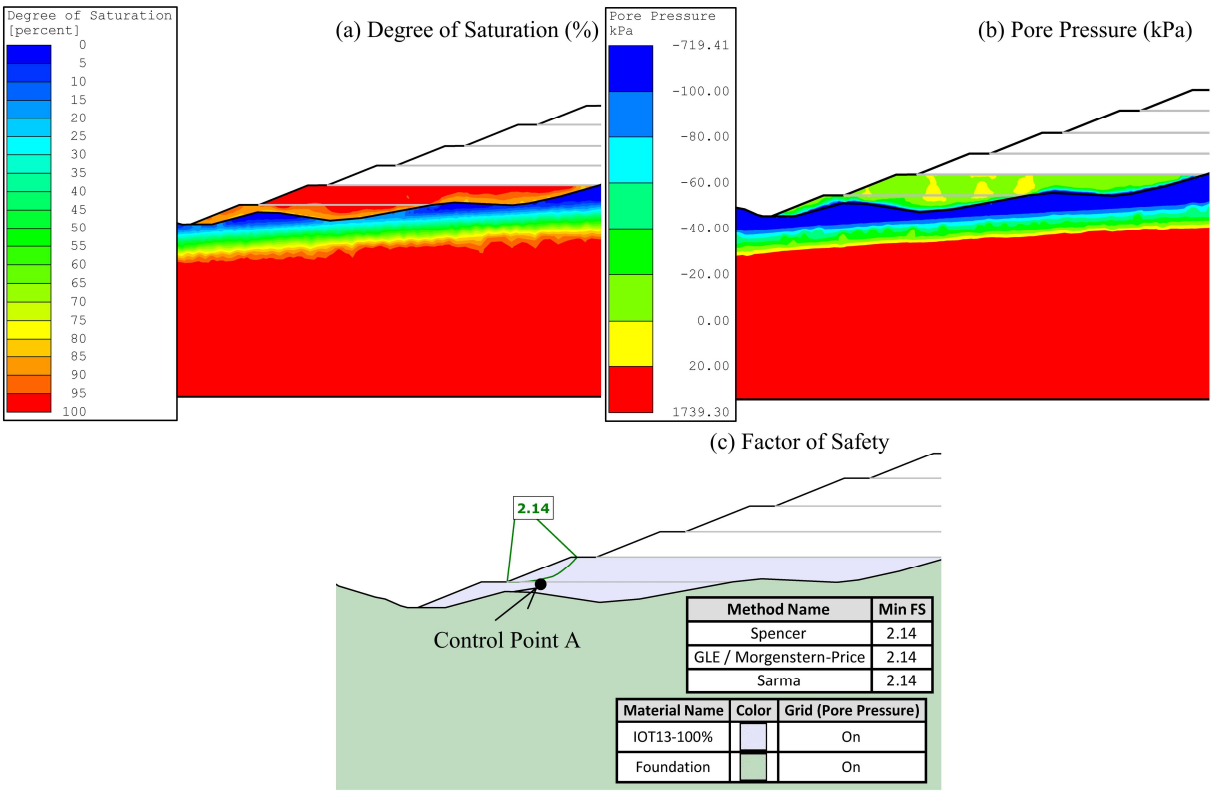

Fig. 17 Response of the filtered tailings stack construction with IOT13-100% at Stage 3. **a** degree of saturation. **b** pore pressure. **c** factor of safety

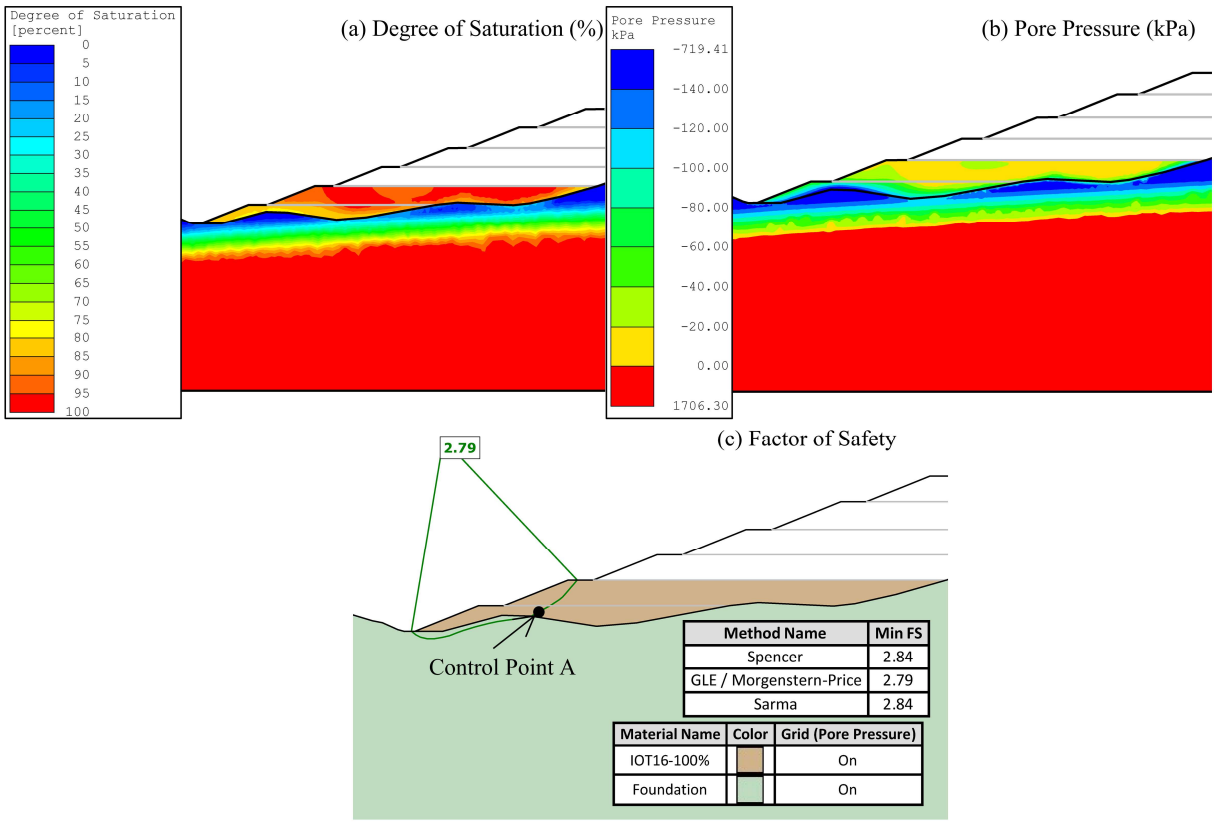

Fig. 18 Response of the filtered tailings stack construction with IOT16-100% at Stage 3. **a** degree of saturation. **b** pore pressure. **c** factor of safety

Compared to the reference scenario IOT10-100% (Fig. 10a), the IOT13-100% scenario exhibits a larger area with degrees of saturation exceeding 95% (Fig. 17a), and displays positive pore pressures in localized regions, reaching up to 20 kPa (Fig. 17b). While matric suction prevails throughout most of the stack (Fig. 17b), similar to the reference scenario (Fig. 10b), the presence of these positive pore pressure zones, particularly near the slope failure surface, contributes to the lower FoS of 2.14 for IOT13-100% compared to 2.38 for IOT10-100% (Figs. 17c and 10c, respectively).

In contrast, for the IOT16-100% scenario (Fig. 18a), a similar degree of saturation contour is observed compared to IOT10-100% (Fig. 10a), with matric suction prevailing throughout the entire stack (Figs. 18b and 10b, respectively). However, the matric suction developed in IOT16-100% is significantly higher, reaching values of up to 60 kPa near the slope surface, compared to a maximum of 20 kPa in the reference scenario. This elevated matric suction plays a crucial role in enhancing stability, forcing the slope failure surface to extend deeper into the foundation—a reflection of the increased shear strength of the tailings under these conditions. Consequently, this scenario achieves the highest FoS of 2.79 at Stage 3 (Fig. 18c).

The behaviors observed at Stage 3 can similarly be extended to Stage 16. Figs. 19 and 20 illustrate the contours of degree of saturation, pore pressure, total displacement, and the slope failure surface corresponding to the minimum FoS at Stage 16 for the IOT13-100% and IOT16-100% scenarios, respectively.

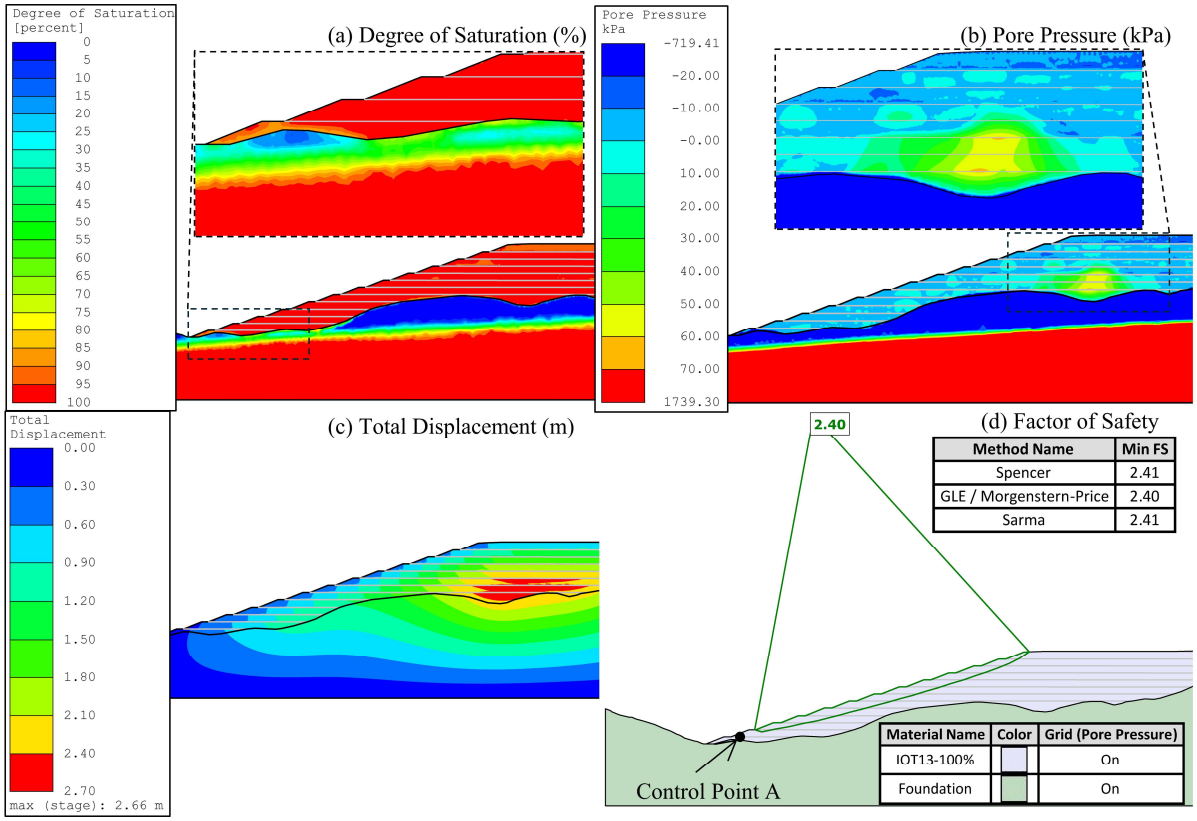

Fig. 19 Response of the filtered tailings stack construction with IOT13-100% at Stage 16. **a** degree of saturation. **b** pore pressure. **c** total displacement. **d** factor of safety

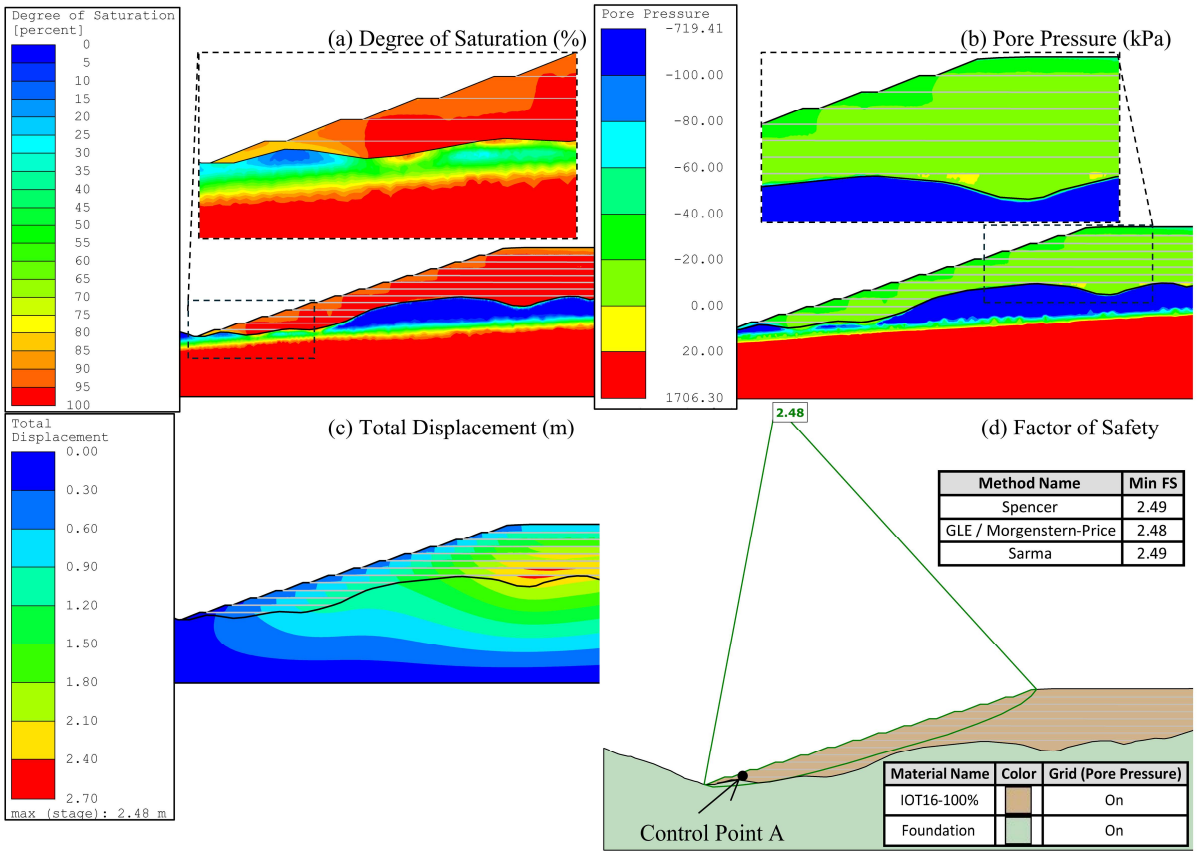

Fig. 20 Response of the filtered tailings stack construction with IOT16-100% at Stage 16. **a** degree of saturation. **b** pore pressure. **c** total displacement. **d** factor of safety

As with the reference scenario, the increased saturation levels in the stack are primarily driven by void ratio reduction caused by overburden stresses across all scenarios. However, in IOT13-100%, saturation levels exceed 95% across nearly the entire stack (Fig. 19a), compared to IOT10-100%, where degrees of saturation near the slope surface range between 90% and 95% (Fig. 13a). In IOT16-100% (Fig. 20a), the areas with degrees of saturation ranging between 90% and 95% expand further into the interior of the stack compared to the reference scenario.

Positive pore pressure development in IOT13-100% is similar to that observed in the reference scenario, being confined to regions with the greatest tailings thickness, where pressures exceed 60 kPa compared to 30 kPa in IOT10-100% (Figs. 19b and 13b, respectively). Elsewhere in the stack, matric suction of up to 10 kPa prevails, consistent with the reference scenario. For IOT16-100% (Fig. 20b), however, the entire stack develops only negative pore pressures (matric suction) at Stage 16, with values reaching as high as 40 kPa near the slope surface. This enhanced suction explains the highest FoS of 2.48 for IOT16-100%, followed by 2.42 for IOT10-100%, and 2.40 for IOT13-100%.

The contours of total displacement at the end of stack construction, presented in Figs. 19c and 20c for the IOT13-100% and IOT16-100% scenarios, respectively, exhibit consistent trends with those observed in the reference scenario, IOT10-100% (Fig. 13c). The greatest displacements occur in regions of maximum tailings thickness. Maximum recorded displacements are 2.70 m for IOT10-100%, 2.66 m for IOT13-100%, and 2.48 m for IOT16-100%. These variations in displacement magnitude can be directly linked to differences in unit weight among the scenarios (Table 5).

3.3 Undercompaction during Rainy Season

The impact of undercompaction during the rainy season on the behavior of the filtered tailings stack during construction was analyzed using numerical simulations for three distinct scenarios: IOT10-100% (e = 0.47), IOT10-90%/100% (e = 0.64/0.47), and IOT10-80%/100% (e = 0.84/0.47). Fig. 21 illustrates the variations in the FoS, degree of saturation, pore pressure at control point A, and seepage, evaluated at the base of the compacted tailings for each scenario. Additionally, Figs. 22 and 23 present the contours of degree of saturation and pore pressure, and the slope failure surface corresponding to the minimum FoS at Stage 3 for the IOT10-90%/100% and IOT10-80%/100% scenarios, respectively.

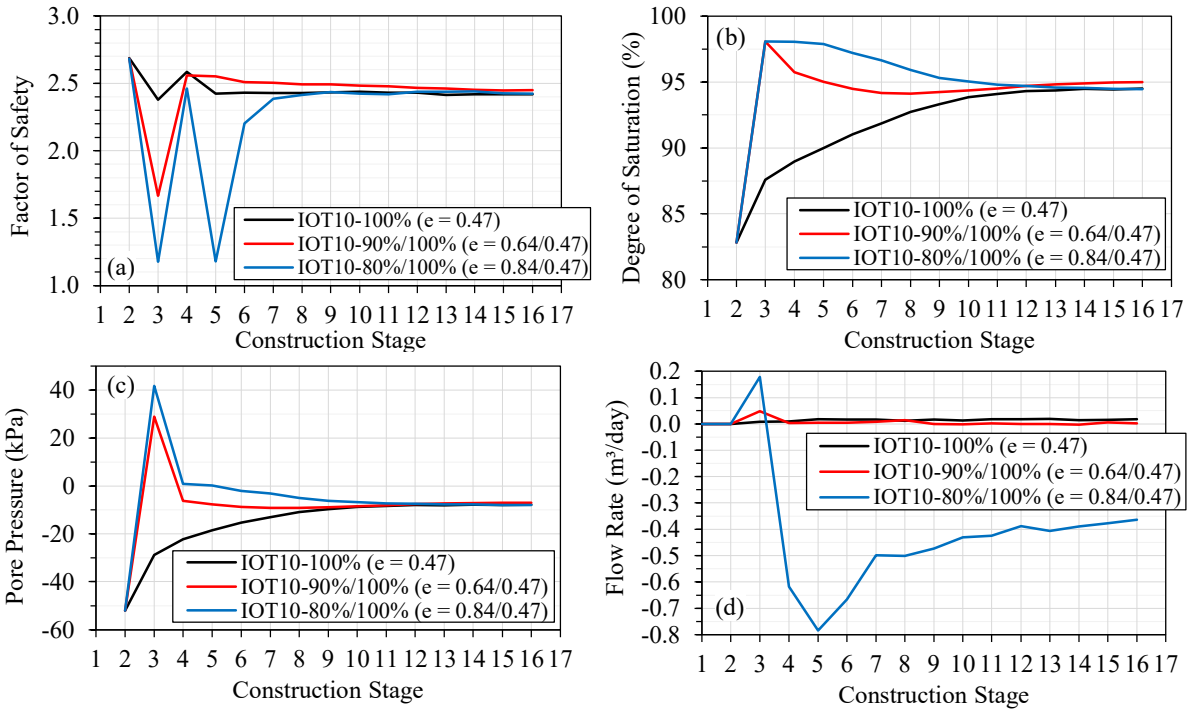

Fig. 21 Influence of undercompaction during rainy seasons on **a** stability, **b** saturation, **c** pore pressure, and **d** seepage through the tailings during construction stages

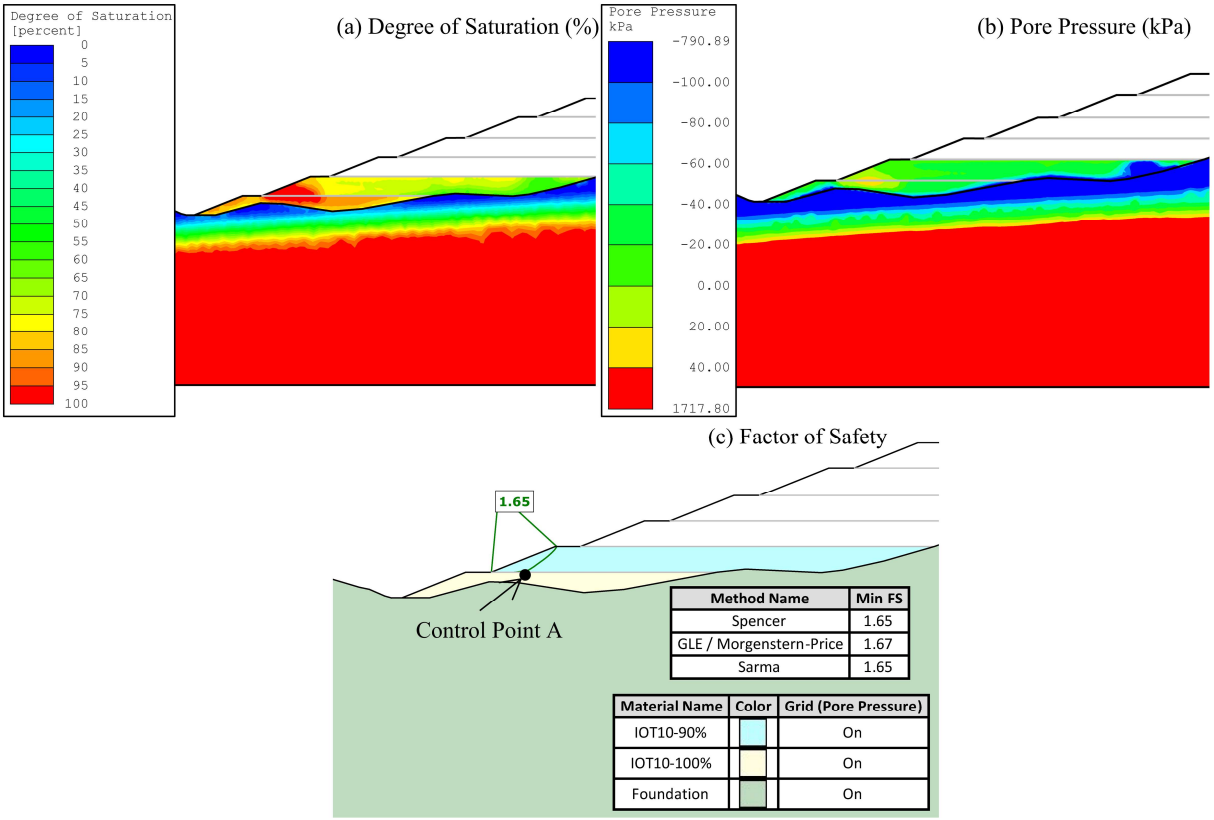

Fig. 22 Response of the filtered tailings stack construction with IOT10-90%/100% at Stage 3. **a** degree of saturation. **b** pore pressure. **c** factor of safety

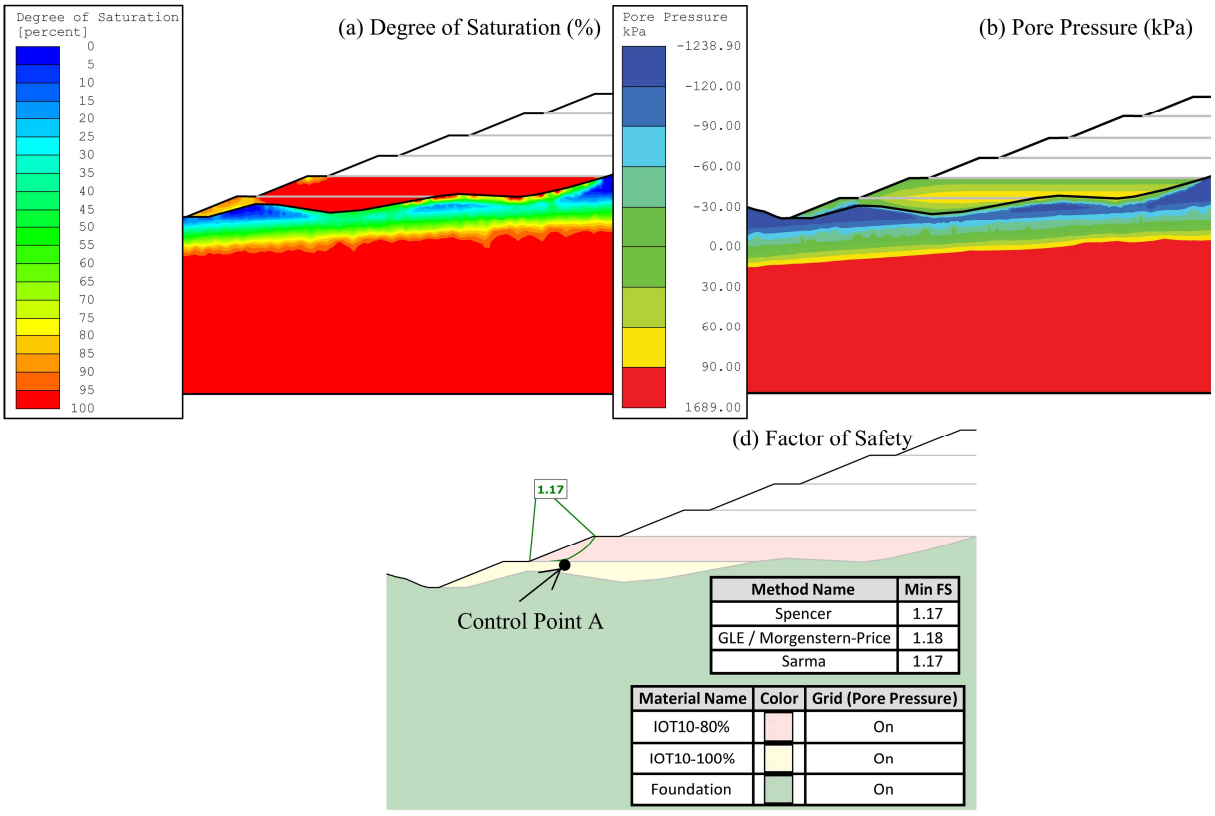

Fig. 23 Response of the filtered tailings stack construction with IOT10-80%/100% at Stage 3. **a** degree of saturation. **b** pore pressure. **c** factor of safety

As discussed in Section 3.1, undercompacted tailings exhibit heightened sensitivity to alternating weather conditions, particularly in the early construction stages. This is evident in Fig. 21a, where greater FoS drops are observed for IOT10-90%/100% and IOT10-80%/100%. For IOT10-90%/100%, compacted to a void ratio of 0.64 during the rainy period and 0.47 during the dry period, the FoS decreases to 1.65 at Stage 3 (Fig. 22c). An even sharper decline is observed in IOT10-80%/100%, constructed with a void ratio of 0.84 during the rainy period, where the FoS drops to 1.17 at Stage 3 (Fig. 23c). In contrast, the reference scenario, IOT10-100%, maintains a FoS of 2.38 at the same stage (Fig. 10c). As construction progresses, the FoS stabilizes during later stages, with IOT10-80%/100% displaying the most pronounced variations.

The relationships between the FoS, degree of saturation, and pore pressure in Figs. 21a, 21b, and 21c demonstrate a strong interdependence during the construction stages. In Stage 3, the sharp drops in FoS observed in Fig. 21a corresponds to the degree of saturation peaks in Fig. 21b and the development of positive pore pressures in Fig. 21c. As construction progresses, the values at control point A show a gradual convergence, with the degree of saturation stabilizing around 95% and pore pressure transitioning to negative values (matric suction) in Fig. 21c. This stabilization of pore pressure and degree of saturation correlates with the gradual increase in FoS, which eventually converges to a stable value of approximately 2.4, as seen in Fig. 21a.

In contrast to the reference scenario IOT10-100% at Stage 3 (Figs. 10a and 10b), where the degree of saturation exceeds 95% only near the surface and negative pore pressures (matric suction) prevail throughout the stack, undercompacted scenarios display markedly different behaviors. For the IOT10-90%/100% scenario, areas with degrees of saturation exceeding 95% extend to the slope surface (Fig. 22a), resulting in positive pore pressures ranging from 20 to 40 kPa near this critical region (Fig. 22b). Similarly, in the IOT10-80%/100% scenario (Figs. 23a and 23b), akin to the behavior observed in the IOT10-80% scenario (Figs. 12a and 12b), the stack becomes fully saturated, forming a perched water table near the surface. Positive pore pressures in this case increase linearly with depth, reaching maximum values ranging between 60 to 90 kPa. These conditions highlight the destabilizing effects of undercompaction, particularly during early construction stages, as increased saturation and positive pore pressures near the slope surface significantly reduce the FoS.

As previously discussed, Section 3.1, seepage in tailings compacted to lower void ratios, such as IOT10-100% and IOT10-90%, is restricted due to their dense structure, which limits water infiltration and mobility. In contrast, higher void ratio stacks, like IOT10-80%, facilitate greater water movement due to their larger pore spaces. This behavior is evident in Fig. 21d, which compares seepage within the tailings for undercompacted scenarios. In IOT10-80%/100%, the seepage is significantly greater than in IOT10-100% and IOT10-90%/100% throughout the construction stages. Positive flow rates represent downward seepage, while negative flow rates correspond to upward movement.

The inversion of seepage observed in IOT10-90%/100% and more prominently in IOT10-80%/100%, as shown in Fig. 21d, is directly related to the formation of perched water tables, arising from the interaction between high- and low-permeability layers within the stack. These heterogeneities, characteristic of undercompacted scenarios, are further explored in Figs. 24 and 25, which depict the contours of degree of saturation, pore pressure, and slope failure surfaces at Stage 16 for the IOT10-90%/100% and IOT10-80%/100% scenarios. While not the main focus of this section, the displacements observed under such conditions were consistent with those obtained in the simulations addressing void ratio variation and material heterogeneity at the same construction stage.

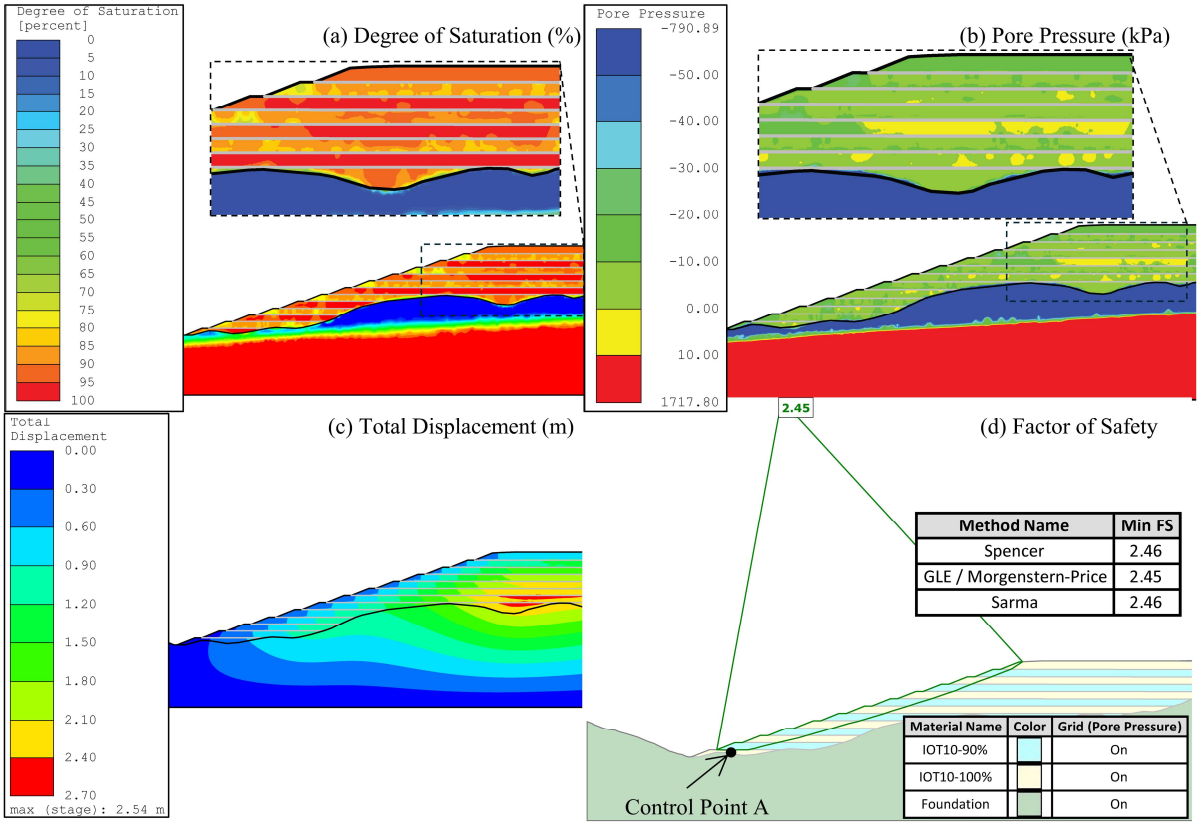

Fig. 24 Response of the filtered tailings stack construction with IOT10-90%/100% at Stage 16. **a** degree of saturation. **b** pore pressure. **c** total displacement. **d** factor of safety

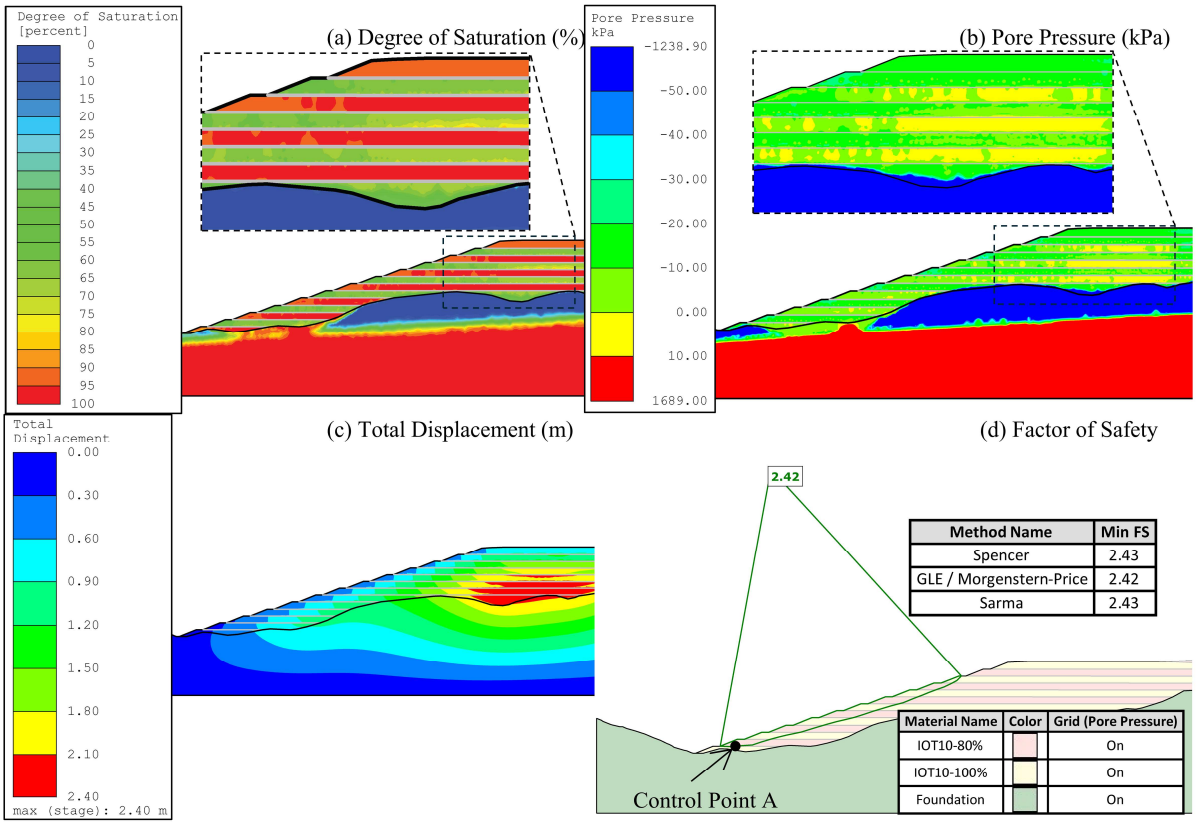

Fig. 25 Response of the filtered tailings stack construction with IOT10-80%/100% at Stage 16. **a** degree of saturation. **b** pore pressure. **c** total displacement. **d** factor of safety

Perched water tables form when infiltrating water encounters low-permeability layers, such as those compacted to the properties of IOT10-100% (Figs. 24a and 25a). This accumulation creates localized saturated zones that reduce matric suction and increase pore water pressure, further lowering effective stress and shear strength, particularly during prolonged rainfall or under additional overburden loads (Figs. 24b and 25b). This behavior is most pronounced in the IOT10-80%/100% scenario (Fig. 21d), where water initially migrates rapidly downward into lower layers (dry season). As construction progresses and overburden pressure increases, the water becomes pressurized, leading to an upward migration back into the layers compacted during the rainy season.

In contrast to IOT10-90%, which is entirely compacted with IOT10-90% properties and shows higher degrees of saturation in layers compacted during the rainy season (Fig. 14a), the undercompacted scenarios (IOT10-90%/100% and IOT10-80%/100%) display distinct saturation patterns (Figs. 24a and 25a, respectively). These differences arise due to the hydraulic conductivity contrasts between layers compacted during different seasons.

By Stage 16, in IOT10-90%/100%, layers compacted during the rainy season exhibit degrees of saturation ranging from 75% to 80%, while those compacted during the dry season exceed 95% (Fig 24a). This leads to localized positive pore pressures of up to 10 kPa in some dry-season layers, while the rest of the stack retains matric suction around 30 kPa (Fig 24b). In IOT10-80%/100%, these effects are more pronounced. Layers compacted during the rainy season show degrees of saturation between 60% and 70%, while those compacted during the dry season reach saturation levels exceeding 95% (Fig 25a). Positive pore pressures of up to 10 kPa develop over a larger area compared to IOT10-90%/100%, as seen in Fig. 25b. However, matric suction of approximately 30 kPa persists across much of the stack.

3.4 Summary of Scenario Performance

Table 8 summarizes the key performance indicators and geotechnical responses across all simulated scenarios. It compiles critical data—including minimum and final Factors of Safety (FoS), pore pressure distributions, and seepage behavior—at both the critical stage and the end of construction. This synthesis supports the comparative assessment and discussion of overall stack behavior throughout Section 3.

Table 8 Summary of key hydraulic and stability responses observed for each construction scenario

Scenario	Void ratio	Minimum FoS during construction	Final FoS after construction	Pore pressure at the critical stage	Seepage condition at the critical stage	Pore pressure at the end of construction	Seepage condition at the end of construction
IOT10-100%	0.47	2.38	2.42	Suction-dominant (up to ~40 kPa)	Very limited seepage; no perched water table	Suction-dominant (up to ~10 kPa); positive pressures exceeding 30 kPa confined outside the structural zone	Very limited seepage; no perched water table within the structural zone
IOT10-90%	0.64	2.33	2.47	Suction-dominant (up to ~40 kPa); positive near slope face (~40 kPa)	Very limited seepage; minor perched water zones near slope face	Suction-dominant (up to ~30 kPa)	Slight increase in seepage; no perched water table within the structural zone
IOT10-80%	0.84	1.01	2.46	Positive (~140 kPa)	Fully saturated; perched water table throughout	Positive pressures at the base of the stack (up to ~40 kPa); suction up to ~30 kPa elsewhere	Fully saturated at the base; significant seepage throughout the stack
IOT13-100%	0.58	2.14	2.40	Suction-dominant (up to ~40 kPa); localized positive zones (up to ~20 kPa)	Very limited seepage; minor perched water zones near slope face	Suction-dominant (up to ~10 kPa); positive pressures exceeding 60 kPa confined outside the structural zone	Very limited seepage; no perched water table within the structural zone
IOT16-100%	0.72	2.79	2.48	Suction-dominant (up to ~60 kPa near slope face)	Very limited seepage; no perched water table	Suction-dominant (up to ~40 kPa)	Very limited seepage; no perched water table within the structural zone
IOT10-90%/100%	0.64 / 0.47	1.65	2.45	Extensive positive zones from slope surface inward (~40 kPa)	Saturated near slope; perched water zones developing near slope face	Localized positive zones (up to ~10 kPa) alternating with regions under suction (~30 kPa)	Perched water table and increased seepage throughout the stack
IOT10-80%/100%	0.84 / 0.47	1.17	2.42	Positive (~90 kPa)	Fully saturated; perched water table throughout	More localized positive zones (up to ~10 kPa) alternating with suction regions (~30 kPa)	Perched water table and significant seepage throughout the stack

FoS = Factor of Safety. Critical stage refers to the lowest FoS observed during staged construction.

4. Conclusion

This study provides a solid foundation for understanding and applying unsaturated soil mechanics in the design and assessment of filtered tailings stacks. The present research advances these principles through comprehensive numerical simulations, addressing the intricate interactions between seepage, pore pressure, and mechanical stability. The findings provide valuable insights to enhance the construction and operation of safer, more efficient filtered tailings systems.

Key results highlight the critical influence of void ratio, tailings heterogeneity, and the potential effects of undercompaction on the hydraulic and mechanical behavior of filtered tailings stacks. Scenarios with lower void ratios, such as IOT10-100%, demonstrated enhanced stability by limiting seepage, and preserving matric suction, particularly along the slope of the stack. These conditions mitigated the pore pressure buildup and ensured consistently high FoS throughout construction, even under alternating rainy and dry conditions. Conversely, higher void ratios, like IOT10-80%, allowed greater water infiltration, leading to rapid saturation and the development of positive pore pressures. This significantly increased instability risks, particularly during the early stages of construction, when the stack's smaller size limits its capacity to store water, allowing pore pressures to reach critical levels in these materials.

Intermediate void ratios, as exemplified by the IOT10-90% scenario, demonstrate restricted water mobility within the tailings but remained highly sensitive to weather conditions. Layers compacted during dry periods retain lower saturation levels by the end of construction, whereas those compacted during rainy periods exhibit higher degrees of saturation, highlighting their susceptibility to weather fluctuations.

The analysis of tailings heterogeneity highlights that, despite variations in material properties—such as IOT10-100%, IOT13-100%, and IOT16-100%—all scenarios demonstrated stable hydraulic and mechanical behavior when compacted to optimal conditions. The reduced void ratios achieved in these scenarios were pivotal in maintaining consistently high FoS across all scenarios. Although material-specific differences were observed—such as higher matric suction and enhanced shear strength in IOT16-100% and a higher frequency of positive pore pressure zones in IOT13-100%—the overall performance emphasized the critical importance of achieving low void ratio.

The analysis of undercompaction during stack construction, as hypothesized in scenarios such as IOT10-80%/100% and IOT10-90%/100%, highlights the destabilizing effects of

perched water tables formed due to reduced compaction efficiency during rainy periods. In these conditions, infiltrating water encounters low-permeability layers, such as those compacted during dry periods, resulting in localized saturated zones with positive pore pressure development. These zones reduce effective stress and diminish the contribution of matric suction to shear strength. This effect is particularly critical during the early construction stages, as reflected in the marked reductions in FoS.

This study underscores the paramount role of effective compaction practices in optimizing the performance and safety of filtered tailings stacks. Achieving uniform and optimal compaction across all layers is essential to prevent the formation of perched water tables and maintain low void ratios, both of which are vital for reliably harnessing the benefits of unsaturated behavior throughout the construction and operation of filtered tailings stacks. By minimizing pore pressure buildup, these practices significantly reduce instability risks, particularly under adverse weather conditions. The insights from this research provide a robust framework for tailoring compaction strategies to address material variability and environmental factors, advancing the design, construction, and management of more efficient and resilient tailings systems.

5. Future Research Directions

Based on the current findings, future research should further investigate key hydromechanical processes and modeling refinements that affect the long-term performance of filtered tailings systems under climate change scenarios. An important direction involves integrating unsaturated soil mechanics into probabilistic risk assessment frameworks to enable a more rigorous quantification of uncertainties related to suction, permeability, and mechanical response. The incorporation of field instrumentation—such as moisture sensors, tensiometers, and piezometers—remains essential for validating numerical predictions and refining boundary condition definitions.

From a design perspective, mitigative strategies such as engineered drainage layers, basal liners combined with toe drains for seepage collection and redirection, and surface covers to reduce infiltration should be considered in the analyses to control saturation profiles and limit the development of positive pore pressures. Lastly, future numerical studies should account for the heterogeneity in stiffness and compressibility among tailings materials, as well as the coupling between suction and volumetric strain.

REFERENCES

Aghazamani N, Scalia J, Bareither CA (2024) Effect of placement water content and dry density on water retention behaviour of filtered tailings. Int J Mining, Reclam Environ 38:214–235. https://doi.org/10.1080/17480930.2023.2260592

Andrade RB, Silva RSA, Almeida MSS, Nagula SS (2025) Evaluation of the liquefaction potential of filtered tailings stacks by means of laboratory investigation. Can Geotech J 62:1–13. https://doi.org/10.1139/cgj-2024-0274

Amoah N, Dressel W, Fourie A (2018) Characterisation of unsaturated geotechnical properties of filtered magnetite tailings in a dry stack facility. In: Jewel RJ, Fourie AB (eds) Paste 2018: Proceedings of the 21st International Seminar on Paste and Thickened Tailings. Australian Centre for Geomechanics, Perth, pp 375–388. https://doi.org/10.36487/ACG_rep/1805_31_Amoah

Bella G (2021) Water retention behaviour of tailings in unsaturated conditions. Geomech Eng 26:117–132. https://doi.org/doi.org/10.12989/gae.2021.26.2.117

Biot MA (1941) General theory of three-dimensional consolidation. J Appl Phys 12:155–164. https://doi.org/10.1063/1.1712886

Bruschi GJ, Santos CP, Khajeh A et al (2025) Hydromechanical Behavior of Cement-Stabilized Iron Ore Tailings. Geotech Geol Eng 43:292. https://doi.org/10.1007/s10706-025-03219-7

Burden R, Wilson GW (2023) Commingling of waste rock and tailings to improve “dry stack” performance: design and evaluation of mixtures. Minerals. https://doi.org/10.3390/min13020295

Cacciuttolo C, Atencio E (2023) Dry stacking of filtered tailings for large-scale production rates over 100,000 metric tons per day: envisioning the sustainable future of mine tailings storage facilities. Minerals. https://doi.org/10.3390/min13111445

Cacciuttolo C, Pérez GC (2022) Practical experience of filtered tailings technology in chile and peru: an environmentally friendly solution. Minerals. https://doi.org/10.3390/min12070889

Cao B, Tian Y, Gui R, Liu Y (2021) Experimental study on the effect of key factors on the soil–

water characteristic curves of fine-grained tailings. Front Environ Sci. https://doi.org/10.3389/fenvs.2021.710986

Carmignano OR, Vieira SS, Teixeira APC et al (2021) Iron ore tailings: characterization and applications. J Braz Chem Soc 32:1895–1911. https://doi.org/10.21577/0103-5053.20210100

Carneiro JJV, Marques EAG, Viana da Fonseca AJP et al (2023) Characterization of an iron ore tailing sample and the evaluation of its representativeness. Geotech Geol Eng 41:2833–2852. https://doi.org/10.1007/s10706-023-02430-8

Chaves LR da C, Heineck KS, Scheuermann Filho HC et al (2025) Field and laboratory study of iron ore tailings–Portland cement blends for dry stacking. In: Proceedings of the Institution of Civil Engineers - Geotechnical Engineering. Pp 31–40. https://doi.org/10.1680/jgeen.23.00097

Consoli NC, Guedes JPC, Azambuja Carvalho JV et al (2025) Mechanical Behavior of Artificially Cemented Iron Ore Tailings Under High Confining Pressures. Geotech Geol Eng 43:209. https://doi.org/10.1007/s10706-025-03170-7

Consoli NC, Silva JPS, Wagner AC et al (2024) Critical state analysis of two compacted filtered iron ore tailings with different gradings and mineralogy at different stages of treatment. Acta Geotech 19:881–898. https://doi.org/10.1007/s11440-023-01963-9

Consoli NC, Vogt JC, Silva JPS et al (2022) Behaviour of compacted filtered iron ore tailings–portland cement blends: new brazilian trend for tailings disposal by stacking. Appl Sci. https://doi.org/10.3390/app12020836

Crystal C, Hore C, Ezama I (2018) Filter-pressed dry stacking: design considerations based on practical experience. In: Tailings and Mine Waste 2018 – Proceedings of the 22th International Conference on Tailings and Mine Waste. UBC Studios, University of British Columbia, Keystone, Colorado, USA, pp 209–219

Dias Neto SLS, Ferraz RL, da Silva TO et al (2024) Hydraulic characteristics of silt-sized iron ore tailings. Geotech Geol Eng 42:3731–3753. https://doi.org/10.1007/s10706-024-02755-y

Doi A, Nguyen TAH, Nguyen NN et al (2023) Enhancing shear strength and handleability of

dewatered clay-rich coal tailings for dry-stacking. J Environ Manage. https://doi.org/10.1016/J.JENVMAN.2023.118488

Durner W (1994) Hydraulic conductivity estimation for soils with heterogeneous pore structure. Water Resour Res 30:211–223. https://doi.org/10.1029/93WR02676

Farenzena HP, Bruschi GJ, Medina GS et al (2024) Iron ore tailings stabilization with alternative alkali-activated cement for dry stacking: mechanical and microstructural insights. Can Geotech J 61:649–667. https://doi.org/10.1139/cgj-2023-0125

Fränkle B, Sok T, Gleiß M, Nirschl H (2024) Copper tailings filtration: Influence of filter cake desaturation. Miner Eng. https://doi.org/10.1016/J.MINENG.2024.108952

Fredlund DG, Morgenstern NR, Widger RA (1978) The shear strength of unsaturated soils. Can Geotech J 15:313–321. https://doi.org/10.1139/t78-029

Gallardo R, Sáez E, Lopez-Caballero F (2025) Cyclic and monotonic undrained response of unsaturated filtered copper tailings. Can Geotech J 62:1–16. https://doi.org/10.1139/cgj-2024-0061

Gallardo R, Sáez E, Lopez-Caballero F (2024) Modeling self-compaction and static stability of a copper filtered tailings pile under unsaturated conditions. Acta Geotech 19:4297–4312. https://doi.org/10.1007/s11440-023-02130-w

Garcia LBL, Lemos Júnior MA, Gomes GJC (2024) Compaction sensitivity in tailings stack infiltration modeling: unsaturated properties uncertainty analysis. In: Tailings and Mine Waste 2024 – Proceedings of the 28th International Conference on Tailings and Mine Waste. UBC Studios, University of British Columbia, Keystone, Colorado, USA

Guedes JPC, Silvani C, Carvalho JVA et al (2024a) Mechanical behaviour of fibre-reinforced cemented iron ore tailings across the compaction curve. Geotech Geol Eng 42:3421–3432. https://doi.org/10.1007/s10706-023-02736-7

Guedes JPC, Wagner AC, Carvalho JVA et al (2024b) Fibers enhancing new mine waste-based alkaline-activated cement for dry stacking purposes. J Mater Civ Eng. https://doi.org/10.1061/JMCEE7.MTENG-17386

Huat BBK, Ali FH, Rajoo RSK (2006) Stability Analysis and Stability Chart for Unsaturated

Residual Soil Slope. Am J Environ Sci 2:154–160. https://doi.org/10.3844/ajessp.2006.154.160

Jesus MH de, Serafim R, Silva JP, Marinho FAM (2023) Unsaturated shear strength parameters for a compacted iron ore tailings. In: E3S Web of Conferences – Proceedings of the 8th International Conference on Unsaturated Soils (UNSAT 2023). E3S Web of Conferences, 382. https://doi.org/10.1051/e3sconf/202338216004

Laureano FV, Kwitko-Ribeiro R, Guimarães L, Leão LP (2022) Mineralogical fingerprint of iron ore tailings in paraopeba river bedload sediments after the B1 dam failure in Brumadinho, MG (Brazil). Minerals. https://doi.org/10.3390/min12060716

Li Z, Zhang C, Zhao J, Yan Q (2021) Safety Factor of Unsaturated Soil Slopes considering the Intermediate Principal Stress Effect and Different Profiles of Matric Suction. Math Probl Eng 2021:1–10. https://doi.org/10.1155/2021/6622522

Medina GS, Farenzena HP, Bruschi GJ et al (2024) The Behaviour of Hydraulically Disposed Silty Iron Ore Tailings Under Static and Cyclic Loading. Geotech Geol Eng 42:4205–4223. https://doi.org/10.1007/s10706-024-02754-z

Mualem Y (1976) A new model for predicting the hydraulic conductivity of unsaturated porous media. Water Resour Res 12:513–522. https://doi.org/10.1029/WR012i003p00513

Nayanthara PN, Rajapakse J, Gallage C et al (2024) Laboratory investigation on the transitional behaviour of tailings from a gold mine site in Australia. Results Eng 24. https://doi.org/10.1016/j.rineng.2024.103481

Oldecop L, Rodari G (2021) Unsaturated mine tailings disposal. Soils and Rocks 44:1–12. https://doi.org/10.28927/SR.2021.067421

Oliveira AHC (2021) Stress-strain analysis in a filtered tailing pile of large dimensions. Dissertation, Federal University of Viçosa

Oliveira E do P, Acevedo AMG, Moreira VS et al (2022) The Key Parameters Involved in a Rainfall-Triggered Landslide. Water. https://doi.org/10.3390/w14213561

Pires K de S, Mendes JJ, Figueiredo VC et al (2019) Mineralogical characterization of iron ore tailings from the quadrilatero ferrifero, brazil, by eletronic quantitative mineralogy. Mater Res. https://doi.org/10.1590/1980-5373-mr-2019-0194

Reichardt K, Timm LC (2004) Soil, plant, and atmosphere: concepts, processes, and applications. Manole, Barueri

Rissoli ALC, Pereira GS, Mendes AJC et al (2024) Dry stacking of filtered iron ore tailings: comparing on-field performance of two drying methods. Geotech Geol Eng 42:2937–2948. https://doi.org/10.1007/s10706-023-02689-x

Sako CH, Pabst T (2023) Comparative geochemical evaluation of codisposal approaches for reactive filtered tailings deposition. Clean Waste Syst. https://doi.org/10.1016/J.CLWAS.2023.100094

Saleh-Mbemba F, Aubertin M (2018) Characterization of Self-Weight Consolidation of Fine-Grained Mine Tailings Using Moisture Sensors. Geotech Test J 41:543–554. https://doi.org/10.1520/GTJ20170035

Sanchez B, Sutta M, Soto J, Benites I (2023) Dry stacked filtered tailings: seepage behaviour during the construction process. In: Wilson GW, Beier GW, Sego GW et al (eds) Paste 2023: Proceedings of the 25th International Conference on Paste, Thickened and Filtered Tailings. University of Alberta, Edmonton, and Australian Centre for Geomechanics, Perth, pp. 620-628. https://doi.org/10.36487/ACG_repo/2355_47

Santos RA, Delgado BG, Rissoli ALC et al (2024) Influence of initial compaction and confining pressure on the hydraulic conductivity of compacted iron ore tailings. In: E3S Web of Conferences – Proceedings of the 8th International Symposium on Deformation Characteristics of Geomaterials (IS-Porto 2023). E3S Web of Conferences, 544. https://doi.org/10.1051/e3sconf/202454414005

Schafer H, Beier N (2020) Estimating soil-water characteristic curve from soil-freezing characteristic curve for mine waste tailings using time domain reflectometry. Can Geotech J 57:73–84. https://doi.org/10.1139/cgj-2018-0145

Schnaid F, Mello LG, Dzialoszynski B (2020) Guidelines and recommendations on minimum factors of safety for slope stability of tailings dams. Soils and Rocks 43:369–395. https://doi.org/10.28927/SR.433369

Sepúlveda RG, Robert ES, Camacho-Tauta J (2022) Assessment of the self-compaction effect in filtered tailings disposal under unsaturated condition. Minerals.

https://doi.org/10.3390/min12040422

Servi S, Lotero A, Silva JPS et al (2022) Mechanical response of filtered and compacted iron ore tailings with different cementing agents: Focus on tailings-binder mixtures disposal by stacking. Constr Build Mater. https://doi.org/10.1016/J.CONBUILDMAT.2022.128770

Silva JPS, Rissoli ALC, Cacciari PP et al (2024) Triaxial testing response of compacted iron ore tailings considering a broad spectrum of confining pressures. Soils Found. https://doi.org/10.1016/j.sandf.2024.101438

Simms P (2021) The role of unsaturated soil mechanics in unconventional tailings deposition. Soils and Rocks 44:1–11. https://doi.org/10.28927/SR.2021.066721

Tebechrani Neto A, Wagner AC, Carvalho JVA, Consoli NC (2025) Effects of fines content, molding water content, and density on behavior of compacted filtered iron ore tailings. Acta Geotech. https://doi.org/10.1007/s11440-025-02616-9

Ulrich B (2019) Practical thoughts regarding filtered tailings. In: Paterson A, Fourie A, Reid D (eds) Paste 2019: Proceedings of the 22nd International Conference on Paste, Thickened and Filtered Tailings. Australian Centre for Geomechanics, Perth, pp 71–79. https://doi.org/10.36487/ACG_rep/1910_01_Ulrich

van Genuchten MT (1980) A closed-form equation for predicting the hydraulic conductivity of unsaturated soils. Soil Sci Soc Am J 44:892–898. https://doi.org/10.2136/sssaj1980.03615995004400050002x

Vanapalli SK, Fredlund DG, Pufahl DE, Clifton AW (1996) Model for the prediction of shear strength with respect to soil suction. Can Geotech J 33:379–392. https://doi.org/10.1139/t96-060

Vargas CC, Campomanes GP (2022) Practical experience of filtered tailings technology in chile and peru: an environmentally friendly solution. Minerals. https://doi.org/10.3390/min12070889

Venturin AM (2022) Seepage analysis of a filtered tailings stack. Dissertation, Federal University of Viçosa

Vizcarra G (2021) Numerical modelling of dry stacking tailings heaps. In: Fourie AB, Reid D

(eds) Paste 2021: Proceedings of the 24th International Conference on Paste, Thickened and Filtered Tailings. Australian Centre for Geomechanics, Perth, pp. 231–238. https://doi.org/10.36487/ACG_repo/2115_19

Wagner AC, Carvalho JVDA, Scheuermann Filho HC, Consoli NC (2024) Influence of grading in compacted tailings behaviour: towards resilient design. Géotechnique. https://doi.org/10.1680/jgeot.23.00475

Wang Y, Vo T, Russell AR (2024) Modelling unsaturated silty tailings and the conditions required for static liquefaction. Géotechnique 74:1377–1389. https://doi.org/10.1680/jgeot.22.00074

Williams DJ (2021) Lessons from tailings dam failures—where to go from here? Minerals. https://doi.org/10.3390/min11080853

Wilson G (2021) The new expertise required for designing safe tailings storage facilities. Soils and Rocks 44:1–8. https://doi.org/10.28927/SR.2021.067521

Zhang C, Chen Q, Pan Z, Ma C (2020) Mechanical behavior and particle breakage of tailings under high confining pressure. Eng Geol 265. https://doi.org/10.1016/j.enggeo.2019.105419

Zhang LL, Fredlund DG, Fredlund MD, Wilson GW (2014) Modeling the unsaturated soil zone in slope stability analysis. Can Geotech J 51:1384–1398. https://doi.org/10.1139/cgj-2013-0394

Zhang Y, Jia H, Liu P et al (2025) Stability Analysis and Optimization of Residual Ore Mining with Granular Backfill. Geotech Geol Eng 43:293. https://doi.org/10.1007/s10706-025-03264-2

Zhang F, Wilson GW, Fredlund DG (2019) Estimation of permeability function for bulyanhulu tailings. Geotech Test J. https://doi.org/10.1520/GTJ20170303

CHAPTER 5

GENERAL CONCLUSIONS

This thesis presents a framework that integrates experimental and numerical approaches to advance the application of unsaturated soil mechanics in the design and assessment of filtered tailings stacks. By focusing on IOT samples from the Quadrilátero Ferrífero region in Brazil, this research addresses critical challenges in understanding the hydro-mechanical behavior of these materials under variable environmental and operational conditions.

Chapter 3 provides a comprehensive exploration of the geotechnical behavior of silt-sized IOT, emphasizing their dual-porosity structure and the critical influence of void ratio and material variability on hydraulic properties. The study highlights that even small variations in particle size distribution, particularly clay content, have a significant impact on water retention and hydraulic conductivity. This underscores the importance of adopting tailored modeling approaches to accurately capture the complex interactions governing these materials. The validation of a dual-porosity conceptual model, accounting for water storage and flow within macropores and micropores, establishes a foundation for a deeper understanding of seepage dynamics in tailings stacks and improves predictive modeling accuracy.

A key finding in Chapter 3 is the direct relationship between void ratio and hydraulic properties, emphasizing the necessity of incorporating these relationships into percolation models and stability assessments. The results demonstrate that IOT cannot be treated as a homogenous material due to persistent differences in hydraulic behavior across samples, even when void ratios are similar. This reinforces the need to model IOTs with material-specific parameters to ensure accurate predictions of hydraulic behavior.

Overall, Chapter 3 delivers a systematic methodology for characterizing the hydraulic properties of IOT, providing critical inputs for the development of improved drainage designs and percolation models. By addressing the complex hydraulic behavior of these materials, this chapter lays the groundwork for incorporating detailed hydraulic analyses into broader numerical simulations.

Building on this foundation, Chapter 4 applies these insights within the realm of numerical simulations to evaluate the transient hydraulic and mechanical behavior of filtered tailings stacks. The simulations revealed that achieving low void ratios is essential for

maintaining stability by limiting seepage, preserving matric suction, and preventing pore pressure buildup, even under alternating wet and dry conditions. Conversely, higher void ratios were associated with rapid water infiltration, leading to saturation and increased instability risks, particularly during early construction stages. These results emphasize the critical role of achieving uniform and optimal compaction during construction.

Chapter 4 also explored the impact of material heterogeneity on seepage dynamics and stability. Tailings compacted at optimal void ratios consistently exhibited stable hydraulic and mechanical behavior, regardless of variability in particle size distribution or mineral composition. However, undercompaction, as explored through hypothetical scenarios simulating reduced efficiency during rainy seasons, revealed significant risks. Perched water tables and localized saturated zones formed under these conditions, diminishing effective stress and shear strength. These findings highlight the importance of addressing environmental challenges during construction to ensure the long-term stability of tailings stacks.

Finally, this research underscores the necessity of integrating experimental findings with advanced numerical simulations to address the complexities inherent in filtered tailings stack design and management. By filling critical knowledge gaps, this study bridges the divide between theoretical insights and practical applications. The proposed methodologies not only align with best practices but also pave the way for safer, more sustainable mining operations, offering solutions tailored to material variability, environmental challenges, and evolving regulatory landscapes. This work establishes a foundation for improving geotechnical practices and sets a precedent for the advancement of filtered tailings management.